A LIPID TALE: ALKYL TAIL IMPURITIES IN TECHNICAL-GRADE OLEYLAMINE REGULATE THE GROWTH AND ASSEMBLY OF ULTRANARROW GOLD NANOWIRES AT CHEMICALLY PATTERNED INTERFACES

by

Erin N. Lang

A Dissertation

Submitted to the Faculty of Purdue University

In Partial Fulfillment of the Requirements for the degree of

Doctor of Philosophy

Department of Chemistry

West Lafayette, Indiana

May 2022

THE PURDUE UNIVERSITY GRADUATE SCHOOL
STATEMENT OF COMMITTEE APPROVAL

Dr. Shelley A. Claridge, Chair

Department of Chemistry &

Weldon School of Biomedical Engineering

Dr. Corey M. Thompson

Department of Chemistry

Dr. Suzanne C. Bart

Department of Chemistry

Dr. Jianguo Mei

Department of Chemistry

Approved by:

Dr. Christine Hrycyna

Dedicated to my parents, Matt & Kerry Lang, for enabling my curiosity, encouraging me to dream big, and for helping me up each and every time I fell along the way.

ACKNOWLEDGMENTS

There are a number of individuals without whom this journey would not have been possible. It truly takes a village. I am privileged to be surrounded with people who support me in so many ways. It is feels impossible to properly express the deep gratitude I feel for all the time and energy invested in me by countless individuals; let this attempt to express my thanks in writing be a start. To those not specifically acknowledged in this far from exhaustive list, know that your contributions have not gone unnoticed, and I hope that you feel my gratitude all the same.

To my advisor, Professor Shelley A. Claridge: Thank you for believing in me, and for always leading by example. Thank you for challenging me to be better, push harder, and give more. Thank you for being patient and kind. Thank you for investing endless time and resources into my development as a scientist and human.

To my first mentor, Professor Kurstan L.H. Cunningham: Thank you for identifying my potential, letting me be part of your research endeavors, convincing me that scientific research can in fact be a career, and teaching me the skills I needed to make it to graduate school. Thank you for showing me that passion and spunk are necessary ingredients for success in all things.

To my lab mates past and present: Thank you for your advice, support, friendship, and helpful suggestions along the way. Thank you for making our lab a fun place to work, day in and day out. Thank you for helping me find the levity I needed to get through the days when nothing was working.

To my family: Thank you for your endless and unconditional love, support, and encouragement; without it I would be nowhere.

To Johannes, JC, Sangeeta, Brian, and the many other friends that helped make West Lafayette feel like home: Thank you for making my years in West Lafayette memorable, and for making sure I did things outside of the lab every once in a while.

To the volleyball community of Lafayette: Thank you for welcoming me, and for providing me with some of the most fun experiences I had during my time in Indiana.

Thank you. Thank you. Thank you.

TABLE OF CONTENTS

LIST OF FIGURES

ABSTRACT

A staggering number of problems in materials chemistry relate to controlling the assembly of matter at <10 nm scales, including those with applications in nanoelectronics, energy harvesting, and biomedical device design. It is difficult to achieve precise chemical patterning at the short length scales required for such applications using traditional top-down fabrication methods (*e.g.*, lithographic techniques). On the other hand, biological systems create high-resolution chemical patterns with remarkable efficiency, by assembling simple molecular building blocks with nm-scale features (*e.g.*, nucleotides, amino acids, lipids) into structurally complex motifs capable of carrying out the diverse functions required for life.

Drawing inspiration from the diverse structures and functions of lipids in biological membranes, this work uses lipids to create high-resolution chemical patterns at interfaces, control the growth and self-assembly of nanocrystals, and to facilitate interactions that precisely template nanocrystals at chemically patterned surfaces.

Functional alkanes assemble into striped phase monolayers on highly oriented pyrolytic graphite (HOPG), in which the alkyl chains are oriented parallel to the substrate, expressing both the polar and nonpolar regions of the amphiphile at the environmental interface. The same is true for diyne phosphoethanolamine (dPE), a phospholipid with a zwitterionic headgroup. When assembled into striped phases on HOPG, the headgroup zwitterions of dPE are confined in 1-nm-wide rows of functional groups with a pitch of ~7 nm, resulting in ordered arrays of orientable dipoles at the HOPG surface. The chemistry of dimensionally confined functional groups is distinct from bulk solution phase chemistry, and in this case enables powerful directing effects which can be used to template the adsorption of ultranarrow gold nanowires (AuNWs) in precise alignment with the template stripes.

Technical grade oleylamine (*cis*-9-octadecen-1-amine, OLAm, 70% purity) serves as the capping ligand for the AuNWs used in this work, and additionally plays an important role in the assembly of AuNWs at dPE/HOPG surfaces. While technical-grade reagents enable cost-effective and scalable production of materials, variation in the composition of impurities between different batches have significant impacts on nanocrystal morphology and assembly. We show that thermal transitions of alkyl chain impurities (*trans* and saturated chains) in AuNW ligand shells can be used to regulate AuNW assembly at chemically patterned interfaces.

Characterization of OLAm reagents by ^{1}H NMR and mass spectrometry reveals significant and highly variable fractions elaidylamine (ELAm, *trans*-9-octadecen-1-amine) and octadecylamine (ODAm) between different batches of OLAm. To understand the phase behavior of mixtures of the C18 alkylamines commonly found in technical grade OLAm, we synthesize isomerically pure OLAm and its *trans* isomer, elaidylamine (ELAm), to generate binary and ternary mixtures with (ODAm), which is commercially available in high purity. Differential scanning calorimetry reveals limited miscibility of the C18 chains, and demonstrates the significant impact of chain composition on the physical properties of mixtures of alkyl chains (*e.g.*, tech. grade OLAm). Finally, we examine the impacts of *trans* and saturated alkyl chains on AuNW synthesis. We find that inclusion of ODAm and ELAm in the ligand blend used for AuNW synthesis each result in shorter AuNWs than those synthesized with pure OLAm. We also observe enhanced stability of surface adsorbed AuNWs conferred by *trans* and saturated chains.

CHAPTER 1. INTRODUCTION

A portion of this chapter was previously published in *The Encyclopedia of Nanomaterials*
DOI: 10.1016/B978-0-12-822425-0.00014-2

1.1 Strategies for controlling chemistry at 5-10 nm scales

The ability to control the assembly of matter at sub-10-nm scales is central to many problems in modern materials chemistry, with implications for energy harvesting, biomedical device design, and nanoelectronics. While advances in traditional top-down fabrication techniques (*e.g.,* extreme ultraviolet (EUV) lithography) have enabled patterns with line widths in this size regime, patterning at sub-10 nm scales is costly, and process induced defects result in low fidelity and line roughness.[1, 2] Bottom-up fabrication methods offer an alternative approach to generating high-resolution chemical patterns: assembling atomic and molecular scale units into extended structures.

Structural hierarchy in biological systems creates complex entities with precise spatial ordering at both the nanoscale and microscale. By assembling simple molecular building blocks with nm-scale features (*e.g.*, nucleotides, amino acids, sugars, lipids), biological systems construct high-resolution chemical patterns with remarkable efficiency. Advances in biomolecule synthesis have fueled the design of bottom-up fabrication methods for controlling the chemistry of materials at 5-10 nm scales.

1.2 Lipids as biomolecular templates for interfacial nanomaterial assembly

The striking diversity of structure and function in biological materials has led to the development of many biomimetic and bioinspired approaches to material design, including the design of interfaces. Biological organisms require diverse interfacial chemistries, from cell membranes that mediate sensing and signaling and compartmentalize life functions, to musculoskeletal interfaces that structure integration of hard and soft materials to enable motility. The biological building blocks (*e.g.,* nucleotides, amino acids, sugars, lipids) used by living organisms can be repurposed for interface design, including molecular recognition and precise positioning of functional moieties at an interface. In this work, we leverage diverse structures and

functions of lipids for creating chemically patterned interfaces and facilitating nanoscale interactions.

Lipids perform many roles in living organisms, including compartmentalization, energy storage, signaling, and pigmentation,[3] pointing to an equally broad array of possible functions in artificial material interfaces. To carry out these diverse functions, biological systems employ thousands of chemically diverse lipid structures. Broadly, lipids are typically comprised of a core (often glycerol) linked to a hydrophilic headgroup and one or more hydrophobic alkyl chains, however each of these components can exhibit substantial variations that enable function. Importantly, the polar–nonpolar boundary generated by the assembly of lipids has chemical consequences, including substantial pK_a shifts and the ordering of surrounding solvent molecules, that alter function at both biological and synthetic interfaces in useful ways.

Typically, in both biological and nanotechnological systems, lipid self-assembly processes are based on the sequestration of either nonpolar chains (*e.g.*, biological membranes) or polar headgroups (*e.g.*, nanocrystal ligand shells), resulting in uniform presentation of the opposite chemistry at the environmental interface. However, it is also possible to generate lipid assemblies in that expose both polar headgroups and nonpolar alkyl chains at the environmental interface (*e.g.*, striped phase monolayers). The work presented here involves numerous lipid assemblies and uses lipid mediated interactions to control the assembly of matter at scales ranging from <10 nm to hundreds of microns.

1.3 Striped phase phospholipid assemblies

Functional alkanes (*e.g.*, saturated fatty acids, phospholipids) assemble into striped phase monolayers on highly oriented pyrolytic graphite (HOPG), in which the alkyl chains are oriented parallel to the substrate surface.[4] The lying down orientation of amphiphilic lipids in striped phases enables the expression of both the polar and nonpolar regions at the environmental interface. These noncovalently adsorbed monolayers are stabilized by alkyl-π interactions with the substrate, lateral interactions between alkyl chains, and interactions between polar headgroups.[4-6]

Striped phases of phospholipids, which resemble repeating cross-sections of biological membranes, generate nm-resolution chemical patterns with a sub-10-nm pitch, and distinct functions with respect to standing-phase lipid monolayers.[7] In this work, we use striped phases of diyne phosphoethanolamine (dPE), a phospholipid with a zwitterionic headgroup, as a striped

template for solution phase assembly processes. The diacetylene groups of dPE align along the stripe direction in the as-assembled monolayer, enabling photopolymerization via UV irradiation to generate polydiacetylene (PDA) backbones, which confer additional stability by tethering molecules along the stripes together.[8-10]

In striped phases, zwitterionic dPE headgroups are confined to 1-nm-wide rows positioned at a 1D boundary with nonpolar alkyl chains. Similar to functional groups at the 2D polar-nonpolar boundary of cell membranes, the dimensionally confined dPE headgroup zwitterions exhibit distinct chemistry compared to bulk solution. For example, the phosphate group, which sits adjacent to the HOPG, undergoes a 5 unit shift in p$K_{1/2}$, whereas the ammonium group, which protrudes into the environment maintains standard ionization behavior.[7] The dipoles of zwitterionic dPE headgroups are orientable, and have been shown to template the adsorption of ultranarrow gold nanowires (AuNWs) in precise alignment with the template stripes.[11] Ordered arrays of AuNWs can extend over areas of almost 10,000 μm^2.[12] The directing effects exhibited by striped phases in the adsorption of AuNWs are discussed in more detail in Chapter 3.

1.4 Lipids at nanocrystal surfaces

A common function of lipids at nanostructured interfaces is as ligands for inorganic nanocrystals. Nanocrystals are often synthesized using low-purity technical-grade reagents, which enable cost effective and scalable synthetic routes. However, in a number of cases, impurities in technical blends have been shown to modulate particle morphology. The importance and known impacts of technical-grade impurities related to nanocrystal synthesis are discussed in detail in Chapter 2, including a case study of oleylamine (*cis*-9-octadecen-1-amine, OLAm), which serves as the capping ligand for the AuNWs used throughout this work.

Technical-grade OLAm is typically prepared from natural sources (*e.g.*, through hydrolysis and amination of vegetable oils or beef tallow) and is commonly available as a 70% purity technical blend. In Chapter 3, characterization of technical-grade OLAm blends by ^{1}H NMR and mass spectrometry reveals large fractions of impurities with the intended headgroup structure and alternate alkyl chain structures. The alkyl chain composition varies dramatically from blend-to-blend. As with biological membranes, thermally regulated phase transitions in nanocrystal ligand shells can be an important driver of assembly. We show that thermal transitions of *trans* and

saturated alkyl impurities in ligand shells composed predominantly of *cis*-unsaturated oleylamine can be used to regulate AuNW assembly at biotemplated interfaces.

The most abundant impurity in technical-grade OLAm reagents is elaidylamine (*trans*-9-octadecen-1-amine, ELAm), which we find is present at levels of 15-50%. Another significant impurity is octadecylamine (ODAm). In biological membranes, mixtures of lipids with differences in the degree of saturation or alkyl chain length allow for dynamic phase segregation, generating lipid rafts involved in protein clustering for many cellular signaling pathways. This raises the possibility that similar levels of control over mesoscale nanocrystal assembly may be achieved by using similar approaches. To understand the phase behavior of mixtures of the 18-carbon alkylamines commonly found in technical-grade OLAm, we synthesize isomerically pure OLAm and its *trans* isomer, ELAm, and characterize mixtures OLAm, ELAm, and ODAm using differential scanning calorimetry (DSC). In Chapter 4, phase diagrams constructed for binary and ternary mixtures of C18 alkylamines reveal limited miscibility of the different chain morphologies. We show that chain composition has important outcomes for the physical properties of alkyl chain mixtures (*e.g.*, technical-grade OLAm). Additionally, we investigate the impacts of *trans* and saturated chains on AuNW synthesis. We find that both ELAm and OLAm both shorten AuNW lengths when included in the ligand blend used for AuNW synthesis. We also observe enhanced stability of surface adsorbed AuNWs with the inclusion of small percentages of *trans* and saturated chains in AuNW ligand shells.

CHAPTER 2. COW-TO-COW VARIATION IN NANOCRYSTAL SYNTHESIS: LEARNING FROM TECHNICAL-GRADE OLEYLAMINE

A version of this chapter has been published in *Nanotechnology*
DOI: 10.1088/1361-6528/ac39cb

2.1 Introduction

Many technical-grade reagents, including oleylamine, are broadly used as ligands in nanocrystal synthesis, allowing for cost-effective, and more environmentally friendly, preparation of materials in useful quantities. Impurities can represent 30% or more of these reagent blends, and have frequently emerged as substantial drivers of nanocrystal morphology, assembly, or other physical properties, making it important to understand their composition. Some functional alkyl reagents are derived from natural sources (*e.g.* often beef tallow, in the case of oleylamine), introducing alkyl chain structures very different than those that might be expected as side products of synthesis from pure feedstocks. Additionally, impurities can exhibit variations based on biological factors (*e.g.* species, diet, season). In biology, blends of alkyl chains allow for surprisingly sophisticated function of amphiphiles in the cell membrane, pointing to the possibility of similar control in synthetic materials if reagent composition were either better controlled or better understood. Here, we provide brief context on the breadth of roles technical-grade impurities have played in nanocrystal materials, followed by a perspective on oleylamine impurities, their physical properties, and their potential contributions to nanomaterial function.

2.2 Technical-grade reagents in nanocrystal synthesis

Many reagents used as inorganic nanocrystal (NC) ligands were originally developed for industrial mining and lubrication applications,[13, 14] and are commonly available in cost-effective technical grades (*e.g.* 70%–90% purity). These improve synthetic scalability, and reduce energetic costs and synthetic waste associated with preparation of high-purity ligands; however, the impurities can also have unintended impacts on synthetic outcomes including particle morphology or assembly. Impurities in such blends are seldom well-characterized in product information, despite a growing number of reports that demonstrate batch-to-batch variability in NC morphology based on reagent supplier or lot number.[15-20]

In some cases, technical grades are derived from natural products, meaning that impurities can be different, and more variable, than those that would appear as side products in preparative reactions from pure feedstocks. For instance, technical-grade oleylamine (OLAm, *cis*-9-octadecen-1-amine), is frequently prepared by hydrolysis and amination of animal tallow (typically beef) or vegetable oils.[21, 22] Fatty acids liberated by hydrolysis of the fats (triacylglycerols) are treated with ammonia, yielding ammonium–carboxylate salts of the acyl chains present in the fat, which are subsequently converted to amides, then nitriles, and finally amines.[22] As a result, composition of the impurity fraction can vary widely with the fat source, based on differences in the fractions of specific of acyl chains appended to the glycerol backbones.[23] Even within a single type of source there can be substantial variation: for instance, beef tallow contains fatty acyl chains ranging in length from 14 to 18 carbons with 0 to 2 degrees of unsaturation. The abundances of individual chains can vary by as much as a factor of two from cow to cow (*e.g.* 15%–30% for stearoyl chains).[24] These variable blends of alkyl chains can influence the final composition of the oleylamine reagent.

Unlike many other ligands, which are typically available in both high- and low-purity grades, oleylamine is predominantly available in low-purity forms (commonly a 70% purity technical grade),[25] likely due to its historical use in applications that did not require high purity (discussed in more detail below). Products that indicate a numerically higher % purity sometimes use qualifiers (*e.g.* '98% primary amine'),[26] which would also apply to high-abundance impurities such as elaidylamine and octadecylamine, meaning that the percentage may not reflect the abundance of OLAm itself. High-purity OLAm can be synthesized from high-purity commercially available oleic acid (OLAc).[17, 27] However, the cost of high-purity OLAc and effort of synthesis make this impractical as a routine reagent preparation for laboratory nanocrystal synthesis.

Impurities in OLAm and other reagents play important roles in nanocrystal synthesis and assembly. Here, we first briefly describe some of the known impacts of impurities in other nanocrystal ligands. We then discuss in more detail the composition of OLAm reagents, particularly in regard to impurities with alternate alkyl chain structures, and their impacts on reagent physical properties and nanocrystal synthesis and assembly.

2.3 Modified headgroups and counterions

Reagent impurities with altered headgroup structures, as well as ionic impurities, can modify particle surface coordination, impacting crystal size, shape, and polydispersity.[15, 18] Much of the development of this understanding has centered around phosphorous amphiphiles (phosphines, phosphine oxides, phosphinic and phosphonic acids), due to early observations of variable morphologies in CdSe NCs synthesized with technical-grade (typically 90% purity) tri-n-octylphosphine oxide (TOPO).

A foundational report by Peng and Alivisatos in 2000 established shape control of CdSe NCs by simulating impurities in technical-grade TOPO to generate controlled rod morphologies.[28] Technical-grade TOPO contains substantial quantities of alkylphosphinic acid and alkylphosphonic acid impurities (Figure 2.1, pink region) that bind strongly to Cd^{2+} ions, altering growth rates along the c-axis of the wurtzite crystal. While synthesis of CdSe NCs with a purified (99%) TOPO ligand generated spheres, addition of hexylphosphonic acid (5%–20%) instead resulted in rods. Wang and Buhro[20, 29] later used 31P NMR to determine specific impurities present in TOPO and their influence on nanocrystal morphology allowing for their use as additives to improve size and shape control in NC syntheses. Di-n-octylphosphinic acid (DOPA) emerged as a common intrinsic impurity in technical-grade TOPO associated with rod growth.[29] Because semiconductor nanocrystal syntheses are often carried out at high temperature, new impurity species can also be formed during synthesis (*e.g.* through oxidation of TOPO or disproportionation of dioctylphosphine oxide to generate DOPA).[30, 31] Morris-Cohen and Weiss showed that, following purification, phosphonate impurities are the primary impurities that remain bound to the surface of high-quality CdSe quantum dots (QDs).[32] Other phosphorus-containing ligands exhibit related phenomena. For instance, tri-n-octylphosphine (TOP) is also used in a 90% technical grade to synthesize cadmium and lead chalcogenide NCs; diphenylphosphine impurities have been shown by Steckel and Bawendi to be important in nanocrystal nucleation, in some cases increasing yield of metal selenide NCs.[33]

Ligands with amine headgroups (*e.g.* hexadecylamine, octadecylamine, OLAm) are also commonly used in nanocrystal synthesis, and can interact with the nanocrystal surface either as a neutral species (through donation of the amine electron pair), or as a cation (through electrostatic interactions of the protonated ammonium).[34, 35] Amines can react with dissolved impurities in the reagent bottle, or with other nanocrystal reaction components, to generate species that alter

coordination behavior. Golan and coworkers found that important classes of impurities for amines (Figure 2.1, blue region) include CO_2 and water, which act to generate the charged form of the headgroup (alkylammonium/alkylcarbamate pairs from reactions with CO_2,[36, 37] or alkylamonium species generated from HCl byproducts of water and inorganic chloride precursors[38, 39]). For alkylammonium reagents such as cetyltrimethylammonium bromide (CTAB), Millstone and others illustrated that halide impurities (Figure 2.1, green region) can also be important, since binding energies of halides on gold surfaces increase with increasing polarizability (Cl^- < Br^- < I^-), and are highest for the Au(111) facet.[19, 40] Iodide impurities, typically present in concentrations from ~3 to 850 ppm,[41, 42] bind strongly to the Au(111) facet, forcing growth in the (110) direction, and altering particle morphology (producing spheres, rods, or prisms).[18, 19, 41, 43]

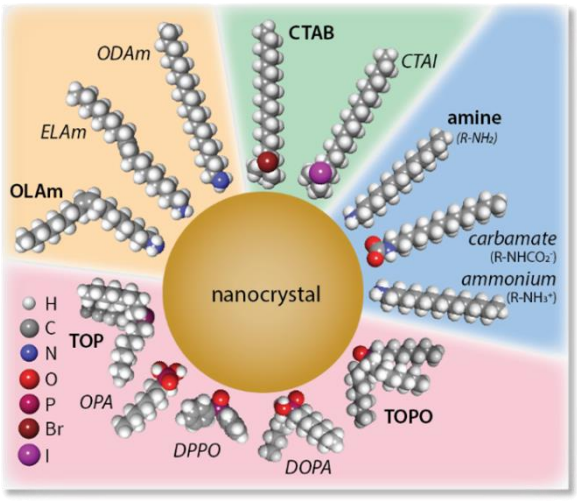

Figure 2.1. Overview of nanocrystal ligands (bold) and common impurities (italicized molecules in same section).

2.4 Modified alkyl chain structures: oleylamine

Although most literature on nanocrystal ligand impurities to date has focused on headgroup chemistry, ligand alkyl chains can influence ligand shell packing, in turn impacting ligand adsorption/desorption, and NC growth, solubility and assembly. For example, experiments by Pradhan and Peng, using high-purity saturated alkyl ligands, have shown that decreasing surface ligand dynamics by increasing the chain length of alkylamine capping ligands slows the growth rate of spherical CdSe NCs at a given temperature.[44] Such effects can also contribute to particle anisotropy. Kim and Lee controlled the asymmetric axial growth of CdSe/CdS core/shell nanorods

by using the relative fraction of octadecylphosphonic acid (ODPA) and hexylphosphonic acid (HPA) ligands as a means of controlling the reactivity of each end of the growing NRs.[45]

Effects of saturated chain impurities in technical-grade blends have been less studied, but impacts are likely to be similarly significant. For instance, Liu and Swihart showed that addition of hexadecylamine to technical-grade OLAm reduced diameters of spherical Au/Ag alloy particles, in comparison with unmodified technical OLAm.[46] Likewise, our own previous experiments showed that addition of octadecylamine to technical OLAm altered particle assembly behavior associated with ligand shell phase transitions.[17]

With this in mind, when considering possible impacts of unintended species in technical-grade reagents, it is also useful to consider alkyl chain compositions. Here, we discuss this issue, focused primarily on OLAm, which is broadly used, and primarily available in very low purity. However, similar issues would also be relevant to oleic acid and other common ligands, especially those derived from biological sources. Overall, the more subtle impacts of alkyl ligand impurities, in comparison with headgroup impurities, and the lack of commercially available pure ligand for direct comparisons, have likely contributed to the limited literature on impacts of these impurities.

Oleylamine appears as a ligand in many synthetic protocols for metal, metal–halide perovskite, metal oxide, and semiconductor nanocrystals,[47-53] with 100–200 publications per year using both 'nanocrystal' (or variations) and 'oleylamine' as keywords since 2010. It plays many roles, often serving simultaneously as a reducing agent and capping ligand, and in some cases also a solvent, since it is a liquid at room temperature.

Prior to finding widespread use in nanocrystal synthesis, OLAm was used for an equally broad range of industrial applications including as an additive to lubricants[14] and corrosion inhibitors,[54] and for mining of various ores.[13] A 1986 EPA report estimated annual OLAm production to be stable at 4.5–5.5 million pounds, noting that actual production levels are confidential.[22] Industrial applications of OLAm require significant quantities of the reagent, but not necessarily high purity. For example, a variety of long-chain primary alkylamines, including OLAm, can be used to collect KCl from potash ore via a froth flotation process.[13] For such applications, the primary amine headgroup is important, while a range of alkyl chain structures provide similar function. Thus, OLAm is typically commercially available in inexpensive, low-purity technical grades (*e.g.* 70% purity) that are straightforward to prepare from natural feedstocks (*e.g.* tallow), as discussed in the introduction.

Abundant impurities in OLAm are typically also primary alkylamines, with other chain structures common in biological triglycerides. The most common impurity in commercial OLAm is the isomer elaidylamine (*trans*-9-octadecen-1-amine, ELAm Figure 2.2, upper left).[16, 17] Quantification of the relative proportions of OLAm (*cis*) and ELAm (*trans*) based on allylic and vinylic protons in ^{1}H-NMR, indicates that technical blends contain ~15%–50% ELAm, with percentages on the lower end of the range more typical.[16, 17] Data in a recent report by Baranov and Jonas (Figure 2.2, upper left panel) illustrate that a batch of oleylamine labeled '98% amine' contains substantially more ELAm than the '70%' technical grade (visible as higher NMR peak intensity from 5.34 to 5.38 ppm);[16] we found similar results with a batch of 'min. 95%' OLAm in recent work.[17]

Primary alkylamine impurities with varying lengths and degrees of saturation (*e.g.* octadecylamine (18:0), octadecadienamine (18:2), hexadecylamine (16:0), hexadecenamine (16:1)) also make up significant fractions of technical-grade OLAm reagents (as characterized by mass spectrometry), again with substantial batch-to-batch differences.[16, 17] In three different commercial OLAm reagents (Figure 2.2, lower left panel), we found relative abundances of <1%–10% for 18:0, <1%–7% for 16:0, and 5%–36% for 18:2 (compared with the primary OLAm/ELAm peak intensity as 100% relative abundance).

As with the ligands discussed in section 2, some impurities reported in OLAm blends have different headgroup chemistry (*e.g.* alkylamides, nitro-compounds), although these typically have lower abundance relative to the modified chain structures. Baranov and Jonas reported a purification strategy that substantially decreases the abundance of oxygen-containing impurities, which improved solubility of precursors for PbS QDs.[16] However, the removal of alkylamine impurities is not straightforward, making it difficult to generate high-purity OLAm starting from technical grades.

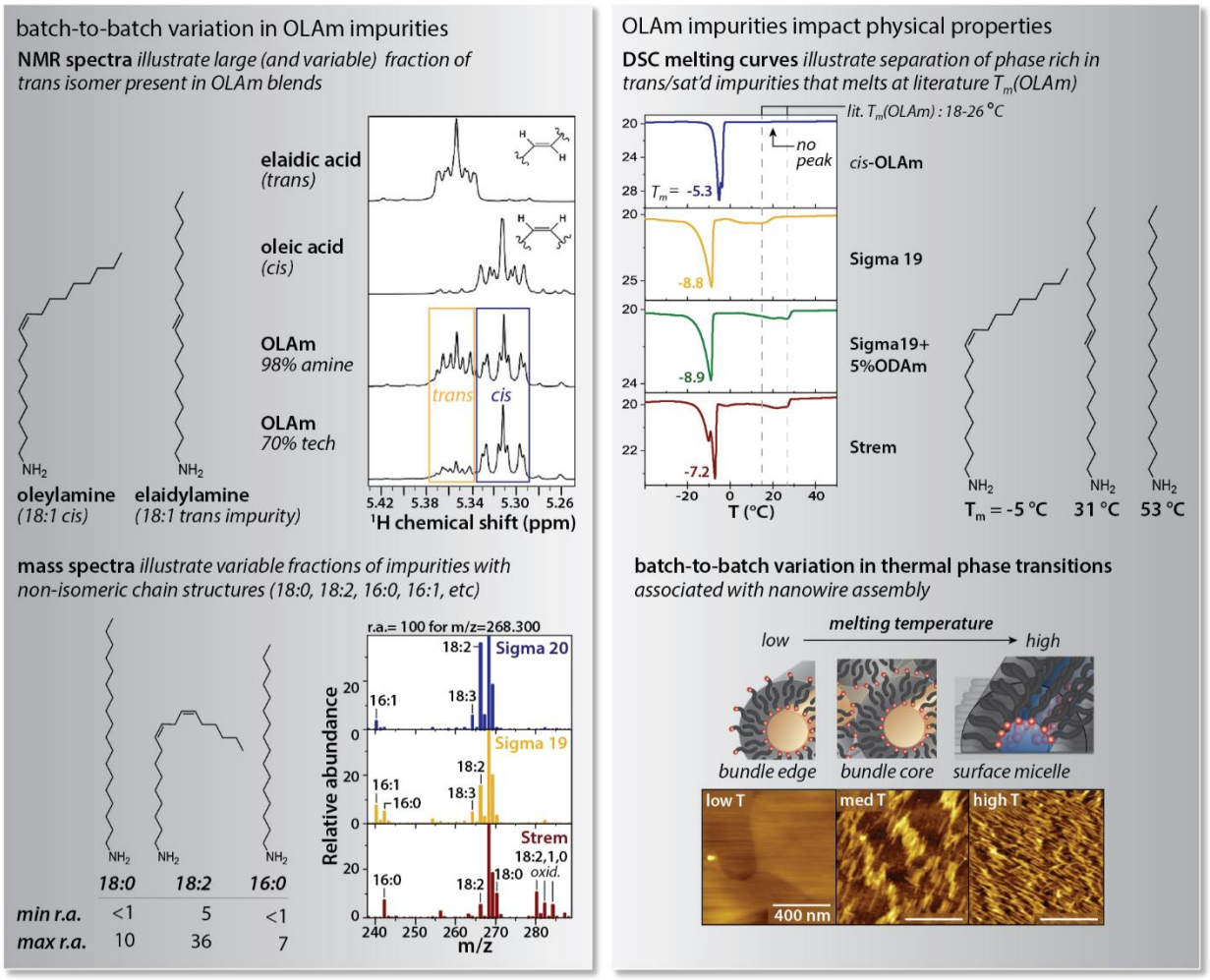

Figure 2.2. Characterization of common impurities in technical-grade OLAm, and impacts on nanocrystal assembly. Reprinted with permission.[16] Copyright © 2019, American Chemical Society. Further permissions related to the excerpted material should be directed to the ACS.

The melting temperature (T_m) for OLAm is typically reported as 18°C–26°C;[25, 26, 55] the wide temperature range is consistent with the variable composition of the technical-grade reagent. Interestingly, even the CRC Handbook reports a value of 25 °C for 'oleylamine' (without commenting on whether this refers to the technical grade).[55] In general, alkyl carboxylic acids have melting transitions 10°C–20°C higher than structurally equivalent alkylamines (e.g. T_m(elaidic acid) = 45 °C, T_m(elaidylamine) = 31 °C and T_m(octadecanoic acid) = 69 °C, T_m(octadecylamine) = 53 °C). Given that T_m(oleic acid) = 13 °C, the reported T_m for OLAm is surprisingly high in comparison.[27]

In a recent set of experiments,[17] we had noticed temperature-dependent differences in gold nanowire (AuNW) assembly when using different bottles of OLAm for nanowire synthesis, and were interested in whether this might reflect batch-to-batch differences in the alkylamine impurities. Synthesizing pure OLAm as a reference, we found that T_m(OLAm) ≈ −5 °C via differential scanning calorimetry (Figure 2.2, upper right panel, blue trace). In contrast, thermograms for different batches of technical-grade OLAm exhibited multiple endothermic peaks (Figure 2.2, upper right panel, gold, green, and red traces). One peak appeared at slightly lower temperature (−8 °C to −10 °C) than that of pure *cis*-OLAm, presumably representing *cis*-OLAm with small amounts of alkyl impurities (*e.g.* diene, *trans* and saturated amines). An additional set of overlapping peaks appeared at higher temperatures, notably very similar to the reported T_m range for technical-grade OLAm. The position of the high-temperature peaks could be increased by adding controlled amounts of octadecylamine (green trace). Therefore, it appears that the melting and solidification observed for OLAm in the laboratory are actually those of a phase rich in *trans* and saturated impurities.

Phase separation in OLAm reagents may not be limited to neat reagents, and may extend to reactions using OLAm in solution and at interfaces (*e.g.* nanocrystal surfaces), with impacts to nanocrystal synthesis and assembly. For instance, we found that the alkyl chain composition of OLAm blends can significantly alter temperature-dependent self-assembly processes, and that *trans* and saturated purities are modestly enriched even on the very high curvature surfaces of 2 nm diameter AuNWs. AuNWs synthesized with these blends exhibit substantial blend-to-blend differences in thermally-regulated assembly, producing nematic adsorption at the highest temperatures, ribbon-phase adsorption at intermediate temperatures and a turn-off in adsorption below what appears to be the solidification point of the ligand shell (Figure 2.2, lower right panel). Given the impacts of saturated alkyl ligands on nanocrystal growth in other contexts,[44, 46] phase separation may also impact growth of nanocrystals from technical-grade OLAm, particularly for syntheses carried out at room temperature. We are currently examining some of these questions in our laboratory.

2.5 Prospects for technical-grade reagents

Technical-grade reagents (including oleylamine) will continue to be important in many areas of nanomaterials synthesis. On the one hand, technical-grade reagents have enabled many

synthetic routes that would be impractical with expensive higher-purity reagents. This will become increasingly important as nanocrystals become viable components of commercial devices and processes that require larger-scale synthesis. Additionally, the use of technical-grade reagents represents one route for decreasing environmental costs (energy usage, chemical wastes)[56] associated with unnecessary preparation of high-purity ligands. However, there are also substantial time and material costs associated with reproducing syntheses that, unknown, depend on one or more impurities. Increased ligand shell chemical complexity may also increase challenges related to evaluating biocompatibility if nanocrystals synthesized with technical-grade blends are used in applications including biochemical probes and biomedical diagnostics (MRI contrast or optical labeling).[51]

We would argue that the most reasonable step toward addressing reproducibility challenge would involve (a) suppliers providing routine access to basic information on composition (*e.g.* mass spectra, relevant NMR spectra) for each lot number on their websites, and (b) lot number reporting in literature synthetic protocols. Over time, this approach would improve reproducibility, as it would allow researchers to compare the composition of their reagent with that of a reagent from another lab, potentially titrating the blend to match concentrations of specific impurities (*e.g.* saturated chains). Alternatively, synthesis temperature could be adjusted relative to impurity phase transitions for different blends.

Supplier-provided compositional information would facilitate selection of reagents, which can sometimes be difficult based on terminology used to qualify purity (*e.g.* '95% primary amine'). And although most synthetic protocols will continue to rely on technical grades, commercial availability of high-purity OLAm and ELAm would help researchers develop an understanding of the levels of reagent control that are needed for synthetic reproducibility, similar to control developed for synthesis with other reagents such as TOPO.

CHAPTER 3. OLEYLAMINE IMPURITIES REGULATE TEMPERATURE-DEPENDENT HIERARCHICAL ASSEMBLY OF ULTRANARROW GOLD NANOWIRES ON BIOTEMPLATED INTERFACES

A version of this chapter has been published in *ACS Nano*
DOI: 10.1021/acsnano.1c02414

3.1 Introduction

Nanocrystals are often synthesized utilizing low-purity technical-grade reagents (*e.g.*, trioctylphosphine oxide, oleylamine),[28, 51] enabling synthesis in useful quantities. For functional alkanes used in nanocrystal synthesis, technical blends often contain significant fractions of molecules with different alkyl chain structures. In a number of cases, minor components of reagent blends have been shown to modulate particle morphology (*e.g.*, based on selective coordination of nanocrystal facets).[18, 19, 28, 29, 42, 57] However, the exposed alkyl chains in ligand shells composed of blended reagents may also generate surprisingly sophisticated function. For instance, in cell membranes, mixtures of chains undergo local phase segregation and ordering transitions,[58, 59] orchestrating protein clustering and membrane curvature and generating cellular signaling cascades.[60-63] This raises the possibility that similar levels of control might ultimately be achieved over mesoscale nanocrystal assembly using related approaches.

Oleylamine (OLAm, 9-*cis*-octadecenamine) is widely used as a nanocrystal ligand.[51, 64] Typically, it is used as a technical (70% purity) grade, consisting of the unsaturated *cis*-isomer (oleylamine) as well as significant quantities of a *trans* isomer (elaidylamine, ELAm) and small amounts of chains with different lengths and degrees of unsaturation (*e.g.*, octadecylamine (ODAm), hexadecylamine (HDAm)).[16, 51, 65] The literature variously describes the melting temperature (T_m) of OLAm as being in the range from 18–26 °C.[25, 26, 55] Although composition is generally not explicitly described, this seems likely to describe the blend—the T_m of oleic acid is 13.4 °C, and melting temperatures of amines are typically several degrees lower than those of equivalent carboxylic acids, which can form strong H-bonded dimers. Thus, the reagent should represent a mixture of high-T_m impurities (e.g., T_m(ODAm) = 53 °C) (17) with a lower-T_m main component (OLAm).

While the phase behavior of oleylamine has not been well-explored, oleic acid (OLAc, 9-*cis*-octadecenoic acid), is the most prevalent fatty acid in biology, and its phase behavior alone and in mixtures has been well-studied.[66-69] For instance, previous DSC studies of binary mixtures of OLAc with its *trans*-isomer (elaidic acid, ELAc)[66] and with stearic acid (18:0-COOH, STAc)[67] have indicated that the straighter chains exhibit very limited miscibility with OLAc, with eutectics at 15:85 for ELAc/OLAc and 5:95 for STAc/OLAc.[66]

Thus, it would be reasonable to predict that technical-grade OLAm blends and/or ligand shells may exhibit related phase separation and thermal transitions, potentially impacting nanocrystal synthesis and assembly. It has been known for many years that saturated alkanethiol ligand shells on gold nanospheres undergo thermal order–disorder transitions.[70-72] For spherical particles, ligand shell ordering can drive aggregation in solution[73-75] and decreases in the photoluminescence of semiconductor quantum dots,[76] with transition temperatures increasing for mixed ligand shells comprised of OLAc and octadecylphosphonic acid (ODPA) as the fraction of ODPA increases.[77] One recent study indicates that alkyl chain interactions can in fact represent the primary driver of aggregation behavior in small spherical nanocrystals with core diameters <8 nm;[75] such interactions also play a role in assembly of small spherical nanoparticles at interfaces.[78, 79] Theory predicts that ligand shell phase transitions would also be important in contact-mediated assembly of nanorods, particularly in poor solvents.[80]

Here, we show that OLAm-capped gold nanowires (AuNWs, diameters = 1.5–2 nm)[49, 81-83] in cyclohexane undergo complex, temperature-dependent hierarchical assembly at an interface, directed by both an amphiphilic template on the substrate[11] and also by phase transitions in the alkyl ligand mixture (Figure 3.1). The observed assembly behavior in our system varies sensitively with the blend composition of alkyl chains and bridges characteristic length scales from <10 nm to >100 μm. Our results demonstrate that mixtures of alkyl ligands exhibit powerful directing effects. These can be utilized in tandem with other directors (here, polarization of nanostructures in low-dielectric solvents) to generate complex hierarchical assembly regulated by ligand blend and differences in physical environments occupied by the ligands.

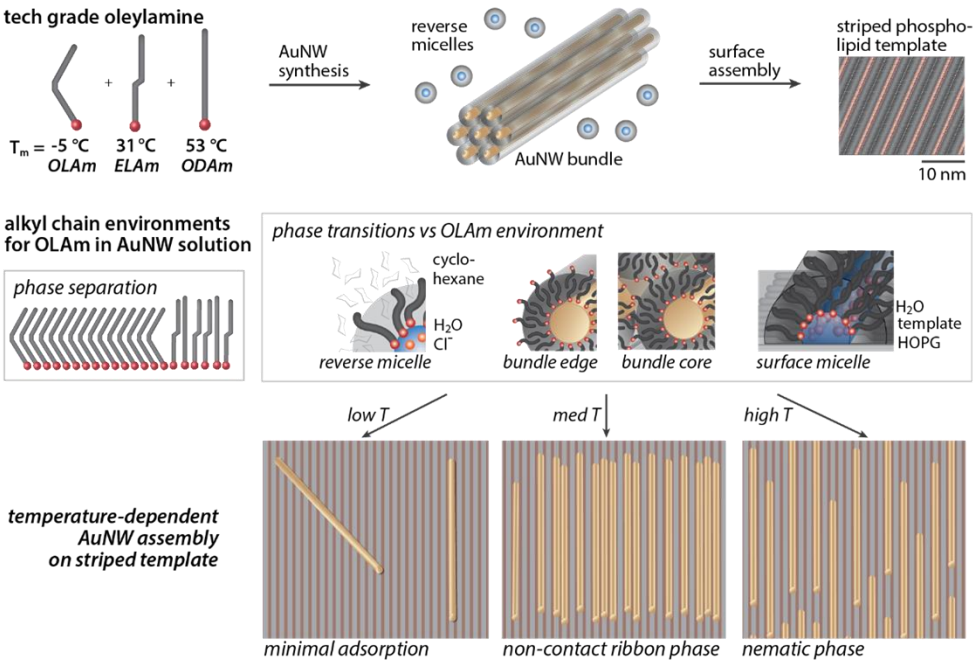

Figure 3.1. Schematic of technical-grade OLAm blend composition impacts on temperature-dependent AuNW assembly.

3.2 Results and discussion

3.2.1 Preparation and characterization of dPE monolayers on HOPG

Striped phospholipid surfaces[7, 10, 84] on highly ordered pyrolytic graphite (HOPG, Figure 3.2) provide a useful templating mechanism for controlling assembly of OLAm-capped AuNWs,[11] of particular relevance to examining thermal impacts of *trans* and saturated chains in OLAm blends. Striped phases of functional alkanes (*e.g.*, phospholipids) assemble on materials such as HOPG via drop-casting from organic solvent[4, 8] or through Langmuir–Schaefer conversion[84-86] (see Experimental Methods). In striped phases, alkyl chains assemble parallel to the substrate,[4-6, 9] stabilized by a combination of alkyl–π interactions and lateral interactions between alkyl chains within the layer. Surfaces prepared in this way resemble a repeating cross section of a lipid bilayer, with 1 nm wide stripes of polar headgroups alternating with ~5 nm of exposed alkyl chains oriented parallel to the HOPG surface. For diyne phosphoethanolamine (dPE), the molecular model illustrates a lamellar edge-to-edge distance of 6.2 nm (Figure 3.2a,b) commensurate with a periodicity of 6.4 nm observed in AFM images (Figure 3.2c). Molecular rows order in epitaxy with the hexagonal HOPG lattice, resulting in 120° angles between domains (Figure 3.2d); long-range ordering of molecular rows (domain sizes >10 μm edge length), visible in SEM images

(Figure 3.2e and Appendix A), provides a means of structuring assembly of AuNWs.[11, 12] In the initial assembled monolayer, rows of diacetylene groups align (Figure 3.2a); photopolymerization via UV irradiation[8, 9, 87] generates polydiacetylene (PDA) backbones that tether together molecules along each row, stabilizing the surface for solution phase assembly experiments such as those described below.

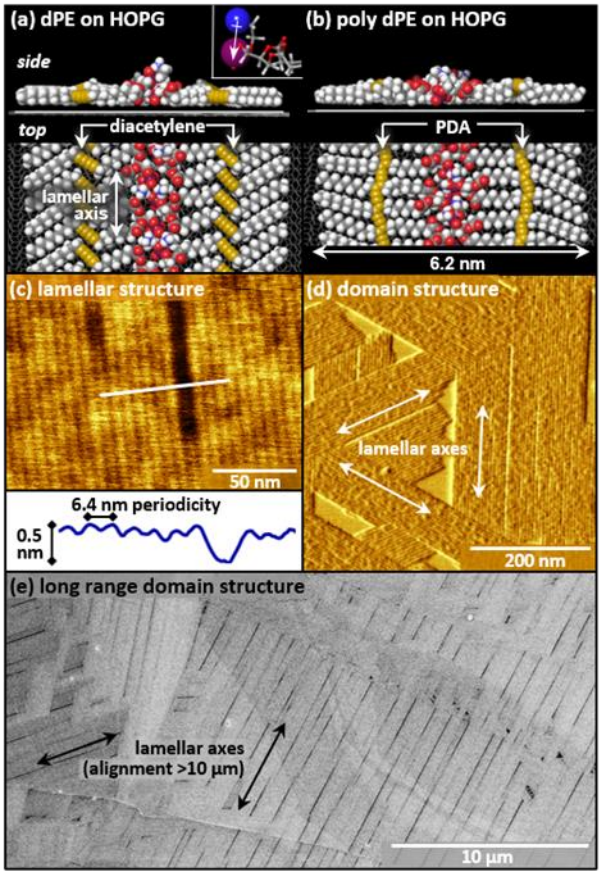

Figure 3.2. (a,b) Molecular models of (a) unpolymerized and (b) polymerized dPE on HOPG. Inset of (a) shows orientable headgroup dipole. (c,d) AFM images illustrating the (c) lamellar and (d) domain structure in dPE monolayers. (e) SEM image illustrating microscale ordering in a dPE monolayer.

Pertinent to local chemical environments impacting thermally regulated assembly, alkyl–π interactions between alkyl chains in the template monolayer and the HOPG substrate would be expected to increase ordering at elevated temperatures. Previous literature has found that (in the presence of excess adsorbate) striped monolayers on HOPG can have melting temperatures 15–25 °C higher than the bulk transition for the same molecule.[88] Such a difference would also potentially

impact further alkyl chain assembly at the interface, in the AuNW assembly experiments described below.

3.2.2 Synthesis of AuNWs and self-assembly at dPE and HOPG interfaces

AuNWs capped with OLAm were synthesized using modifications to literature procedures[49, 81, 83] (see Experimental Methods for more detail). Briefly, solutions of $HAuCl_4 \cdot 3H_2O$, OLAm, and triisopropylsilane (TIPS) in dry cyclohexane were aged for 12 h, resulting in AuNWs with <2 nm diameter and lengths tunable from <100 nm to >1 μm (Figure 3.3a) by adjusting reagent concentrations.

The AuNW growth solution contains a large excess of OLAm (here, ~250 μmol of OLAm vs. ~6 μmol of Au atoms). The literature suggests that, under these conditions, OLAm forms an interdigitated bilayer around each AuNW.[83] Excess OLAm is also likely to form reverse micelles, stabilizing the ~20 μmol of H_2O and 25 μmol of Cl^- that are byproducts of Au precursor decomposition.[11] Depletion interactions between OLAm ligand shells produce hexagonally packed bundles of AuNWs in solution.[83, 89, 90] When freshly cleaved HOPG substrates are exposed to AuNW growth solution, AuNWs adsorb as bundles on the HOPG surface (Figure 3.3b, see Figure A.1a for a larger image). Adsorption of excess OLAm from the growth solution is also observed (Figure A.1b).

Assembly of AuNWs on striped phospholipid templates yields a distinct morphology. Previously, we have reported a complex assembly process in which excess OLAm from the AuNW growth solution adsorbs around rows of hydrated dPE headgroups forming hemicylindrical micelles (Figure 3.3c) with dPE headgroup dipoles forming arrays.[11] Polarization of AuNWs by dPE headgroup dipoles simultaneously induces attraction of AuNWs to the surface dipole arrays and repulsion between adjacent AuNWs, causing long bundled AuNWs to separate when aligned with the template, though they remain bundled when misaligned (Figure 3.3d,e). The repulsion can persist up to ~28 nm, which is similar to the Bjerrum length for cyclohexane (Figure 3.3c, right). The result is assembly with AuNWs aligned precisely with dPE lamellar axes and center-to-center distances at multiples of the dPE template pitch, with distances twice the template pitch common under high-density coverage conditions and longer distances (Figure 3.3e) when AuNWs can spread more freely on the surface.

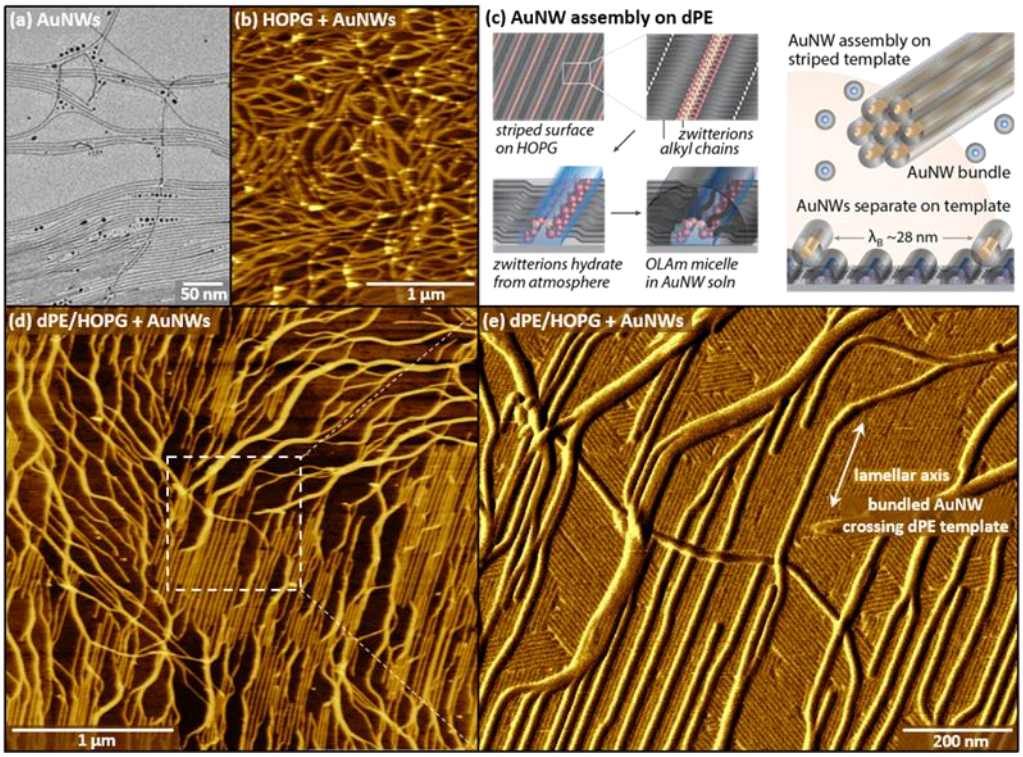

Figure 3.3. (a) TEM image of AuNWs. (b) AFM image of bundled AuNWs deposited on bare HOPG. (c) Cartoon of AuNW assembly on dPE scaffold. (d) AFM image of AuNWs assembled on dPE/HOPG. (e) AFM phase image of highlighted area in (d), showing AuNW alignment relative to dPE stripes.

3.2.3 Assembly morphology transition for short AuNWs

In contrast, assembly of shorter, more mobile, AuNWs on dPE produces two distinct assembly motifs: nematic phases (Figure 3.4a) and ribbon phases (Figure 3.4b). Appendix A Figure A.2 shows larger images illustrating these assembly motifs. Ribbon assembly is observed with as little as 5 s of exposure to as-prepared AuNW solution but does not occur for diluted solutions (Figures A.3–A.5), even with much longer exposure. 2D fast Fourier transforms (2D-FFTs) (insets in Figure 3.4a,b) facilitate comparison of spatial frequencies associated with assembly. When FFT sections perpendicular to the main wire alignment axis for each image are compared (blue lines in insets), the ratio Ampl(N)/Ampl(R) (Figure 3.4c, left panel, comparing nematic (N) and ribbon (R) spatial frequencies) exhibits a peak at ±0.061 nm^{-1}, corresponding with a periodicity of 16.6 nm, approximately twice the template periodicity, while AuNWs in the ribbon phase are more variable, as described below. In the low-spatial-frequency range (Figure 3.4c, right

panel), spectral density is greater for the ribbon phase, in the range corresponding to structural features with 100–400 nm; this is reasonable, given the variable spacing between ribbons.

In contrast with previously reported nanocrystal ribbon phases,[91-94] here in many cases, the AuNWs align laterally *without* contact between ligand shells, consistent with the repulsive interactions we have reported previously for assembly on striped phospholipid templates.[11] However, in contrast with nematic phase assembly (Figure 3.4a), in some cases, the AuNWs in ribbons (Figure 3.4b) remain in contact, possibly consistent with a limited ability for the AuNWs to separate.

Larger-scale AFM and SEM images (Figure 3.4d–f, see Figures A.6–A.8 for larger images) illustrate ribbon alignment over scales in some cases substantially exceeding 10 μm. Thus, the adsorption process leading to ribbon formation likely involves sequential adsorption of many AuNW bundles.

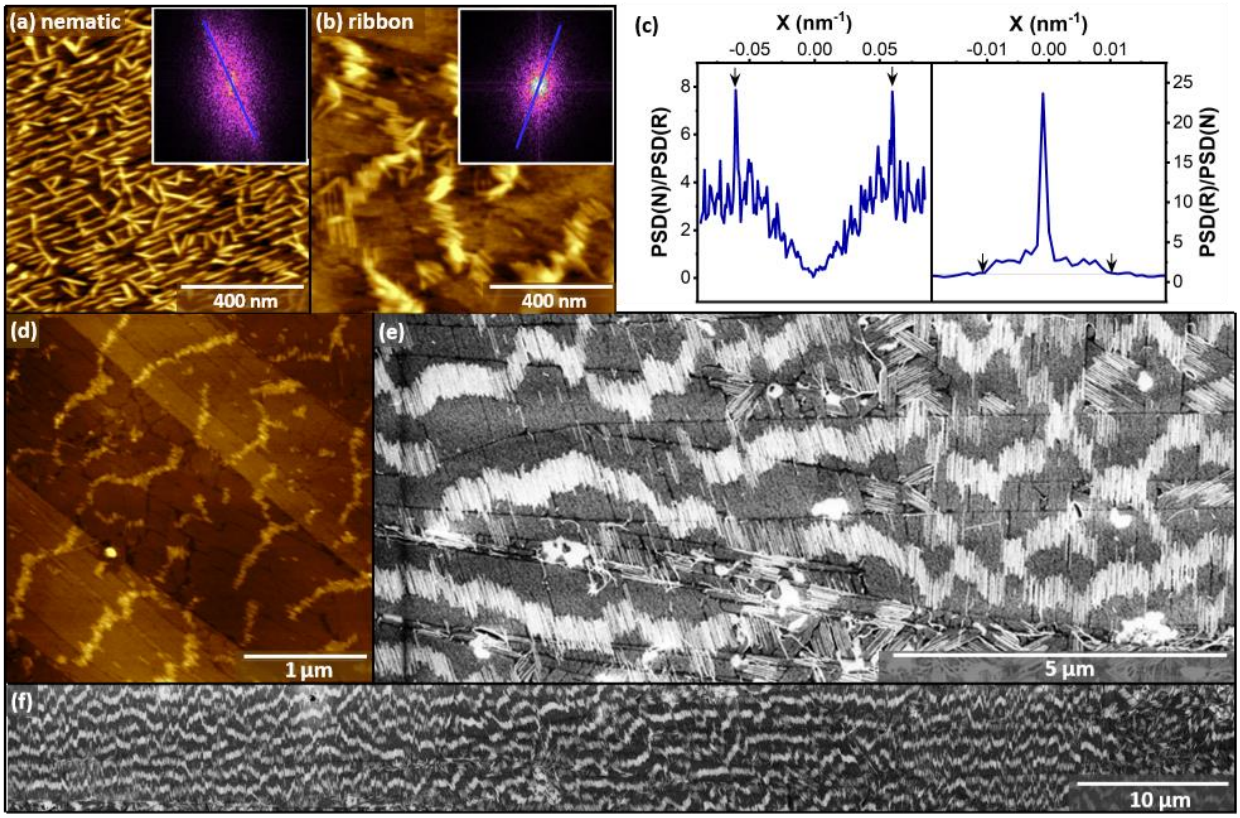

Figure 3.4. (a,b) AFM images and center regions of 2D-FFTs for (a) nematic and (b) ribbon phase assemblies of AuNWs on dPE templates. (c) Ratios of linear sections from 2D-FFTs in (a) and (b). (d) AFM and (e,f) SEM images illustrating AuNW alignment in ribbon phases.

The assembly of ribbon *vs.* nematic phases varied substantially based on the batch of OLAm reagent used in synthesis (Figure 3.5). We compared two batches of technical-grade OLAm from Sigma-Aldrich, procured in 2019 and 2020 (Sig19, and Sig20, respectively) with a reagent procured from Strem. Temperature-controlled experiments revealed that AuNW assembly was temperature-dependent (Figures 3.5a and A.9), with a ribbon-to-nematic transition temperature ($T_{R\rightarrow N}$) that was typically near room temperature for Sig19 and Sig20 but above 50 °C for the Strem OLAm (Figure 3.5a, bottom right). At a lower threshold temperature ($T_{O\rightarrow N}$), well below room temperature, a turn-off in AuNW adsorption was observed (Figure 3.5a, top). At intermediate temperatures, slightly above $T_{O\rightarrow N}$ but below the ribbon onset temperature, we observe nematic assemblies. The transition from low-temperature nematic to ribbon ($T_{N\rightarrow R}$) occurs at a higher temperature for Strem than for Sig19.

To understand whether differences in OLAm blend composition were correlated with differences in $T_{O\rightarrow N}$, $T_{N\rightarrow R}$, and $T_{R\rightarrow N}$, we characterized the OLAm blends by high-resolution mass spectrometry (MS, Figure 3.5b), nuclear magnetic resonance (NMR, Figure 3.5c), and differential scanning calorimetry (DSC, Figure 3.6). In mass spectra for all three blends (Figure 3.5b), a peak at m/z = 268.300 appears with a relative abundance (r.a.) of 100, corresponding to the mass of OLAm, with an isotopic peak at 269.303 having an r.a. ≈ 20. To facilitate comparisons between lower-abundance peaks, mass spectra in Figure 3.5b are truncated at r.a. = 29; see Appendix A Figures A.10–A.12 for full spectra and tables of masses.

The most abundant single impurity in commercial OLAm blends is typically elaidylamine (ELAm), the *trans* isomer of 1-aminooctadec-9-ene, which has the same mass as OLAm and is not distinguishable by MS. The relative abundances of OLAm and ELAm can be approximated based on integrated NMR peak intensities for allylic and vinylic protons (Figure 3.5c, see Figures A.14–A.17 for full spectra), which produce distinct resonances for *cis* and *trans* alkene configurations. Analysis of peak areas (see Appendix A) results in approximated *cis/trans* ratios of 3.5:1 for Sig20, 3.6:1 for Sig19, and 2.6:1 for the Strem blend, meaning that the Strem blend is enriched in the higher-melting *trans*-isomer.

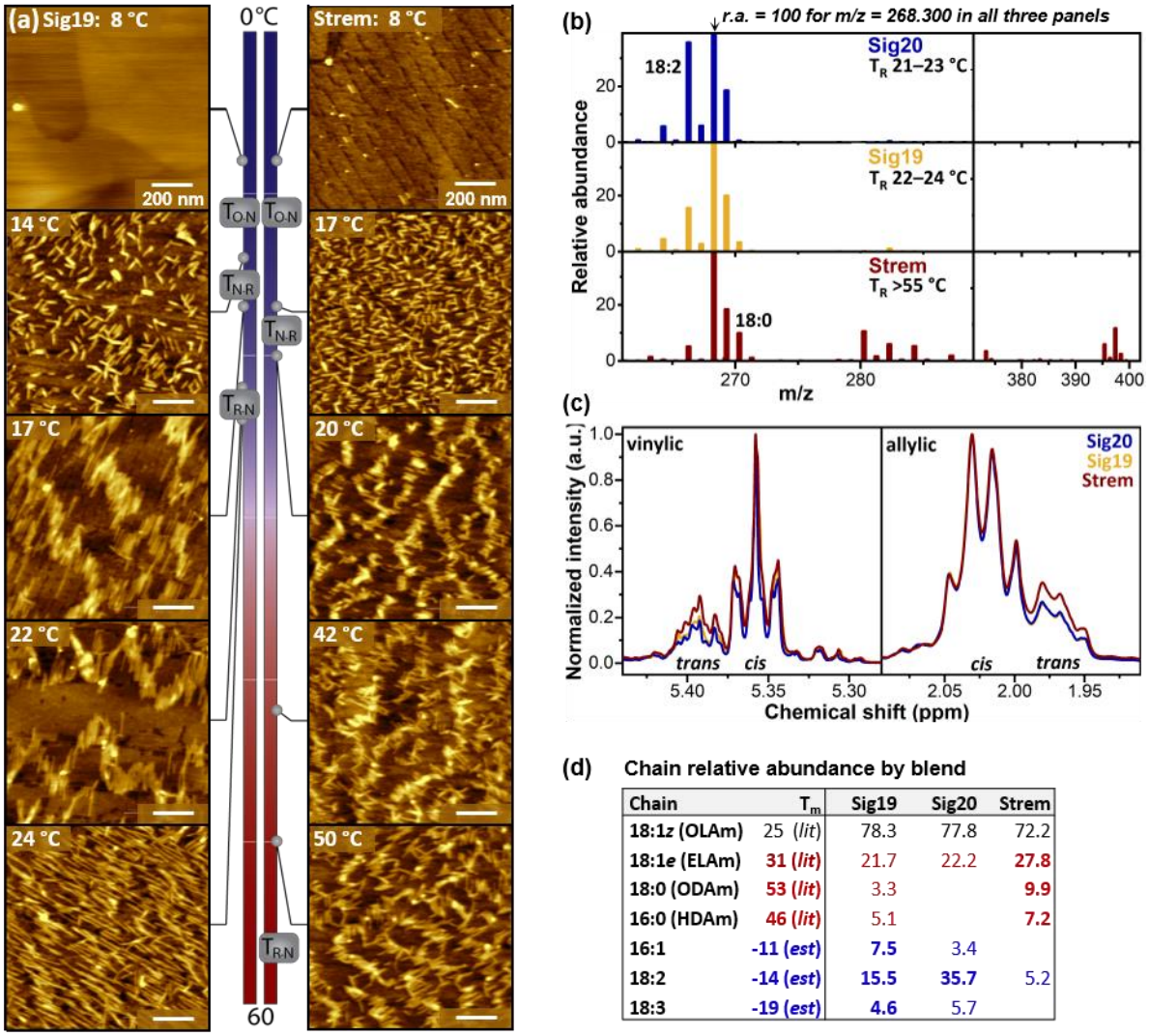

(d) **Chain relative abundance by blend**

Chain	T_m	Sig19	Sig20	Strem
18:1*z* (OLAm)	25 (*lit*)	78.3	77.8	72.2
18:1*e* (ELAm)	31 (*lit*)	21.7	22.2	27.8
18:0 (ODAm)	53 (*lit*)	3.3		9.9
16:0 (HDAm)	46 (*lit*)	5.1		7.2
16:1	-11 (*est*)	7.5	3.4	
18:2	-14 (*est*)	15.5	35.7	5.2
18:3	-19 (*est*)	4.6	5.7	

Figure 3.5. (a) AFM images illustrating that assembly morphology depends on both the temperature and batch of OLAm used in AuNW synthesis for Sigma (Sig19) and Strem OLAm (see Figure A.9 for images at additional temperatures). Colored bars illustrate temperature ranges associated with changes in assembled morphology. (b) Mass spectra for three commercial OLAm blends, truncated at r.a. = 29 to illustrate differences in impurity concentrations. (r.a. of the peak at 268.300 is 100 for all three spectra. See Appendix A for full spectra). (c) ^{1}H NMR spectra of allylic and vinylic proton regions. (d) Tabulated abundances of common alkyl chain impurities, utilizing quantifications of 18:1 z (*cis*) and 18:1 e (*trans*) based on NMR peak integration (see Appendix A for calculations), with literature[27, 55, 95] or estimated melting temperatures (see Appendix A).

The table in Figure 3.5d quantifies the relative prevalences of common OLAm impurities in the mass spectra of the OLAm blends; in making this comparison, the total abundance of the MS peaks at *m/z* = 268.300 and 269.303 was distributed between OLAm (18:1 z) and ELAm (18:1

e) according to NMR peak ratios calculated above. For reference, literature melting points[27, 55] for each substance are tabulated, where available; values for some impurities were approximated in relation to structurally analogous carboxylic acids, in the absence of literature values for the amine (see Figure A.18). The value for pure *cis*-OLAm was also measured here by DSC (*vide infra*), yielding a different value than the reported literature value.

Overall, the relative prevalence of high-T_m and low-T_m impurities in the blends appears consistent with the higher value of $T_{R\rightarrow N}$ observed for the Strem blend. The composition of the Sig19 OLAm blend reflects with reasonable accuracy the composition described in previous literature[65] with relative abundances (r.a.) of ∼3 for octadecylamine (ODAm, 18:0) and 5 for hexadecylamine (HDAm, 16:0) impurities. By comparison, the Sig20 blend contains less of these high-T_m impurities (r.a.(18:0) ≪ 1 and r.a.(16:0) ≈ 0.1), while Strem contains more (r.a.(18:0) ≈ 10 and r.a.(16:0) > 7). Conversely, Sig20 is enriched in one of the low-T_m polyunsaturated chains (r.a.(18:2) ≈ 42, in comparison with a value of ∼16 for Sig19), while in the Strem blend, the low-T_m chains are less abundant (r.a.(16:1) and r.a.(18:3) < 2, r.a.(18:2) ≈ 5). The Strem blend also contains impurities with masses consistent with oxidation (*e.g.*, 280.265, mass consistent with $C_{18}H_{34}NO$),[16] which may further impact physical properties.

3.2.4 Phase transitions of *cis*-OLAm

Differences in blend composition impact phase transitions measured by DSC, for pure OLAm synthesized from OLAc (see Experimental Methods for synthetic protocols and Figures A.13 and A.17 for the mass spectrum and NMR spectrum) and for OLAm blends.

The T_m for OLAm is described in a variety of sources as 18–26 °C.[25, 26, 55] However, the melting thermogram for pure *cis*-OLAm (Figure 3.6, blue trace) exhibits a pair of overlapping endothermic peaks at −5.3 and −3.7 °C. Based on thermograms for the more broadly studied OLAc, the lower-temperature peak may correspond to disordering of the terminal chain segments (described as a γ–α transition and occurring at −2.6 °C for OLAc).[96] OLAc also exhibits a higher-temperature α–L transition near 13 °C, corresponding to disordering of chain segments adjacent to the COOH headgroups and loss of dimerization between opposing COOH groups.[96] In contrast, for pure *cis*-OLAm, no distinct transition above 0 °C is observed; we suggest that the peak centered at −3.7 °C may be equivalent to the α–L transition for OLAc, occurring at a lower temperature due to the weaker H-bonding between amines in comparison with COOH dimers.

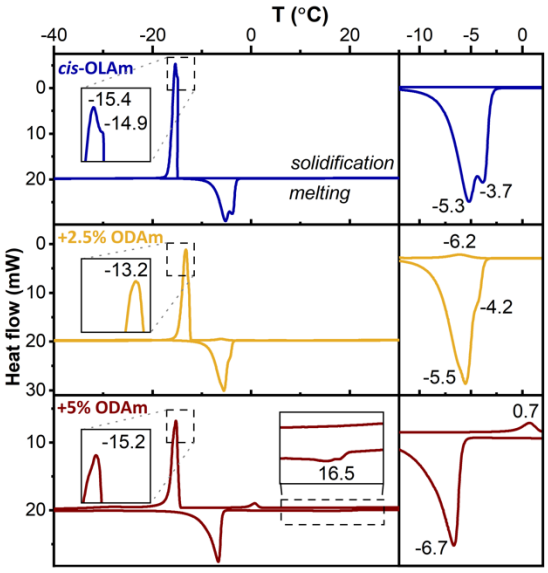

Figure 3.6. DSC thermograms for pure *cis*-OLAm (blue) and pure *cis*-OLAm with 2.5% (gold) or 5% (red) ODAm.

3.2.5 Phase separation of OLAm blends

The commonly reported T_m for OLAm is 20–30 °C higher than our observed T_m of pure *cis*-OLAm; therefore, we examined whether phase separation might play a role in the observed thermal transitions. Previous DSC studies of binary mixtures of OLAc with its *trans* isomer (elaidic acid, ELAc)[66] and with its saturated analogue (stearic acid, STAc)[67] have indicated that the straighter *trans* and saturated (T/S) chains exhibit limited miscibility with OLAc, with eutectics at 15:85 for ELAc/OLAc and 5:95 for STAc/OLAc.[66] This leads to distinct peaks in DSC thermograms for phases rich in T/S chains. Thus, it would be reasonable to expect OLAm and its saturated and *trans* analogues to exhibit similar behavior.

DSC thermograms of OLAm with the addition of controlled amounts of (commercially available) ODAm (Figure 3.6, lower panels) provide a useful starting point for interpreting thermograms from more complex OLAm blends including multiple alkylamine impurities. With the addition of 2.5% ODAm (Figure 3.6, gold traces), a small additional solidification peak emerges at −6.2 °C. With 5% ODAm (Figure 3.6, red traces), the secondary peak shifts to higher temperature, with a maximum near 0.7 °C, and a broad, shallow feature with a maximum near 16.5 °C appears in the melting thermogram.

Commercial blends of OLAm also exhibit higher-temperature transitions similar to those in the *cis*-OLAm/ODAm blends (Figure 3.7a) and in a range similar to commonly reported melting temperatures of OLAm. Secondary melting peaks appear near 17 °C for the two Sigma blends (Sig19 shown in Figure 3.7a, gold trace) and at 26 °C for the Strem blend (red trace). Addition of ODAm to the Sig19 reagent (green trace) shifts the secondary peaks into a range similar to that for the Strem blend. Thus, we suggest that the higher-temperature phase transition in the OLAm blends represents a phase that is predominantly T/S chains. This would be consistent with the observation that the transition occurs at a higher temperature for the Strem blend, which contains larger fractions of both *trans* and saturated chains in comparison with the Sigma blends.

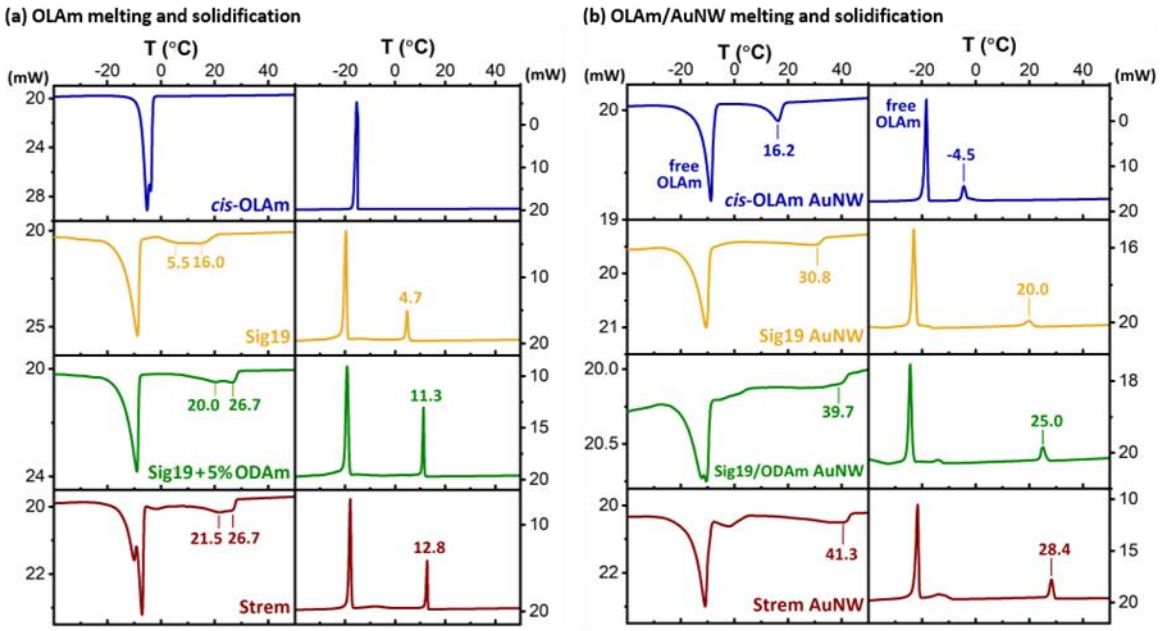

Figure 3.7. DSC melting (left) and solidification (right) thermograms, for (a) four different OLAm compositions, and (b) AuNW solids prepared from the same OLAm compositions.

3.2.6 DSC thermograms of AuNW solids

Thermograms for AuNW solids provide possible insight into the ligand chemistry of nanowires grown using OLAm blends. Figure 3.7b shows thermograms for AuNW solids (AuNW growth solution deposited in the DSC pan; solvent allowed to evaporate) for comparison with those of the batches of OLAm used to prepare the AuNWs (Figure 3.7a). In each AuNW melting or solidification thermogram, a peak is visible above the main *cis*-OLAm transition; its temperature

varies based on the batch of OLAm used in synthesis. For AuNWs synthesized from pure *cis*-OLAm (Figure 3.7b, blue), this is a new peak (T_m = 16.2 °C, T_s = −4.5 °C), centered ∼15 °C higher than the original *cis*-OLAm peak. Because this peak is not present in the pure *cis*-OLAm (Figure 3.7a, blue), we suggest it corresponds to complexed *cis*-OLAm. In AuNW growth solution, complexes may include AuNW–ligand, other ligated gold structures such as nanospheres, and/or reverse micelles enclosing water and ions from the gold precursor. The literature suggests that alkylammonium chloride salts are a significant component of AuNW growth solution and may represent as much as half of the ligand shell.[89, 97] We find that the addition of HCl to *cis*-OLAm to form oleylammonium chloride produces a new peak at approximately the same value (T_m = 15.9 °C, Figure A.19). The relative area of the "complex" peak for *cis*-OLAm AuNWs (Figure 3.7b, blue) is 0.18, in comparison with an area of 0.82 for the main *cis*-OLAm peak. Estimating the amount of complexed OLAm as 18% of the 255 μmol of OLAm per reaction yields a value of 46 μmol, similar to the 57 μmol total of polar and ionic species that would be generated by 2.5 mg of gold precursor.

For AuNWs synthesized from each OLAm blend (Figure 3.7b, gold, green, and red traces), temperatures of phase transitions in the complexes are instead offset from the T/S peak for the blend, again shifted upward by ∼15 °C. This relationship is most obvious for the (sharper) solidification transitions (right column) but also holds for the melting transitions (left column). For instance, in the Sig19 blend, the original T_s(T/S) = 4.7 °C (Figure 3.7a, gold), while T_s(complex) = 20.0 °C (Figure 3.7b, gold). The complexed peak temperature also changes in a controlled manner with the addition of ODAm—if 5% ODAm is added to the Sig19, T_s(T/S) = 11.3 °C (Figure 3.7a, green), while T_s(complex) = 25.0 °C (Figure 3.7b, green). Further, in the AuNW solids, the original T/S peak disappears, and in some cases, a much smaller peak appears at lower temperature (at −18.1 and −14.2 °C for Sig19 and Sig19 + 5% ODAm), similar to those for low-percentage ODAm in Figure 3.6. Both of these observations could be consistent with complexation of a large fraction of the T/S chains, with the peaks at −18.1 and −14.2 °C possibly representing small amounts of free T/S chains.

To assess the AuNW ligand shell composition more directly, we harvested AuNWs by centrifugation, removed the Au cores by cyanide etching (see Experimental Methods in Appendix A and Figure A.20), and performed MS on the remaining organic components. While the relative abundance of ELAm is not possible to assess directly in this way, ODAm and HDAm are modestly

enriched in the ligand shells, in comparison with the original reagent (*e.g.*, 9% ODAm in Sig19 AuNWs, compared with 3% ODAm in Sig19 reagent), consistent with impacts of minor alkyl chain components on the AuNW assembly.

3.2.7 Impacts of alkyl chain phase transitions on templated AuNW adsorption

AuNW synthesis and surface assembly generate several distinct chemical environments that may modulate alkyl chain phase transitions (Figure 3.8a), impacting AuNW–substrate interactions and the disassembly of AuNW bundles for ribbon phase formation. Ligand shells on individual AuNWs (Figure 3.8a, left), or on the exterior of AuNW bundles, likely have lower order–disorder transition temperatures in comparison with interior ligands in a AuNW bundle (Figure 3.8a, center) or with micelles formed on the HOPG substrate (Figure 3.8a, right).

Thus, we make the following hypotheses regarding the observed adsorption patterns. (1) Below T_O, ordered AuNW ligand shells weaken interactions with the template (surface micelles and/or enclosed dPE dipole arrays), limiting AuNW adsorption (Figure 3.8a, left). (2) From $T_{O\rightarrow N}$ to $T_{N\rightarrow R}$, the nematic phase may result from disordering of external AuNW ligand shells, permitting adsorption of individual AuNWs (Figure 3.8a, left). If internal ligand shells remain ordered, conflicting attractive and repulsive interactions between AuNWs and template dipoles and between AuNWs in the bundle may act to limit adsorption of bundled wires. (3) At higher temperatures ($T_{N\rightarrow R}$ to $T_{R\rightarrow N}$), disordering of internal ligand shells (Figure 3.8a, center) would allow more rapid disassembly of bundles as attractive and repulsive interactions evolve in conjunction with the substrate, enabling coupled adsorption events. Although multiple factors may contribute to formation of the ribbon phase, we favor the interpretation that it involves reorientation of dPE headgroup dipoles parallel to the substrate and longitudinal polarization of the AuNWs. This would allow for the large vacancies observed between ribbons, if dipoles associated with an existing ribbon serve to activate and deactivate further assembly in the vicinity of the ribbon. (4) At the highest temperatures ($>T_{R\rightarrow N}$), disordering of surface micelles may impact the collective orientation of dipoles in the striped phase for ribbon assembly.

If $T_{R\rightarrow N}$ and $T_{O\rightarrow N}$ relate to order–disorder transitions in the AuNW ligand shells, these values would be expected to be substantially lower for AuNWs synthesized from *cis*-OLAm (T_s near −20 °C for pure *cis*-OLAm and −4 °C for complexed *cis*-OLAm in AuNW solids (Figure 3.7b, blue trace), compared with a T_s of 20 °C for Sig19 AuNW solids (Figure 3.7b, gold trace)).

We carried out additional assembly experiments (Figure 3.8b), establishing that $T_{O\rightarrow N}$ and $T_{N\rightarrow R}$(*cis*-OLAm) < −5 °C and $T_{R\rightarrow N}$(*cis*-OLAm) ≈ 16 °C (Figure 3.8d). We note that pure cyclohexane freezes at 6.5 °C, so the AuNW "solution" used to deposit AuNWs for the −5 °C image is a partly solidified slush. Thus, it was not straightforward to probe lower temperatures to establish values for $T_{O\rightarrow N}$ and $T_{N\rightarrow R}$ with more certainty.

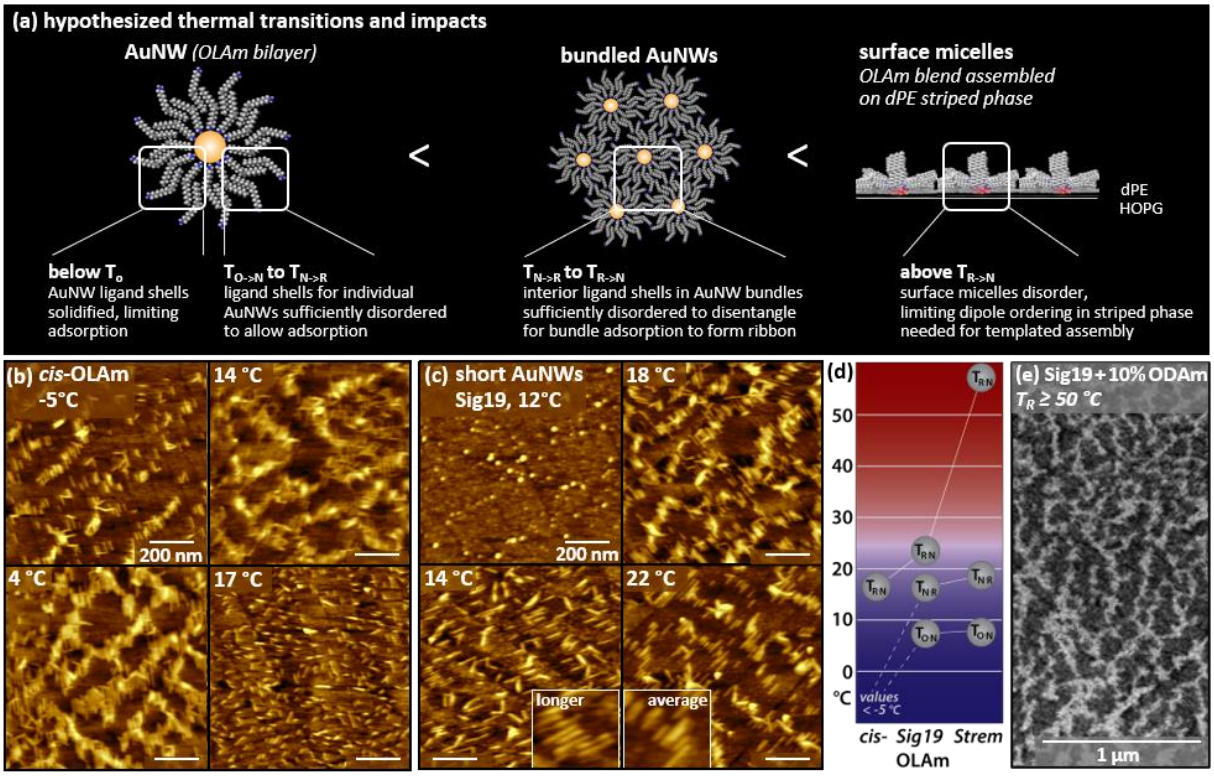

Figure 3.8. (a) Molecular models illustrating OLAm environments proposed to induce differences in assembly transition temperatures. (b) AFM images of low-temperature *cis*-OLAm AuNW ribbon phase assembly. (c) AFM images of assembly of shorter AuNWs synthesized with Sig19 OLAm. (d) Comparison of $T_{O\rightarrow N}$, $T_{N\rightarrow R}$, and $T_{R\rightarrow N}$ for AuNWs synthesized from different OLAm reagents. (e) SEM image showing $T_{R\rightarrow N} \geq 50$ °C for AuNWs synthesized using Sig19 OLAm with the addition of 10% ODAm.

Further, it would be reasonable to expect that shorter AuNWs would exhibit different transition temperatures than longer wires. Shorter wires (56 ± 16 nm) synthesized from Sig19 OLAm assembled in a manner consistent with this prediction (Figure 3.8c), with $T_{O\rightarrow N}$ = 13 °C (vs. 8 °C for longer (95 ± 23 nm) Sig19 AuNWs). The transition to ribbon phase was more similar to that observed for the longer wires, with $T_{N\rightarrow R}$ between 14 and 18 °C. Wires adsorbing in the

nematic phase at 14 °C were above average in length, compared to wires adsorbing in the ribbon phases (compare insets in 14 and 22 °C images).

Finally, the higher-temperature nematic phase transition occurs at a lower temperature for *cis*-OLAm AuNWs (16 °C) in comparison with Sig19 AuNWs (24 °C) and at a substantially higher temperature for Strem AuNWs (>50 °C). The addition of ODAm to the Sig19 blend (Figure 3.8e) elevated $T_{R\rightarrow N}$ to levels similar to that observed for the Strem blend. These differences may be consistent with the different availability of saturated impurities to form surface micelles on the dPE template.

3.3 Conclusions

Nanocrystals are often synthesized with technical-grade alkyl reagents containing a blend of chain structures. These blends of chains can phase separate and/or undergo selective adsorption in heterogeneous environments, producing rich thermally controlled behavior based on alkyl chain phase transitions. Here, we find that pure *cis*-OLAm has a T_m near −5 °C, in contrast with its T/S analogues (ELAm and ODAm), which have T_m values near 30 and 50 °C, respectively.[27, 55] Blends of *cis*-OLAm with these chains phase separate with as little as 2.5% added ODAm; in technical-grade OLAm, this produces a T/S-rich phase with higher T_m and T_s values, in line with values reported previously for OLAm. When OLAm is used in AuNW synthesis, DSC data suggest that a large fraction of the T/S chains may participate in complexes with AuNWs or other species.

AuNWs assembled at amphiphilic interfaces undergo temperature-dependent changes in assembly. At low temperatures (below $T_{O\rightarrow N}$), adsorption of AuNWs becomes very limited, which may result from solidification of AuNW ligand shells. At slightly higher temperatures ($T_{O\rightarrow N}$ to $T_{N\rightarrow R}$), a low-temperature nematic phase is observed, potentially corresponding to increased disorder in ligand shells of isolated AuNWs and those on the exterior of AuNW bundles. From $T_{N\rightarrow R}$ to $T_{R\rightarrow N}$, ribbon phase assemblies are observed, which we suggest require disordering of ligand shells within AuNW bundles so they may separate rapidly during adsorption. Consistent with this possibility, AuNWs synthesized with pure *cis*-OLAm maintain ribbon phase formation at temperatures as low as −5 °C, assembling from the partially frozen cyclohexane solvent. At elevated temperature (>$T_{R\rightarrow N}$), a transition back to nematic assembly is observed; we suggest that $T_{R\rightarrow N}$ relates to disordering of hemicylindrical alkylamine surface micelles that form spontaneously on the striped dPE template when exposed to the AuNW solution.

Overall, these experiments point to the capability to actively use the blending of alkyl chains to control temperature-dependent nanocrystal assembly, analogous to phenomena such as lipid raft formation, in which differences in alkyl chain structure induce complex biological processes. Simultaneously, these experiments also highlight the need for routine access to information on alkyl chain composition in blended reagents such as OLAm, since minor alkyl chain fractions dominate physical properties such as apparent T_m.

3.4 Experimental methods

3.4.1 Materials

Ammonium hydroxide solution (28.0–30.0% NH_3 basis), oleylamine (OLAm, technical grade, 70%), triisopropylsilane (TIPS, 98%), oleic acid (OLAc, ≥99%), lithium aluminum hydride (95%), octadecylamine (ODAm, ≥99%), oxalyl chloride (98%), manganese(II) chloride tetrahydrate (≥99%), chloroform, anhydrous diethyl ether, and molecular sieves (4 Å) were purchased from Sigma-Aldrich (Saint Louis, MO) and used as received. Oleylamine (min 95%) was purchased from Strem Chemicals (Newburyport, MA) and used as received. Diethyl ether, dichloromethane (DCM), dimethylformamide (DMF), sodium sulfate, and sodium chloride were purchased from Fisher Scientific (Fair Lawn, NJ) and used as received. Dry cyclohexane (99.5% extra dry, Acroseal) and tetrachloroauric acid trihydrate (ACS reagent grade) were purchased from Acros Organics (Fair Lawn, NJ) and used as received. Sodium cyanide (98%) was purchased from Alfa Aesar (Haverhill, MA) and used as received. 1,2-Bis(10,12-tricosadiynoyl)-sn-glycero-3-phosphoethanolamine (dPE, >99% purity) was purchased from Avanti Polar Lipids (Alabaster, AL).

3.4.2 Langmuir-Schaefer (LS) conversion of amphiphile monolayers

LS conversion of standing phase Langmuir films to striped phase assemblies on HOPG was performed using a Kibron (Helsinki, Finland) MicroTrough XL, as previously reported.[7, 10] Typically, onto a subphase of 5 mM $MnCl_2$ in water at 30 °C, 45 μL of a 0.6 mg/mL solution of dPE in $CHCl_3$ was deposited. In order to allow the spreading solvent to evaporate, the trough was allowed to equilibrate for 30 min before the trough barriers were compressed at a rate of 6 mm/min. Upon reaching the desired monolayer packing density, a freshly cleaved HOPG substrate was

heated to 70 °C using a custom-built thermally controlled dipping apparatus reported previously (63) and then lowered into contact with the subphase for 2 min to facilitate LS conversion of the phospholipid monolayer. Transfer was typically carried out at a surface pressure of 30 mN/m. Upon withdrawal from the subphase, the substrate was dried under N_2. The resulting dPE monolayers were then photopolymerized by UV irradiation (254 nm) for 1 h.

3.4.3 AuNW synthesis

AuNW synthesis was carried out using procedures adapted from the literature.[49, 81-83] Typically, the reaction flask was charged with molecular sieves, 2.5 mg of $HAuCl_4 \cdot 3H_2O$, and 5.8 mL of dry cyclohexane. Oleylamine (84 μL) was added, followed by brief agitation of the solution using a vortex mixer. Triisopropylsilane (120 μL) was added, and the solution was mixed until the $HAuCl_4 \cdot 3H_2O$ was dissolved. The reaction mixture was moved to a humidity-controlled chamber to age 12 h at ambient temperature. For experiments using longer AuNWs, the same procedure was carried out using a smaller volume of cyclohexane.

3.4.4 AuNW assembly

For AuNW assembly, monolayers of dPE on HOPG substrates were lowered into contact with the AuNW growth solution. The temperature of the growth solution was maintained by equilibrating in a water bath held at the desired temperature for 5 min prior to introducing the substrate; the growth solution was maintained at constant temperature throughout the AuNW adsorption process using a water bath. A mixture of ammonium chloride and ice (1:3 ratio of salt to ice) was used for assembly of *cis*-OLAm AuNWs at −5 °C. Upon removal of the HOPG substrates from the growth solution, they were rinsed with 1 mL of cyclohexane and dried under a stream of N_2.

3.4.5 AFM imaging

AFM measurements were collected under ambient conditions in tapping mode using an Agilent (Agilent Technologies, Santa Clara, CA) 5500 AFM equipped with a MikroMasch (MikroMasch, Tallinn, Estonia) HQ:NSC18/No–Al AFM probe (nominal force constant 2.8 N/m, radius < 8 nm).

3.4.6 Image analysis

Gwyddion scanning probe microscopy data visualization and analysis software was used to perform plane flattening, median line corrections, and contrast adjustments.

3.4.7 DSC

DSC thermograms were acquired using a PerkinElmer (PerkinElmer, Waltham, MA) Jade DSC. A temperature scan rate of 2 °C/min was employed for all scans unless otherwise noted. Samples were contained in PerkinElmer volatile aluminum DSC pans. A DSC pan packed with aluminum was used as the reference; sufficient aluminum was added so that the mass of the reference pan was 100–110% of the mass of the loaded sample pan.

3.4.8 NMR

^{1}H NMR spectra were aquired using a Bruker AV-III-400-HD (400 MHz) spectrometer with a 5 mm BBFO Z-gradient SmartProbe (Bruker Corporation, Billerica, MA) using $CDCl_3$ (Cambridge Isotope Laboratories, Tewksbury, MA) as the solvent.

3.4.9 SEM imaging

High-resolution images were acquired using a Teneo VS SEM (FEI Company, Hillsboro, OR). Typically, a working distance of 5–6 mm, beam current of 0.2–0.8 nA, and an accelerating voltage of 5.00 kV in tandem with the in-column Trinity detector T3 led to the best resolution. Substrates were secured onto standard SEM pin stub specimen mounts using conductive carbon tape.

3.4.10 TEM imaging

All TEM imaging was performed on a Tecnai G2 20 (Thermo Fisher Scientific, Hillsboro, OR) with an accelerating voltage of 200 kV and a lanthanum hexaboride (LaB_6) filament. TEM samples were prepared by depositing 6 μL of redispersed gold nanowire solution on a 200 mesh C/Cu grid (Ted Pella, Redding, CA). The solution was wicked from the grid after 10 s.

CHAPTER 4. LIMITED MISCIBILITY OF TRANS AND SATURATED ALKYL CHAIN IMPURITIES IN TECHNICAL-GRADE OLEYLAMINE: IMPACTS ON ANISOTROPIC NANOCRYSTAL GROWTH

4.1 Introduction

Nanocrystals (NCs) are often synthesized using inexpensive technical-grade reagents as organic capping ligands.[15, 18] A number of recent reports have shown that impurities present in the technical grade ligands traditionally used for NC synthesis have significant synthetic outcomes.[15, 18] For instance, impurities with different headgroup chemistry (*e.g.*, dioctyl phosphonic acid impurities in trioctylphosphine oxide)[20, 28] and ionic impurities (*e.g.*, iodide impurities in cetyl trimethylammonium bromide)[19, 42] have been shown to direct anisotropic growth of NCs through selective passivation of specific crystal facets.

Although impurities that directly interact with the nanocrystal surface (through polar headgroups or counterions) have been the most broadly examined, other technical grade ligands (*e.g.*, oleylamine, OLAm) contain large fractions of impurities with the intended headgroups and an alternate alkyl chain structure. Oleylamine (*cis*-9-octadeceneamine) is commonly available as a 70% purity technical grade; the most abundant impurity, present at levels of 15–50%, is elaidylamine (*trans*-9-octadeceneamine, ELAm).[16, 17] Other significant impurities often include saturated octadecylamine (ODAm, <1–15%), and 16-carbon saturated and unsaturated chains. In some cases, reactions with dissolved gases can also generate alternate headgroup structures.[15, 36]

The blends of alkyl chains present in technical grade OLAm have the potential to be significant drivers of morphology and function. Oleylamine is typically derived from natural sources (*e.g.*, through hydrolysis and amination of beef tallow or vegetable oils).[21, 22, 98] Triglycerides in tallow and other fats have alkyl chain structures similar to those of membrane phospholipids; in cell membranes, lipids combining *cis*- and *trans*-unsaturated and saturated chains with large differences in melting temperature[55] and morphology orchestrate many complex functions.[99] Phase separation and order–disorder transitions of alkyl chains drive protein clustering and signaling cascades,[3, 62, 100-102] and alkyl chain morphology is a critical determinant of membrane curvature.[103, 104]

Phase transitions in alkyl ligand shells are important predictors of temperature-dependent aggregation,[70-75] photophysical properties,[76, 77] and interfacial assembly,[17, 79] and may also impact

synthesis. For example, for spherical Au NCs with sufficiently high surface curvature (<8 nm diameter), saturated alkyl ligand order–disorder transitions are the primary driver of particle aggregation in solution.[75] Simple binary mixtures of ligands alter temperature-dependent NC physical properties. Unsaturated oleic acid (OLAc) ligands blended with saturated octadecylphosphonic acid (ODPA) lowered order–disorder transition temperatures for quantum dot ligand shells.[77] Nearest neighbor interactions between alkyl chains determined the thermodynamics of exchanging OLAc for saturated fatty acids with varied chain lengths in ligand shells of InP quantum dots.[105] Recently, we observed that variations in the blend of alkyl impurities in technical-grade OLAm reagents modified temperature-dependent assembly behavior,[17] suggesting a likely role for alkyl chain phase transitions in the ligand shell in more complex mixtures and for anisotropic nanocrystals.

Despite the broad use of technical-grade OLAm in nanocrystal synthesis, relatively little has been reported about the phase behavior of its constituent amines and their mixtures. In contrast, oleic acid (OLAc) is the most common mono-unsaturated fatty acid in biology, and is prevalent in foods, cosmetics, and other products. As a result, phase transitions of binary mixtures of fatty acids have been well-studied.[66-69] These illustrated limited miscibility of elaidic acid (ELAc) and octadecanoic acid (ODAc, also commonly referred to as stearic acid) with OLAc, with eutectics at 85:15 for OLAc:ELAc and 95:5 for OLAc:ODAc.[66] Thus, it would be reasonable both to expect phase separation for alkylamine constituents of technical-grade OLAm, and to question how these impact nanocrystal synthesis.

Here, we synthesize pure OLAm and ELAm, characterizing binary and ternary mixing behavior of these molecules with ODAm (Figure 4.1). We also assess the morphologies and ligand compositions of AuNWs synthesized in the presence of mixtures of C18 alkylamines with controlled chain compositions (Figure 4.1d).

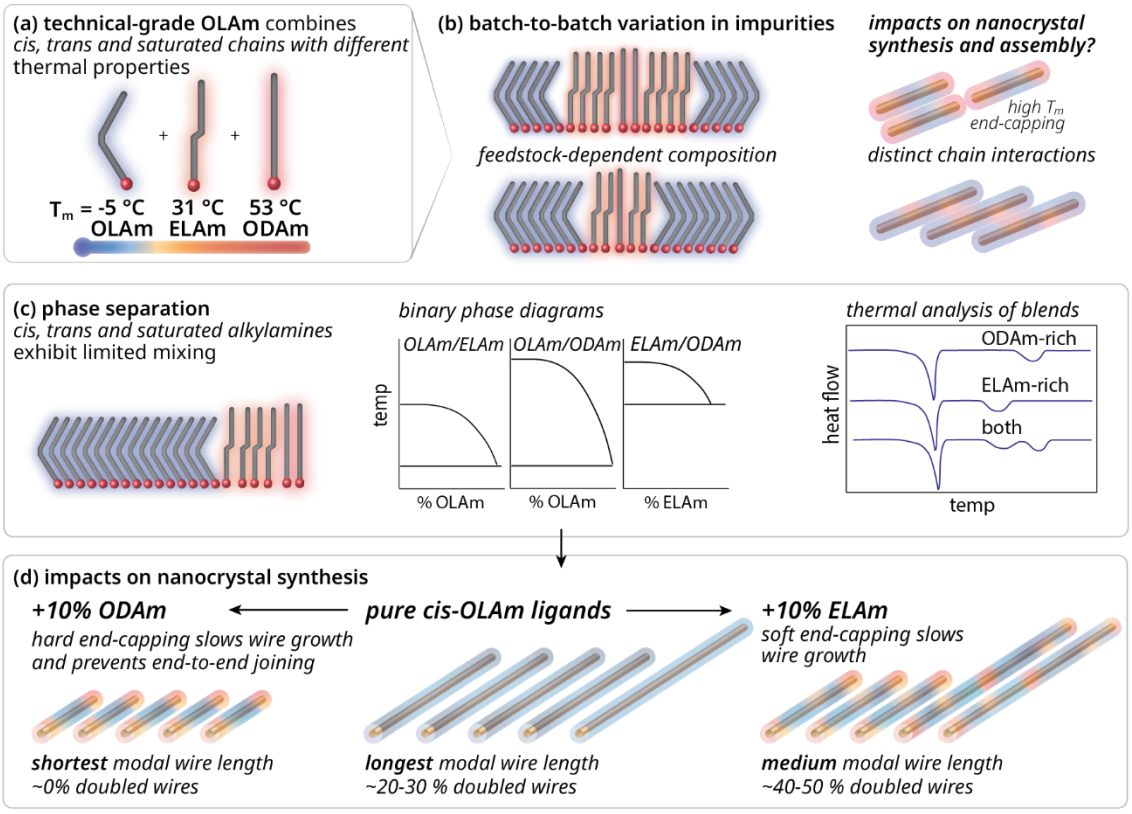

Figure 4.1. Schematic showing cartoon representations of (a) C18 alkylamines present in technical-grade OLAm and their respective melting temperatures (b) variable impurity composition of OLAm reagents and possible outcomes for synthesis and assembly of NCs (c) phase diagrams of binary chain mixtures showing limited miscibility of C18 alkylamines; characterized by DSC (d) control of AuNW synthesis based on chain composition of ligand blend.

4.2 Results and discussion

4.2.1 Binary mixtures exhibit eutectic behavior

Phase transitions of OLAm, ELAm, and ODAm were examined by differential scanning calorimetry (DSC), and phase transition temperatures were plotted against chain composition of binary mixtures to create phase diagrams (Figure 4.2). Thermograms for binary mixtures were eutectic, and reveal limited miscibility of the chains. In each case, the mixing of pairs of amines is less extensive than mixing reported previously for structurally equivalent carboxylic acids,[66] which is reasonable given the weaker H-bonding between headgroups. The phase diagrams illustrate eutectic points of 96:4 for OLAm/ELAm (Figure 4.2a, compare with 85:15 OLAc:ELAc[66]), a limiting case of eutectic behavior for OLAm/ODAm (Figure 4.2b) in which the eutectic

composition is shifted to the limit of pure OLAm (*vs.* 95:5 for OLAc:ODAc[67]), and 87:13 for ELAm/ODAm (Figure 4.2c). Thermodynamic analysis of the calculated liquidus line (solid lines added to each isotherm, see Appendix B for details of analysis) appears consistent with nearly ideal mixing of each pair of components in the liquid phase.

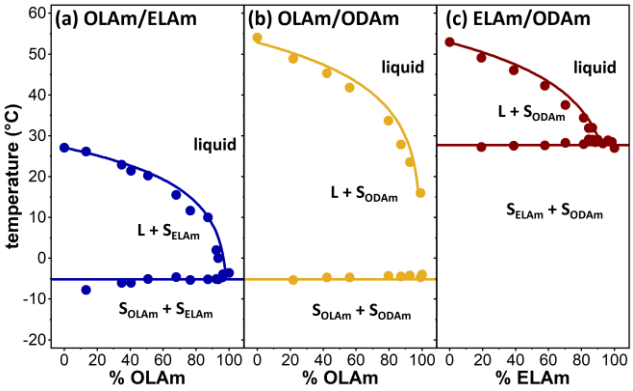

Figure 4.2. DSC phase diagrams for binary mixtures of (a) OLAm and ELAm, (b) OLAm and ODAm, and (c) ELAm and ODAm.

4.2.2 Alkyl composition influences phase transitions of ternary mixtures

To better understand the mixing behavior of alkyl chain morphologies and their impact on the phase behavior of technical-grade mixtures, we used DSC to assess the phase transitions of ternary mixtures of OLAm, ELAm, and ODAm. In previous work,[17, 98] we found that DSC thermograms of pure OLAm exhibit a single melting transition near -8 °C, which is 20–30 °C below the melting temperature of OLAm reported in the literature (typically 18–26 °C).Technical-grade OLAm exhibited a primary transition near -10 °C, with a broad, variable secondary transition near the literature T_m.

Here, we demonstrate the changing phase transition behavior of 3:1 OLAm/ELAm (a reasonable approximation of the typical technical-grade composition) as small amounts of ODAm (up to 10 %) are added to the mixture to approximate the typical range of abundance of this secondary impurity. Mixtures were generated targeting 0, 2.5, 5.0, 7.5, and 10 % ODAm, with actual percentages calculated by weighing samples after each sequential addition to the DSC pan. The 3:1 OLAm/ELAm binary mixture contains two phases (Figure 4.3, blue traces at top), one with T_m = -11 °C (similar to T_m(*cis*-OLAm)), and one with T_m near 10 °C, presumably a phase rich in ELAm (*trans* chains). The top blue trace in Figure 4.3 shows the complete thermogram for

3:1 OLAm/ELAm; the next blue trace shows the temperature range around the two endothermic transitions, with the vertical scale enlarged for the second peak to increase visibility of changes in peak shape with the addition of ODAm.

The addition of up to 4.4% ODAm (Figure 4.3, green and yellow traces) does not substantially impact the *trans*-rich peak, consistent with the miscibility of ELAm/ODAm up to a 87/13 ratio (which would represent 4.48% total ODAm in this blend). However, the addition of greater amounts of ODAm (7.5–10.6%, Figure 4.3, orange and dark red traces) produces a third endothemic transition in the range from 20–30 °C, consistent with separation of excess ODAm. The positions of these peaks shift to higher temperatures with increasing amounts of ODAm.

Finally, we compare these results to DSC thermograms (Figure 4.3, bottom two traces) of two technical-grade OLAm reagents – one described by the vendor as '70% OLAm' and one '95% amine'. The '70 % OLAm' blend (light blue trace) is most visibly similar to the 2.5 and 4.4% ODAm samples (green and yellow traces). Analysis by MS and NMR, summarized in Figure 4.4 indicates that the reagent is comprised of a 3.6:1 OLAm/ELAm blend, with ODAm equivalent to the 2.5% (green) trace, and a similar amount of hexadecylamine (HDAm, saturated 16-carbon amine). The reagent is also relatively rich in unsaturated impurities, which potentially also contribute to the double peak at 7.0 and 13.8 °C.

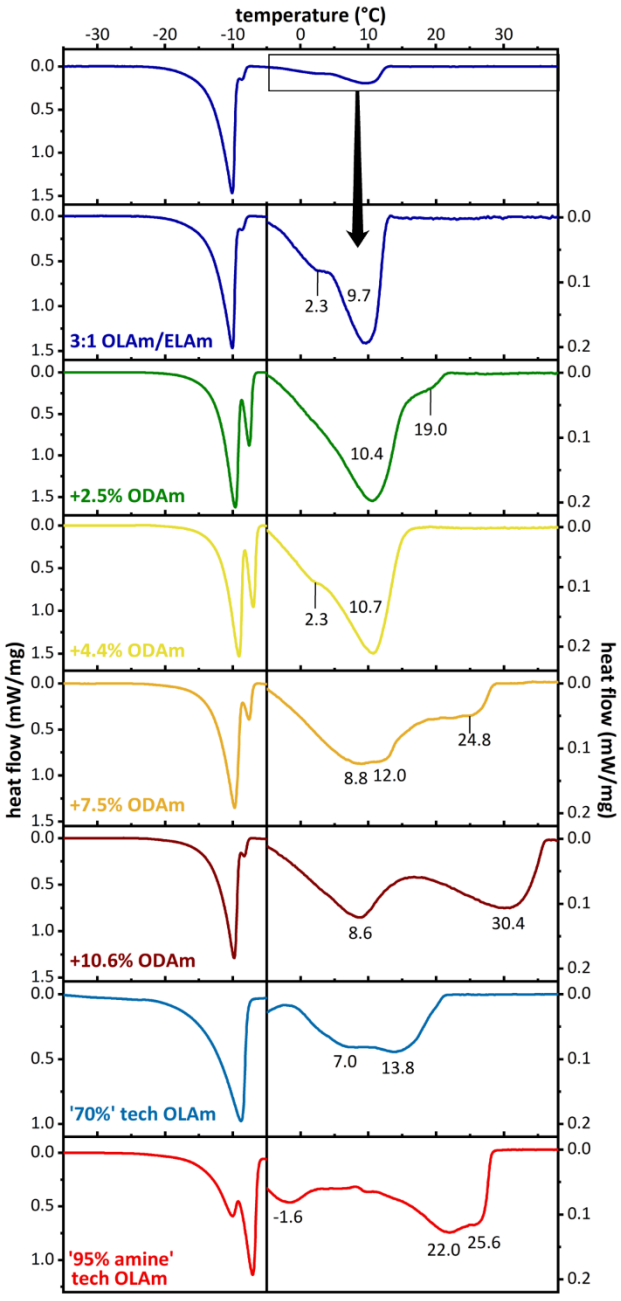

Figure 4.3. DSC thermograms for 3:1 OLAm:ELAm with 0-10% added ODAm, and for two technical-grade OLAm blends (bottom two traces).

In contrast, the ’95 % amine’ blend exhibits a prominent peak with a high-temperature edge at 25 °C (maximum heat flow 0.12 mW/mg), similar to the 7.5% ODAm sample (orange trace). MS/NMR analysis indicates this reagent contains 5.1% ODAm *vs.* 61.9% OLAm+ELAm,

equivalent to 7.5% ODAm *vs.* 90% OLAm+ELAm in the simplified mixture shown here). An additional peak is visible at 22 °C, consistent with the 3.7% HDAm in the blend.

		70% OLAm		95% amine	
		OLAm:ELAm: 3.6:1		*OLAm:ELAm: 2.5:1*	
Chain	**T_m**	*r.a.*	*total %*	*r.a.*	*total %*
18:1*z* (OLAm)	**-5 (*lit*)**	**78.3**	**57.5**	**72.2**	**40.1**
18:1*e* (ELAm)	**31 (*lit*)**	**21.7**	**15.9**	**27.8**	**15.8**
18:0 (ODAm)	**53 (*lit*)**	**3.3**	**2.4**	**9.9**	**5.6**
16:0 (HDAm)	**46 (*lit*)**	5.1	3.8	7.2	4.1
16:1		7.5	5.5		
18:2		15.5	2.1	5.2	2.9
18:3		4.6	3.4		

Figure 4.4. Percentages of ELAm, ODAm, and other key impurities in technical grade OLAm blends shown in Figure 4.3. NMR peak intensities were used to calculate OLAm:ELAm ratios. These values were then used to divide MS peak intensity at 268.3 m/z into OLAm and ELAm contributions. Relative abundances (r.a.), are calculated with OLAm + ELAm peak intensity taken to be r.a.=100, producing r.a. values for ODAm and other impurities that are comparable to the percentages of ODAm shown in Figure 4.3. Total % values are calculated based on the summed r.a. values for all major impurities.[17]

The agreement between the thermal phase behavior of the simplified ternary mixtures shown here and known complex technical grade OLAm reagents points to the possibility of ultimately identifying key blend physical characteristics relevant to nanocrystal synthesis with relatively simple metrics such as DSC thermogram peak positions.

4.2.3 Alkyl chain mixture composition influences AuNW growth.

To examine impacts of each ligand chain structure on nanocrystal synthesis, we conducted experiments in which binary mixtures of OLAm, ELAm, and ODAm were used in lieu of technical grade OLAm in the synthesis of ultranarrow AuNWs. The synthesis was carried out using a variation on a literature procedure,[49, 50, 81-83] in which $HAuCl_4 \bullet 3H_2O$, triisopropylsilane (TIPS), and OLAm were mixed in cyclohexane and aged to allow for AuNW growth. AuNWs produced using this procedure are 1.5–2 nm in diamter, and their OLAm ligand shells typically interact in solution, producing hexagonally-packed AuNW bundles based on depletion attraction.[83, 89, 90] Average AuNW length can be varied by controlling precursor concentrations (see Experimental Methods in Appendix B for more detail).

Here, we first carried out synthesis with pure *cis*-OLAm, using precursor concentrations (see Experimental Methods) that produced wires with lengths 61 ± 28 nm, based on transmission electron microscopy (TEM) images (Figure 4.5a). Center-to-center distances (d_{cc}) were also evaluated as a metric of ligand shell thickness, yielding d_{cc} = 4.8 nm for pure OLAm.

Next, we performed AuNW synthesis using blends of OLAm and (saturated) ODAm (Figure 4.5b,d) or (*trans*) ELAm (Figure 4.5c,e). Use of amine blends with at least 10% ODAm substantially shortened average wire length (mean near 20 nm and standard deviation ~10 nm for 5–30% ODAm) by nearly a factor of 3. This effect remained consistent across the ODAm percentages tested (up to 40%). Ligand shell thickness, as evaluted by d_{cc}, increased only slightly (from d_{cc} = 4.9 nm to 5.2 nm), suggesting the ligand shell morphology is comparable; that is, blending is not changing the interdigitated bilayer.

In contrast, addition of large amounts of ELAm (up to 80%) induced only minor variations in *average* AuNW length, but caused the clear evolution of two (or more) populations of wires, with averages of 30–40 nm for short wires, and 60–80 nm for longer wires. We refer to the shortest length as the 'base' population (Figure 4.5d,e, gold bars). For large percentages of ELAm (40 and 80 %), it appears that there may be a third population of wires, with lengths ~3x the base wire length.

Both ODAm and ELAm decrease the base AuNW length, potentially through more effective capping of the <111> facets on AuNW ends resulting from stronger chain-chain interactions. This could be reasonable, given the higher melting temperatures of both the *trans* and saturated chains. However, ELAm also produces populations of longer wires, with lengths that appear to be 2x and 3x the base AuNW length for the synthesis. Thus, we speculate that this effect may arise from end-to-end joining of wires as they bundle.[106] Again, given the stronger lateral packing interactions for *trans* and saturated chains, it may be reasonable that increased percentages of *trans* chains along the length of the wire increase bundling, potentially suggesting that ODAm may not be abundant either in the ligand shell, or in the outer layer of the interdigitated bilayer that would mediate initial interactions with adjacent nanowires during bundling.

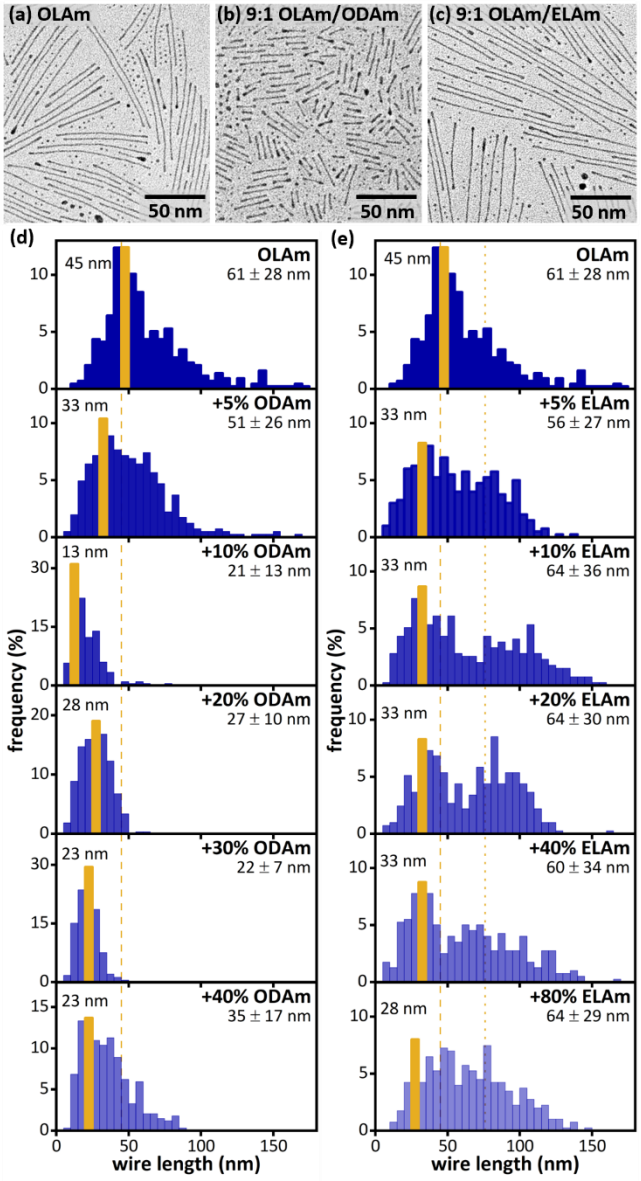

Figure 4.5. Impacts of ODAm and ELAm on AuNW synthesis. (a-c) TEM images of AuNWs synthesized with (a) 100% OLAm, (b) 90% OLAm/10% ODAm, (c) 90% OLAm/10% ELAm. (d,e) Histograms of AuNW lengths for syntheses carried out with pure *cis*-OLAm (top, both d and e), and with the addition of the stated percentage of (d) ODAm or (e) ELAm. Gold bars indicate base wire length for each condition.

4.2.4 Spectroscopic measurement of AuNW growth kinetics

To better understand the impacts of ligand structure on AuNW growth kinetics, we carried out UV-vis-NIR spectroscopy measurements on AuNW growth solutions with controlled ligand compositions (Figure 4.6). In these measurements we compared syntheses using pure *cis*-OLAm

(Figure 4.6a), or *cis*-OLAm blended with 10% ODAm (Figure 4.6b), 20% ELAm (Figure 4.6c), or 10% ODAm and 30% ELAm (Figure 4.6d). At the earliest timepoints (20–60 min, red traces), each reaction mixture exhibits minimal absorbance above 450 nm. At the 80 min timepoint, each reaction mixure exhibits increased absorption in the range up to ~600 nm, consistent with the reduction of Au(I) to Au(0) by TIPS. Notably, the increased absorption in this region over time is not accompanied by the appearance of an LSPR band at ~520 nm, but instead a shoulder emerges at ~490 nm suggesting that the AuNSs formed in the initial stages of reduction have diameters <2 nm.[107] Reaction mixtures with blended ligands (Figure 4.6b-d) also exhibit a peak near 1200 nm; in subsequent timepoints, this becomes a red-shifted tail with increased absorbance, characteristic of wire growth to lengths > 8 nm. For *cis*-OLAm, this evolution of NIR spectral features is observed starting at the 100 min timepoint, with the long tail for subsequent timepoints. The absorbance at 490 nm (A_{490}) increases more gradually with time for the reaction with pure cis-OLAm that for those with blended ligands (Figure 4.6e, A_{490} normalized to the 7 h timepoint), indicating faster formation of <2 nm diameter species in the presence of *trans* and saturated chains.

Thus, neither ODAm nor ELAm appears to shorten base AuNW length by slowing kinetics of the initial stages of growth, possibly consistent with a need for larger Au particles to generate more ordered ligand shells capable of expressing differentiated ligand populations at their ends.

Additionally, based on the similarity of the early stages of growth for blended ligands, we speculate that *trans* and saturated chains behave similarly in the initial stages of growth. Again, this may be consistent with longer wires forming during AuNW bundling, which would also become more favorable as the base wire length increases.

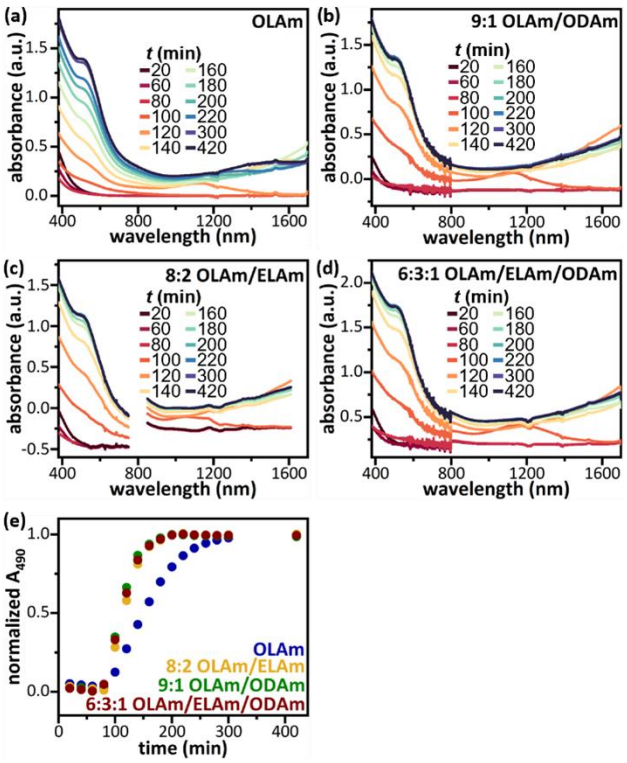

Figure 4.6. UV-vis-NIR kinetics measurements of AuNW growth with stated ligand blend: (a) pure *cis*-OLAm, or (b–d) *cis*-OLAm with (b) 10 % ODAm, (c) 20 % ELAm, or (d) 10 % ODAm and 30 % ELAm. During spectrum acquisition, switching between UV/vis and NIR sources occurs at 800 nm, creating a change in the spectral data at that point. (e) Normalized absorbance at 490 nm for each reaction mixture *vs*. time.

4.2.5 Composition of AuNW ligand shell vs. alkyl chain composition used in synthesis

Next, we sought to understand whether disproportionate inclusion of ELAm and ODAm in AuNW ligands shells relative to the ligand composition used for synthesis could contribute to differences in AuNW growth. For these experiments we used a cyanide etching process to dissolve the Au cores of washed AuNWs to liberate surface bound ligands for characterization. Details of the cyanide etching process are outlined in the Experimental Methods section and Appendix B. Analysis of the allylic and vinylic proton signals in ^{1}H NMR spectra yielded *cis:trans* ratios for ligand shells containing both OLAm and ELAm. The observed *cis:trans* ratios (Figure 4.7a,b) are consistent with the relative amounts of OLAm and ELAm used in AuNW synthesis.

The proportion of ODAm in the ligand shells could not be determined using ^{1}H NMR, so we instead used MS (Figure 4.7c) to analyze the relative amounts of OLAm and ODAm in the ligand shell. Here, we compared ligands recovered from AuNWs synthesized using 6:3:1

OLAm/ELAm/ODAm with those recovered from AuNWs synthesized using 9:1 OLAm/ODAm. We hypothesized that the inclusion of ELAm in ligand shells might increase abundance of ODAm in comparison with an OLAm/ODAm binary mixture, due to greater miscibility. However, MS data do not appear consistent with this hypothesis. In each case, ODAm is slightly enriched in the ligand shell relative to the original mixture (r.a. of ODAm based on stoichiometry should be 11.1), but its abundance in the OLAm/ELAm/ODAm ligand shell (13.3) is slightly lower than in the OLAm/ODAm ligand shell (17.5).

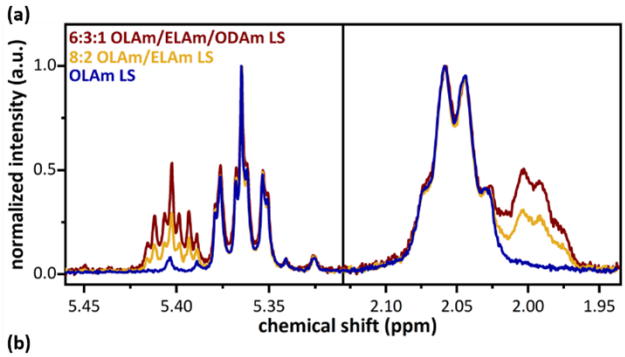

(b)

ligand blend	vinyl protons		allyl protons	
	% *cis*	% *trans*	% *cis*	% *trans*
8:2 OLAm/ELAm	77.9	22.1	79.6	20.4
6:3:1 OLAm/ELAm/ODAm	67.7	32.3	68.6	31.4

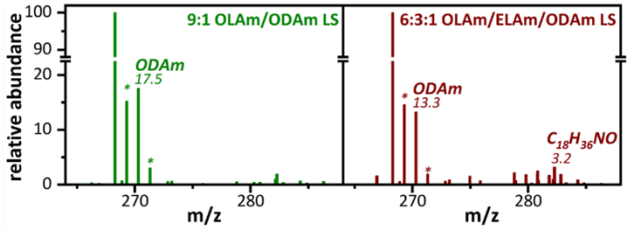

Figure 4.7. (a) Overlay of vinyl (left) and allyl (right) regions of ^{1}H NMR spectra for ligand shells of AuNWs synthesized using OLAm (blue), 8:2 OLAm/ELAm (yellow), and 6:3:1 OLAm/ELAm/ODAm (red) ligand blends. (b) Table reporting percent compositions of *cis* and *trans* chains calculated based on vinyl (left) and allyl (right) ^{1}H NMR signals. (c) Mass spectra of ligand shells from AuNWs grown using 9:1 OLAm/ODAm (green) and 6:3:1 OLAm/ELAm/ODAm (red).

4.2.6 Ligand blend influences AuNW adsorption at chemically patterned interfaces

To examine how AuNW ligand shell composition impacts further assembly processes, we allowed batches of AuNWs synthesized with controlled binary and ternary blends to adsorb to

chemically templated interfaces. The interfaces we utilized are composed of striped phases of diyne phosphoethanolamine (dPE),[7] in which the alkyl chains in the amphiphile lie parallel to a highly oriented pyrolytic graphite (HOPG) substrate (Figure 4.8a, top left). This type of molecular assembly occurs readily on HOPG,[10, 84-86] and other 2D materials, generating a pattern comprised of 1-nm-wide stripes of functional groups with a pitch of ~7 nm, tunable based on alkyl chain length.

Previously, we have demonstrated that when these dPE striped surfaces on HOPG (dPE/HOPG) are held under controlled hydration conditions (Figure 4.8a, top center right), then immersed in AuNW solution, excess OLAm forms hemicylindrical micelles around the hydrated headgroups (Figure 4.8a, top right), and the surface undergoes a complex set of interactions with AuNWs that cause them to orient with the striped template, straighten, and separate (Figure 4.8a, bottom);[11] these assembly interactions exhibit further temperature-regulated changes.[17]

Here, we exposed dPE/HOPG templates to AuNW growth solutions generated with controlled blends of OLAm, ELAm, and ODAm (Figure 4.8b–m). In general agreement with our expectations, we observed differences in assembly based on ligand shell composition.

However, what we also observed was that, in each case, the lengths of adsorbed wires measured by AFM (Figure 4.8b,e,h,k) were substantially greater than lengths observed by TEM (Figure 4.8c,f,i,l, shown at same scale as AFM images). Histograms of wire lengths (Figure 4.8d,g,j,m) tabulated from TEM images (gold bars) and AFM images (blue bars) illustrate that in each AuNW solution tested, the mean wire length measured by AFM is ~2x the mean measured by TEM.

Although it would be reasonable for surface binding affinity to increase with AuNW length, potentially skewing the surface measurement toward longer wires, this trend is evident even in the OLAm/ODAm sample (Figure 4.8e–g), in which wires are uniformly short (21 ± 13 nm, as measured by TEM), while wires measured by AFM are predominantly 50–100 nm in length. The systematic difference may indicate that individual cylindrical micelles in each nanowire bundle frequently contain 2–4 short AuNWs, and that AFM measures the full micelle length, providing further possible insights into AuNW growth and assembly. For instance, the observation that micelles adsorbing from OLAm/ODAm growth solution exhibit the *greatest* difference in length, when compared with TEM, could be consistent with the hypothesis that ODAm binding to

AuNW ends limits AuNW length both by slowing wire growth through gold deposition at the wire termini, and by limiting fusion between AuNW ends within bundles.

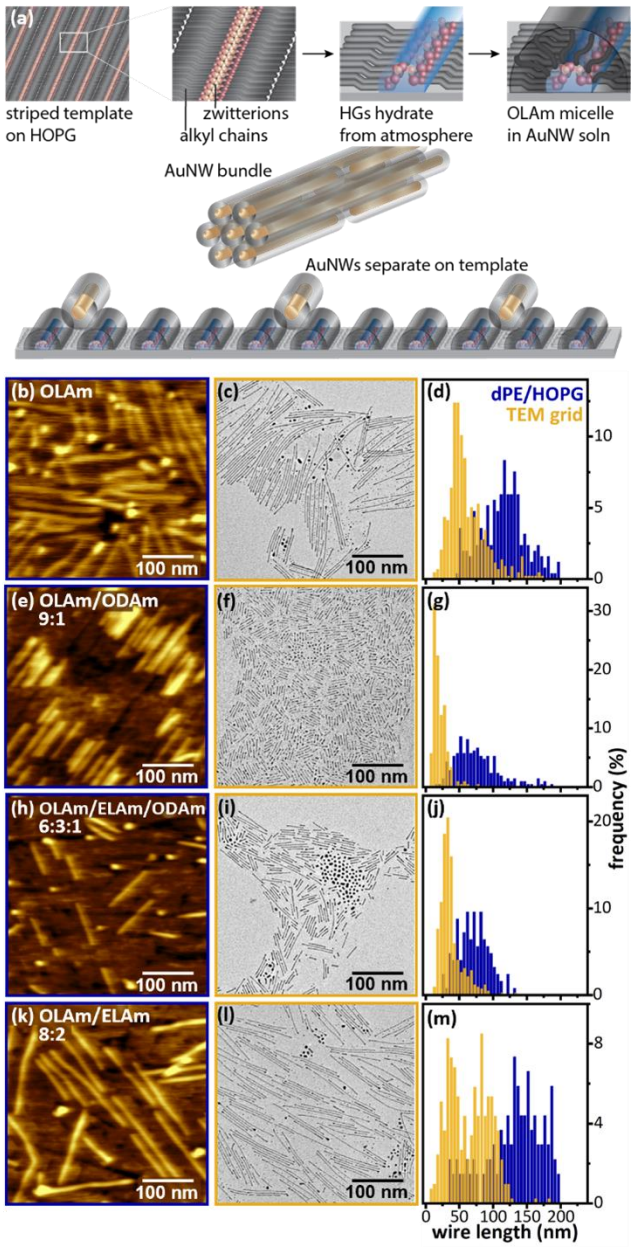

Figure 4.8. (a) Schematic of AuNW adsorption on striped molecular templates on HOPG. (b,e,h,k) AFM images of AuNWs adsorbed to dPE/HOPG striped templated substrates. (c,f,i,l) TEM images of washed AuNWs deposited on TEM grids. All AFM and TEM images depict a representative 400 nm x 400 nm region, to facilitate visual comparison of populations. (d,g,j,m) Histograms of AuNW lengths measured by TEM (gold bars) and AFM (blue bars).

Interestingly, the ternary ligand blend (6:3:1 OLAm/ELAm/ODAm, Figure 4.8h–j) exhibits wire lengths much more similar to the 9:1 OLAm/ODAm blend (Figure 4.8e–g) than to the 8:2 OLAm/ELAm blend (Figure 4.8k–m). Again, this would be consistent with the hypothesis that ODAm binds to AuNW ends more strongly than ELAm, preventing joining of wire ends within bundles. Although the lengths of adsorbed wires are very similar for OLAm/ODAm (Figure 4.8e) and OLAm/ELAm/ODAm (Figure 4.8h), the adsorption itself is very different for the two samples – ribbon phases are observed for OLAm/ODAm, while limited adsorption of individual wires is observed for OLAm/ELAm/ODAm. This would be in line with our previous findings that suggest ligand shell phase transitions drive differences in adsorption on these surfaces, with the adsorption patterns observed in Figure 4.8h consistent with solid-like ligand shells on AuNW bundle interiors limiting bundle adsorption. Less-ordered ligand shells in the OLAm/ODAm blend (Figure 4.8e) would allow for bundle adsorption and spreading to form ribbons.

4.2.7 Ligand blend composition also impacts AuNW stability, with increased stability conferred by *trans* and saturated chains

After adsorption to dPE/HOPG substrates, AuNWs slowly begin to undergo conversion from wires to small spherical nanoparticles due to Rayleigh instability, as shown in AFM topography images (Figure 4.9). The timescale of conversion depends on the composition of the ligand blend in the growth solution. We observed primarily AuNWs with a small fraction of AuNPs 20 min after adsorption of OLAm AuNWs to the surface (Figure 4.9a). The relative fraction of AuNWs on the surface decreased after 40 min (Figure 4.9b), while the relative surface coverage of AuNPs increased. After 1 h (Figure 4.9c), only AuNPs were observed on the surface. In comparison, AuNWs synthesized using 9:1 OLAm/ODAm do not undergo Rayleigh instability after 20 minutes (Figure 4.9d), and we observed a mixture of AuNWs and AuNPs 3 h and 7 h after adsorption to the dPE/HOPG substrate (Figure 4.9e,f), suggesting that ODAm stabilizes the surface adsorbed AuNWs. We observed a similar increase in stability for surface adsorbed AuNWs synthesized using 8:2 OLAm/ODAm (see Appendix B), possibly suggesting that increased ligand ordering due to the inclusion of *trans* and saturated chains results in greater stability.

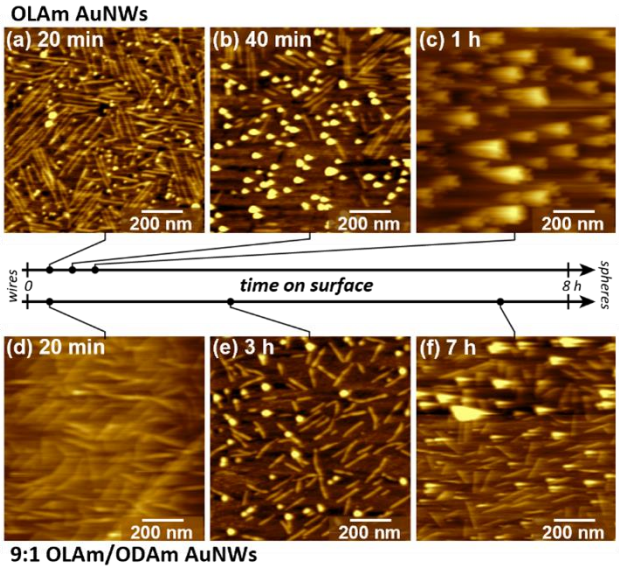

Figure 4.9. AFM topography images of AuNW synthesized using OLAm (a,b,c) and 9:1 OLAm/ODAm (d,e,f) collected at various time points after adsorption to dPE/HOPG substrates.

4.3 Conclusions

Nanocrystals are often synthesized from technical-grade OLAm reagents that contain complex mixtures of alkyl amines, raising the possibility that these differences in chain structure composition impact nanocrystal growth and assembly. Here, we have shown that OLAm, and its common *trans* and saturated alkyl impurities ELAm and ODAm, exhibit limited miscibility when the molecules are blended, as in technical-grade OLAm reagents. Additionally, we have illustrated that OLAm and ELAm exhibit distinct impacts on nanocrystal growth, in the context of ultranarrow AuNW synthesis: both ligands decrease base wire lenth, consistent with selective binding of nanowire <111> end facets. However, ODAm also appears to prevent formation of long wires, while ELAm promotes formation of long wires. We rationalize this observation, suggesting that ELAm (and perhaps also ODAm) may promote AuNW bundling, leading to co-localized wire ends that can join (in the presence of ELAm) or remain separated (if capped with stronger-binding ODAm). When both ODAm and ELAm ligands are added simultaneously, the ODAm growth pattern is observed, consistent with this suggestion. AuNWs adsorbed to interfaces and imaged by AFM also exhibit lengths 2-4 times those of average wires lengths imaged by TEM, consistent with the possibility of end-to-end joining in bundles that is regulated by end-capping.

4.4 Experimental methods

4.4.1 Materials

Ammonium hydroxide solution (28.0-30.0% NH_3 basis), oleylamine (OLAm, technical grade, 70%, lot #STBJ0354), triisopropylsilane (TIPS, 98%), oleic acid (OLAc, ≥99%), lithium aluminum hydride (95%), octadecylamine (ODAm, ≥99%), oxalyl chloride (98%), manganese (II) chloride tetrahydrate (≥99%), chloroform, anhydrous diethyl ether, and molecular sieves (4 Å) were purchased from Sigma Aldrich (Saint Louis, MO) and used as received. Diethyl ether, dichloromethane (DCM), dimethylformamide (DMF), methanol (MeOH), sodium sulfate, and sodium chloride were purchased from Fisher Scientific (Fair Lawn, NJ) and used as received. Dry cyclohexane (99.5% extra dry, Acroseal), elaidic acid (98%), and tetrachloroauric acid trihydrate (ACS reagent grade) were purchased from Acros Organics (Fair Lawn, NJ) and used as received. Oleylamine (min 95%, lot #23662300) was purchased from Strem Chemicals (Newburyport, MA) and used as received. Sodium cyanide (98%) was purchased from Alfa Aesar (Haverhill, MA) and used as received. 1,2-bis(10,12-tricosadiynoyl)-sn-glycero-3-phosphoethanolamine (dPE, >99% purity) was purchased from Avanti Polar Lipids (Alabaster, AL).

4.4.2 AFM imaging

AFM images were collected in tapping mode using an Agilent (Agilent Technologies, Santa Clara, CA) 5500 AFM equipped with a MikroMasch (MikroMasch, Tallinn, Estonia) HQ:NSC18/No-Al AFM probe (nominal force constant 2.8 N/m, radius <8 nm).

4.4.3 DSC

DSC thermograms were acquired using a Perkin Elmer (Perkin Elmer, Waltham, MA) Jade DSC. A temperature scan rate of 2 °C/min was used for all scans unless otherwise noted. Perkin Elmer volatile aluminum DSC pans were used to contain the samples. An empty DSC pan was packed with aluminum to be used as the reference; aluminum was added so that the mass of the reference pan was 100–110% of the mass of the sample pan. To facilitate comparison between thermograms, samples were normalized based on weight and baseline correction was performed using the Peak Analyzer wizard in Origin Pro.

4.4.4 Synthesis of OLAm and ELAm

OLAm and ELAm were synthesized from OLAc and ELAc respectively using a procedure modified from the literature,[108] described briefly here. A more detailed description can be found in the Supporting Information. Fatty acyl chlorides were prepared *via* chlorination of fatty acids by oxalyl chloride. The acyl chlorides were subsequently amidated by dropwise addition to an aqueous solution of ammonia. The resulting fatty amide was reduced by lithium aluminum hydride to yield the primary amine product.

4.4.5 NMR

^{1}H NMR spectra were collected using a Bruker AV-III-400-HD (400 MHz) spectrometer equipped with a 5 mm BBFO Z-gradient SmartProbe (Bruker Corporation, Billerica, MA). Samples were prepared in $CDCl_3$ or CD_3OD (Cambridge Isotope Laboratories, Tewksbury, MA).

4.4.6 AuNW growth

AuNW synthesis was carried out using procedures adapted from the literature.[49, 50, 81, 82] The reaction flask was charged with molecular sieves, 2.5 mg of $HAuCl_4 \cdot 3H_2O$, and 8.0 mL of dry cyclohexane. Capping ligands (OLAm, ELAm, ODAm) were combined in the reported ratios to reach a final quantity of 255 µmol. The capping ligand blend was added to the reaction mixture followed by brief agitation using a vortex mixer. Triisopropylsilane (120 µL) was added and the solution was mixed using a vortex mixer until the $HAuCl_4 \cdot 3H_2O$ was dissolved. The reaction mixture was moved to a humidity-controlled chamber to age 12 h at ambient temperature.

4.4.7 Extraction of nanocrystals from AuNW growth solution

AuNWs were harvested by centrifugation at 6000 rpm for 5 min in a 1:3 cyclohexane/ethanol solvent mixture. The supernatant was removed, and the pellet was resuspended in cyclohexane.

4.4.8 TEM imaging

TEM images were collected using a Tecnai G2 20 (Thermo Fisher Scientific, Hillsboro, OR) instrument with a lanthanum hexaboride filament and an accelerating voltage of 200 kV. A 200 mesh Cu grid with pure C coating (Ted Pella, Redding, CA) was charged with 6 µL of resuspended AuNW solution. After 10 s, the solution was wicked from the grid.

4.4.9 Etching of AuNW cores to obtain free ligand shell

To collect AuNWs and remove unbound ligands, the AuNWs were extracted and washed by repeating the precipitation and centrifugation procedure listed above three times. AuNWs were then resuspended in 5 mL of DCM under stirring and 5 mL of 1 M aqueous NaCN was added. The reaction mixture was stirred for 5 h under ambient conditions. The organic layer was collected, washed 3 times with milli-Q water, then dried over sodium sulfate. Solvent was removed to yield the liberated ligand molecules.

4.4.10 UV-Vis-NIR

Absorption spectra were acquired using an Agilent Cary 6000i UV-Vis-NIR spectrophotometer (Agilent, Santa Clara, CA) with a scan rate of 500 nm/min. Growth solutions were prepared normally, then immediately transferred to 10 mm quartz cuvettes. Spectra were collected every 20 minutes for the first 12 hrs of wire growth.

APPENDIX A. SUPPORTING INFORMATION FOR CHAPTER 3

Oleylamine Impurities Regulate Temperature-Dependent Hierarchical Assembly of Ultranarrow Gold Nanowires on Biotemplated Interfaces

Materials and Methods.

Materials.

Ammonium hydroxide solution (28.0-30.0% NH_3 basis), oleylamine (OLAm, technical grade, 70%), triisopropylsilane (TIPS, 98%), oleic acid (OLAc, ≥99%), lithium aluminum hydride (95%), octadecylamine (ODAm, ≥99%), oxalyl chloride (98%), manganese (II) chloride tetrahydrate (≥99%), chloroform, anhydrous diethyl ether, and molecular sieves (4 Å) were purchased from Sigma Aldrich (Saint Louis, MO) and used as received. Oleylamine (min 95%) was purchased from Strem Chemicals (Newburyport, MA) and used as received. Diethyl ether, dichloromethane (DCM), dimethylformamide (DMF), sodium sulfate, and sodium chloride were purchased from Fisher Scientific (Fair Lawn, NJ) and used as received. Dry cyclohexane (99.5% extra dry, Acroseal), and tetrachloroauric acid trihydrate (ACS reagent grade) were purchased from Acros Organics (Fair Lawn, NJ) and used as received. Sodium cyanide (98%) was purchased from Alfa Aesar (Haverhill, MA) and used as received. 1,2-bis(10,12-tricosadiynoyl)-*sn*-glycero-3-phosphoethanolamine (dPE, >99% purity) was purchased from Avanti Polar Lipids (Alabaster, AL).

NMR analysis to determine cis:trans ratio of OLAm reagents.

A procedure based on the ratio method for separating spectral features of mixtures was adapted from the literature.[16] Here, the ratio method is based on the assumption that for OLAm reagents, the ^{1}H NMR spectral features for vinyl and allyl protons are linear sums of weighted spectra of *cis* and *trans* isomers: $reagent(\delta) = A * cis(\delta) + B * trans(\delta)$ where δ is a chemical shift, and A and B are the amplitude weights of each isomer.

For each reagent, a spectral feature belonging to the *cis* component was normalized to the intensity of the same spectral feature from the synthesized *cis*-OLAm. The spectrum of the *trans* component was obtained through the difference of the normalized spectra. The amplitude weights of each component (*cis* and *trans*) were determined using the Composite Spectrum Regression tool

in OriginPro 2021 (OriginLab Corporation, Northampton, MA). The relative areas under the peaks were also calculated using OriginPro 2021. The reported *cis:trans* ratios for each reagent are averaged across vinylic and allylic protons.

Procedure for thermally controlled rotary LS conversion of dPE monolayers.

For assembly experiments using longer AuNWs (~450 nm), dPE monolayers exhibiting very long-range order were prepared using thermally controlled rotary Langmuir-Schaefer (TCR-LS) conversion, which routinely transfers molecular domains with areas >100 μm^2, as we have previously reported.[12] The TCR-LS conversion of dPE monolayers to produce striped phase templates on flexible HOPG films was carried out using single barrier compression on a Kibron trough. The subphase (5 mM $MnCl_2$ in water) was heated to 30 °C and 60 µL of a 0.5 mg/mL solution of dPE in $CHCl_3$ was deposited on the surface. An equilibration period of 30 min was allotted to allow for evaporation of the spreading solvent. Following equilibration, a single trough barrier was swept inward at 6 mm/min to compress the monolayer to the desired 30 mN/m surface pressure. A thermally controlled copper disk was cleaned with hexane and ethanol, and a pliant HOPG film was mounted to the disk. The copper disk and mounted HOPG film were heated to 80 °C; this temperature was maintained throughout the LS conversion. The HOPG film was lowered into contact with the Langmuir film, and the copper disk was rotated such that the HOPG translation rate across the Langmuir film was 0.14 mm/s. Following TCR-LS conversion, the HOPG film was removed from the copper disk, gently dried with N_2, and placed under UV radiation (254 nm) for 1 h to photopolymerize the dPE monolayer.

AuNW growth.

AuNW synthesis was carried out using procedures adapted from the literature.[11, 81-83, 89] Typically, the reaction flask was charged with molecular sieves, 2.5 mg of $HAuCl_4 \cdot 3H_2O$, and 5.8 mL of dry cyclohexane. Oleylamine (84 µL) was added, followed by brief agitation of the solution using a vortex mixer. Triisopropylsilane (120 µL) was added and the solution was mixed until the $HAuCl_4 \cdot 3H_2O$ was dissolved. The reaction mixture was moved to a humidity-controlled chamber to age 12 h at ambient temperature. For experiments using longer AuNWs (~450 nm and >1 µm), the same procedure was carried out using 2.4 mL and 1.8 mL of cyclohexane, respectively.

Procedure for synthesis of oleylamine from oleic acid.

Oleic acid (2.25 mL, 7 mmol) was dissolved in 25 mL of dichloromethane (DCM) at room temperature under N_2. Three drops of N,N-dimethylformamide (DMF) were added to the mixture, followed by oxalyl chloride (0.78 mL, 9.2 mmol). The reaction was stirred overnight at room temperature under an atmosphere of N_2. Solvent and excess oxalyl chloride were removed *via* rotary evaporation to yield oleoyl chloride as a yellow/orange oil.

Ammonium hydroxide solution (100 mL) was charged to a round bottom flask and cooled to 0 °C. A solution of oleoyl chloride (1.25 g) in 5 mL tetrahydrofuran (THF) was added dropwise under vigorous stirring, forming a white precipitate. The mixture was brought to room temperature and stirred for 18 h. The product was extracted with DCM (3×100 mL). The DCM layers were then combined and washed with water. If the addition of water resulted in a cloudy single-phase mixture, the addition of a small aliquot of brine solution typically allowed the mixture to form immiscible layers. The organic layer was collected and dried over sodium sulfate. Solvent was removed to yield oleylamide as a white solid.

A slurry of oleylamide (1.09 g, 3.9 mmol) and 40 mL of anhydrous diethyl ether under N_2 was brought to 0 °C. Under vigorous stirring, lithium aluminum hydride (1.47 g, 39 mmol) was added. The mixture was brought to room temperature and stirred for 20 h. The reaction was quenched at 0 °C by sequential addition of 1.5 mL water, 1.5 mL of 15 % NaOH in water, and 4.5 mL water. The mixture was filtered, and the organic layer was collected and dried over sodium sulfate. Solvent was removed to yield OLAm as a transparent, pale yellow oil (~80% yield).

Extraction of nanostructures from AuNW growth solution.

AuNWs were harvested by centrifugation at 8000 rpm for 10 min in a 1:2 cyclohexane/ethanol solvent mixture. This procedure was repeated three times in order remove excess OLAm and silane.

Au core etching.

Following washing and extraction from the AuNW growth solution, AuNWs were resuspended in 5 mL of DCM under stirring. To the solution of resuspended AuNWs, 5 mL of 1 M aqueous NaCN was added. The reaction mixture was stirred for 5 h under ambient conditions.

The organic layer was collected, washed 3 times with milli-Q water, then dried over sodium sulfate. Solvent was removed to yield the liberated ligand molecules.

Energy minimization.

Models of lamellar structures were visualized and minimized using the software packages Maestro[109] and Macromodel[110] (Schrödinger, Cambridge MA), respectively. Models of lamellar structures were minimized using the OPLS3e force field with extended cutoffs. The Polak-Ribiere conjugate gradient (PRCG) algorithm and gradient method with 50000 iterations and a convergence threshold of 0.05 was used to perform minimizations.

Models of OLAm hemicylindrical reverse micelles at the dPE/HOPG surface were visualized by sequential minimization of dPE on HOPG, followed by the dPE monolayer with 97 water molecules, and finally the dPE monolayer with water molecules and 105 OLAm molecules. The minimizations were performed using the same parameters as the lamellar structures, but additionally used an octanol solvent environment.

AFM images comparing AuNW assembly on bare HOPG and dPE/HOPG.

AFM images of freshly cleaved HOPG substrates exposed to growth solutions of long (Figure A.1a) and short (Figure A.1b) AuNWs illustrate typical adsorption behavior for each condition. Long AuNWs adsorb to the HOPG surface as flexible bundles (Figure A.1a), without evident alignment with the substrate lattice. Short AuNWs can adsorb individually or as bundles, which are aligned epitaxially with the underlying graphite lattice. The AFM images show that, upon exposure of bare HOPG to AuNW growth solution, excess OLAm from the AuNW solution can adsorb in a lying down configuration (Figure A.1b inset), generating a lamellar pattern morphologically similar to the dPE template, but with different polar headgroup chemistry.

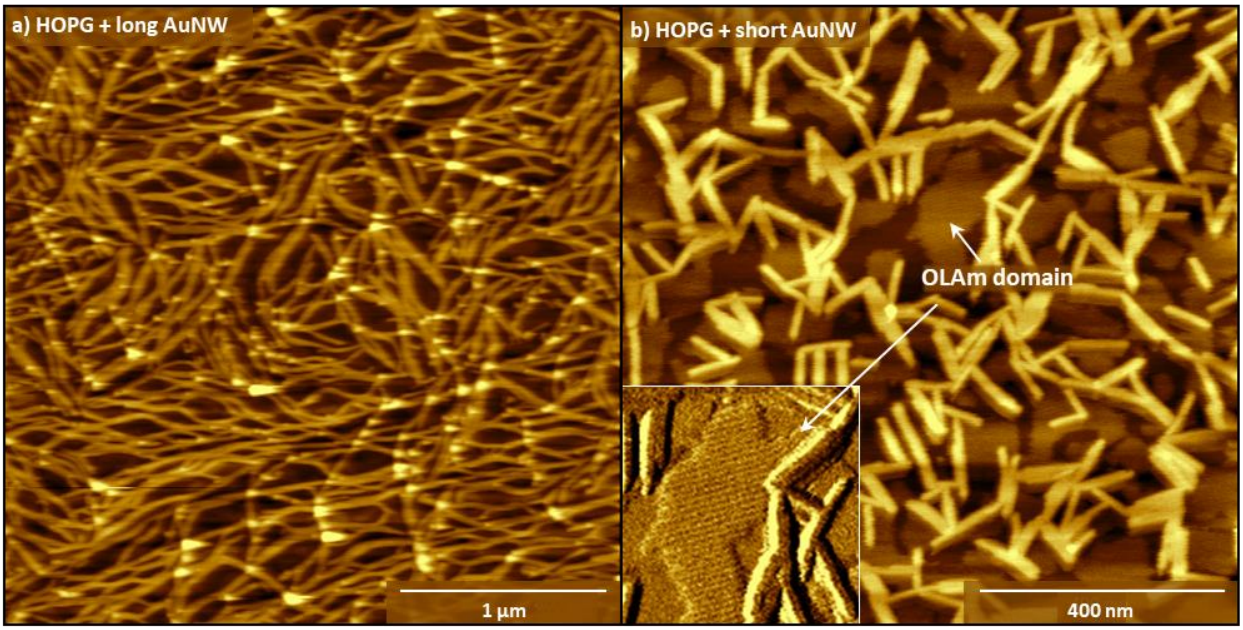

Figure A.1. AuNW assembly on bare HOPG substrates. AFM topography images of (a) long and (b) short AuNWs assembled on freshly cleaved HOPG substrates. The inset in (b) is an AFM phase image showing the lying down structure of OLAm domains.

Distinct adsorption morphology of AuNWs is observed when a dPE monolayer is present on the HOPG surface (Figure A.2). AuNW adsorption is templated by the striped surface chemistry of the dPE. Previously, we have reported that striped phases of dPE induce ordering of AuNWs through a multi-step assembly process,[11] summarized briefly here. dPE headgroups in the template monolayer adsorb water from the ambient environment, forming water nanochannels ~1 nm in diameter, around which hemicylindrical inverse micelles of excess OLAm assemble upon exposure to AuNW solution. This assembly process generates arrays of protected ~1-nm-wide channels in which dPE headgroup dipoles can collectively reorient. Molecular dynamics suggest that on average, headgroups orient with a substantial dipole component normal to the surface. Thus, when dipole arrays on the dPE/HOPG surface interact with polarizable AuNWs, the nanowires initially undergo transverse polarization, simultaneously inducing an attractive AuNW/substrate interaction and a repulsive interaction between adjacent AuNWs. These interactions lead to straightening and separation of the AuNWs. Assembly takes place in a low dielectric solvent (cyclohexane, ε ~2); in this environment, the distance through which two elementary charges can interact with a magnitude equal to kT (Bjerrum length) is ~28 nm, making wire/interface and wire/wire electrostatic interactions possible over substantial distances. AFM images show typical

adsorption behavior for AuNWs on dPE/HOPG. Long AuNWs become well separated when the wire long axes align with the template stripe direction but remain in bundles when not aligned with the template (Figure A.2a). This is clearly depicted in the higher resolution AFM phase image (Figure A.2b), in which the dPE template stripes are visible. When AuNWs with lengths much shorter than average dPE domain length adsorb, the wire long axes align with the template stripe direction. Ribbon phase assembly (Figure A.2c) is observed from AuNW solutions at temperatures below T_R, while nematic assembly (Figure A.2d) is observed at temperatures above T_R. Related behavior is observed for AuNWs with lengths somewhat greater than dPE domain lengths, although more adsorption defects are observed, due to inability of AuNWs to align with just one dPE template domain direction.

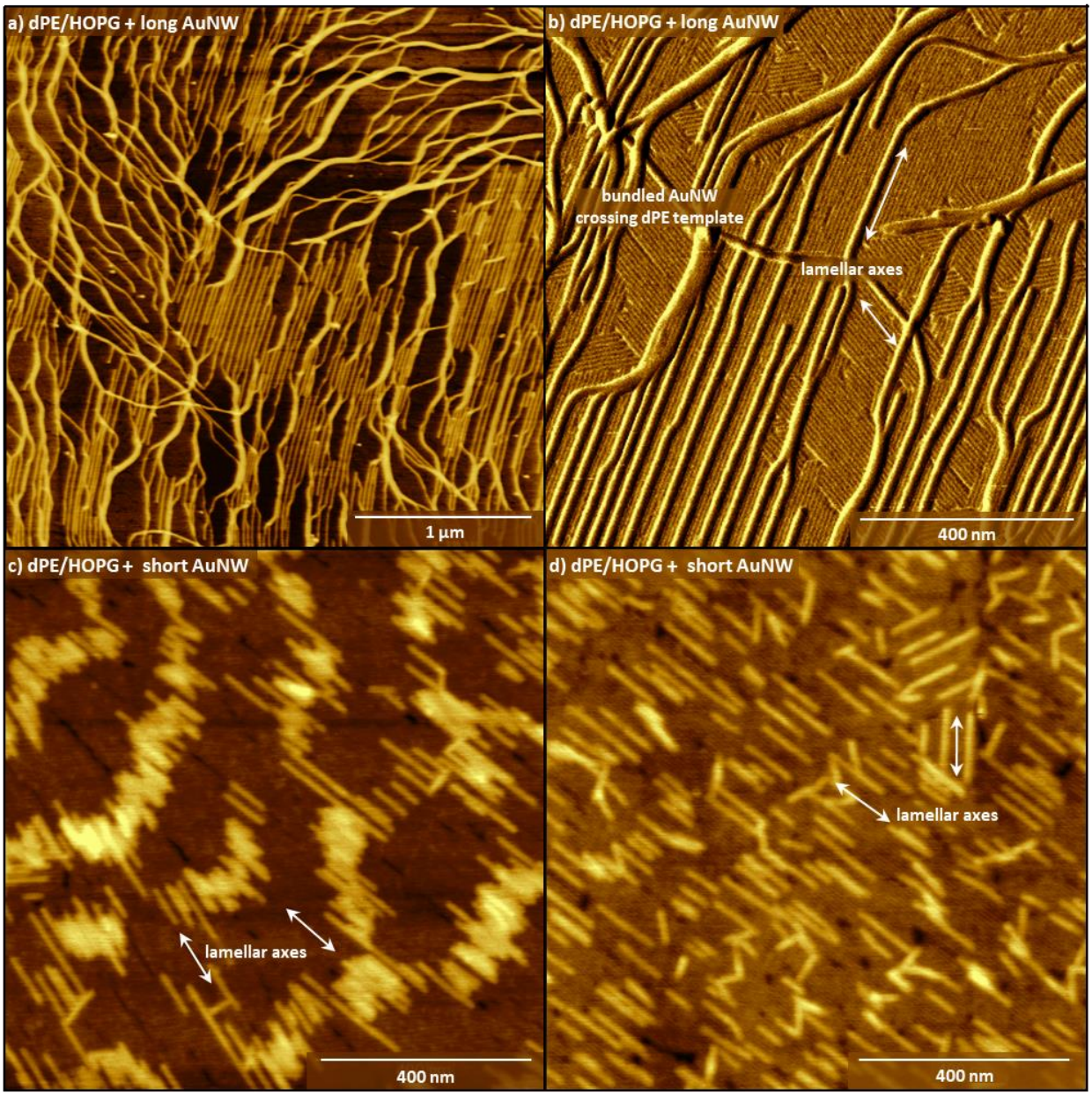

Figure A.2. AuNW assembly on templated substrates. AFM images of: (a) long AuNWs assembled on dPE template, (b) high resolution phase image showing AuNW alignment with dPE lamellar axes, (c) ribbon phase assembly of AuNWs on dPE template, (d) nematic assembly of AuNWs on dPE template.

Effects of adsorption time and concentration on AuNW adsorption morphology.

The adsorption morphology of AuNWs on dPE/HOPG is influenced by both the concentration of the AuNW solution that the substrate is exposed to and the length of time the substrate is exposed to the solution. Ribbon phases of AuNWs are typically only observed when

the substrate is exposed to sufficiently concentrated solutions of AuNWs, as illustrated by the top row of AFM images in Figure A.3a. Occasionally, ribbon assemblies have been observed as a minority phase adsorbed from solutions with as low as 12 nM [AuNW]. Typical adsorption behaviors for a range of solution concentrations at various time points are illustrated by the AFM images in other rows of Figure A.3a. The AuNWs used here are ~100 nm (Figure A.3b) long and have been diluted with dry cyclohexane to the concentration of AuNWs indicated in the left panel of the figure. Here, AuNW concentration is approximated based on the assumption that all Au atoms in the reaction solution were incorporated into 100 nm long AuNWs with diameters of 2 nm. AFM images (Figure A.3a) indicate that fewer AuNWs are adsorbed from dilute solutions of AuNWs, consistent with classical models of adsorption (*e.g.*, Langmuir, Freundlich). Despite differences in adsorption morphology, for all concentrations of AuNWs studied, the fraction of dPE/HOPG surface covered by AuNWs increased with exposure time (Figure A.3c). Ribbon phases assemble rapidly (AuNW solution exposure as little as 1 s, Figure A.3c), making it difficult to elucidate the early stages of the assembly process. However, AFM images depicting ribbon phases at very short time points suggest that ribbon phases become more defined over time (Figure A.3d).

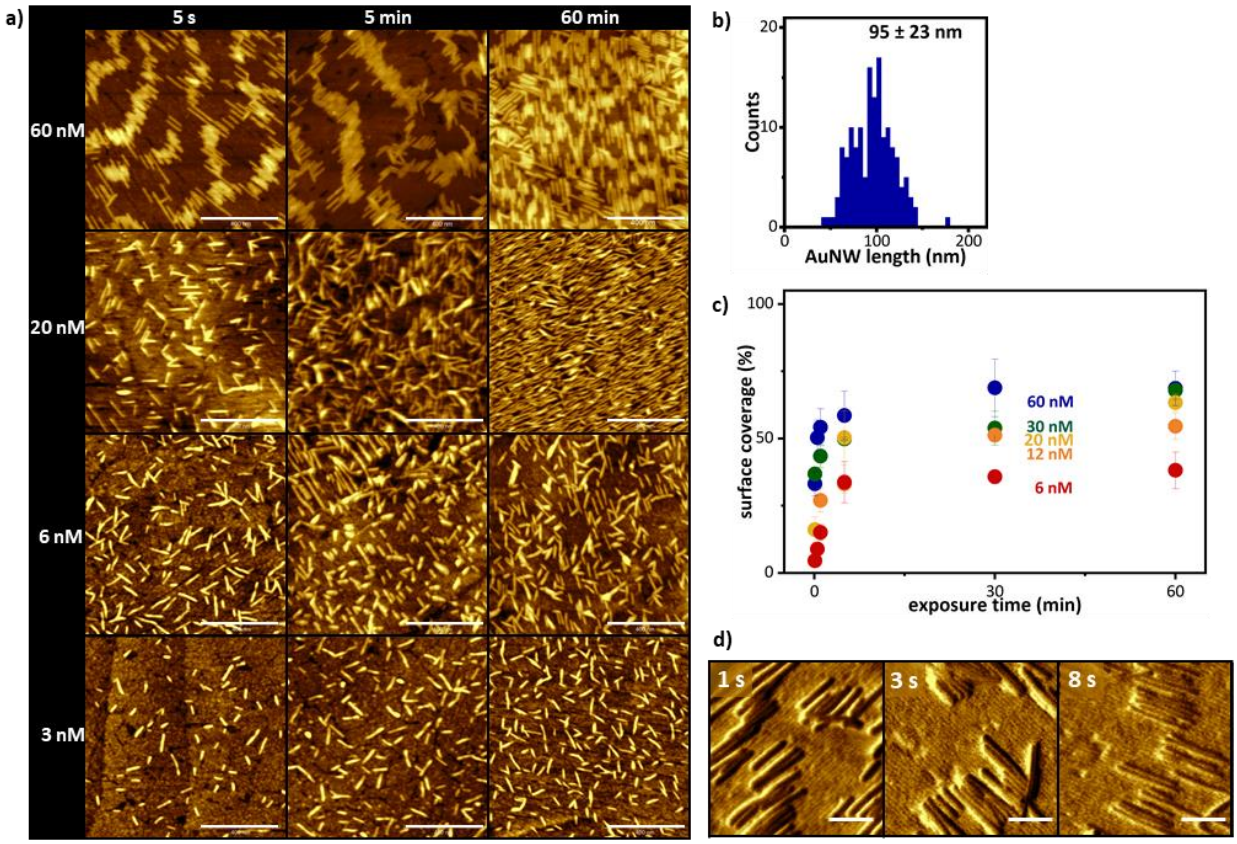

Figure A.3. Surface coverage of dPE/HOPG substrates as a function of AuNW concentration and time of exposure. (a) AFM images of AuNWs adsorbed to dPE/HOPG substrates for (top to bottom) increasingly dilute solutions of AuNWs, and (left to right) increasingly long exposure of the substrate to AuNW solution. Scale bars are 400 nm. (b) Histogram showing AuNW lengths for 150 AuNWs from 5 different substrates. (c) Plot demonstrating the effects of AuNW solution concentration and duration of substrate exposure on the surface coverage of the substrate. (c) AFM images of AuNW adsorption morphology at short time points. Scale bars are 70 nm.

We also note that the OLAm concentration decreases from 44 mM to 2.2 mM as the AuNWs are diluted from 60 nM to 3 nM; it is possible that the concentration of both AuNWs and OLAm molecules in solution impact adsorption. For instance, one recent study suggests that unbound OLAm can influence the solution bundling behavior of AuNWs through an entropically driven mechanism,[90] which in this case may additionally impact the assembly morphology of AuNWs adsorbed from solution. While a correlation between AuNW bundling in solution and subsequent assembly morphology on dPE/HOPG has not been quantified explicitly, Figure A.4 shows AFM images of AuNW solutions (equivalent to 60 nM, 6 nM, and 3 nM [AuNW] in Figure A.3) exposed to bare HOPG to assess possible differences in bundled AuNW deposition. Overall,

we do not observe differences in adsorption patterns that point to large differences in bundling of AuNWs across the concentration range investigated here.

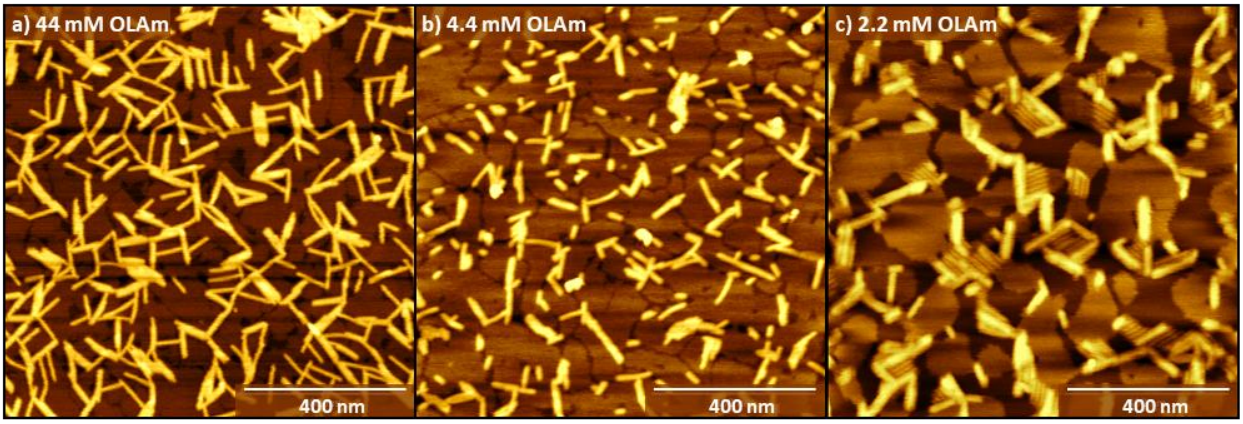

Figure A.4. Bundling behavior of AuNWs. AFM images illustrating the adsorption of individual AuNWs and bundles of AuNWs to freshly cleaved HOPG surfaces from AuNW solutions with (a) 44 mM OLAm (b) 4.4 mM OLAm and (c) 2.2 mM OLAm.

To better understand the AuNW adsorption and assembly process at dPE/HOPG surfaces, we designed experiments to examine the extent to which classical models of adsorption describe the processes that result in nematic and ribbon assemblies of AuNWs. Here, we fit AuNW adsorption trends using both the Langmuir and Freundlich models. Although AuNW concentrations below 60 nM predominantly produced non-ribbon assembly, occasionally areas of ribbon phase were observed at lower concentrations. To compare adsorption rates for ribbon and nematic assembly, we analyzed surface coverage separately for ribbon and non-ribbon areas of these samples.

Langmuir isotherms were generated for nematic areas (similar to AFM image in Figure A.5a) formed after 1 min and 60 min of substrate exposure to the AuNW solution, and for ribbon assemblies (similar to Figure A.5c) formed after 1 min. Data are plotted in Figure A.5b, using a linear form of the Langmuir model $\frac{1}{q} = \frac{1}{Kq_{max}} * \frac{1}{C} + \frac{1}{q_{max}}$ (q = surface coverage, C = [AuNW], K = constant). Linear fits, observed here for nematic surface coverage at both time points (Figure A.5d, blue and gold traces), indicate similarity to the Langmuir model. The non-linear curve observed for ribbon assemblies suggests that the Langmuir model does not describe this adsorption behavior (Figure A.5d).

AFM images of ribbon phase assemblies (Figure A.5c) show large areas of the dPE template where AuNWs are not adsorbed, which may suggest the heat of adsorption is not uniform across the surface (*e.g.* due to collective headgroup dipole reorientation near AuNW ribbons). However, the Freundlich adsorption model, which models adsorption at surfaces with non-uniform adsorption enthalpies, is also unfit to describe ribbon phase adsorption. A linear form of the Freundlich model $\log q = \log K + \frac{1}{n}\log C$ (q = surface coverage, C = [AuNW], K,n = constants), is used to plot ribbon phase adsorption data in Figure A.5e. We again observe a non-linear curve, demonstrating that ribbon phase adsorption is not adequately described by the Freundlich model.

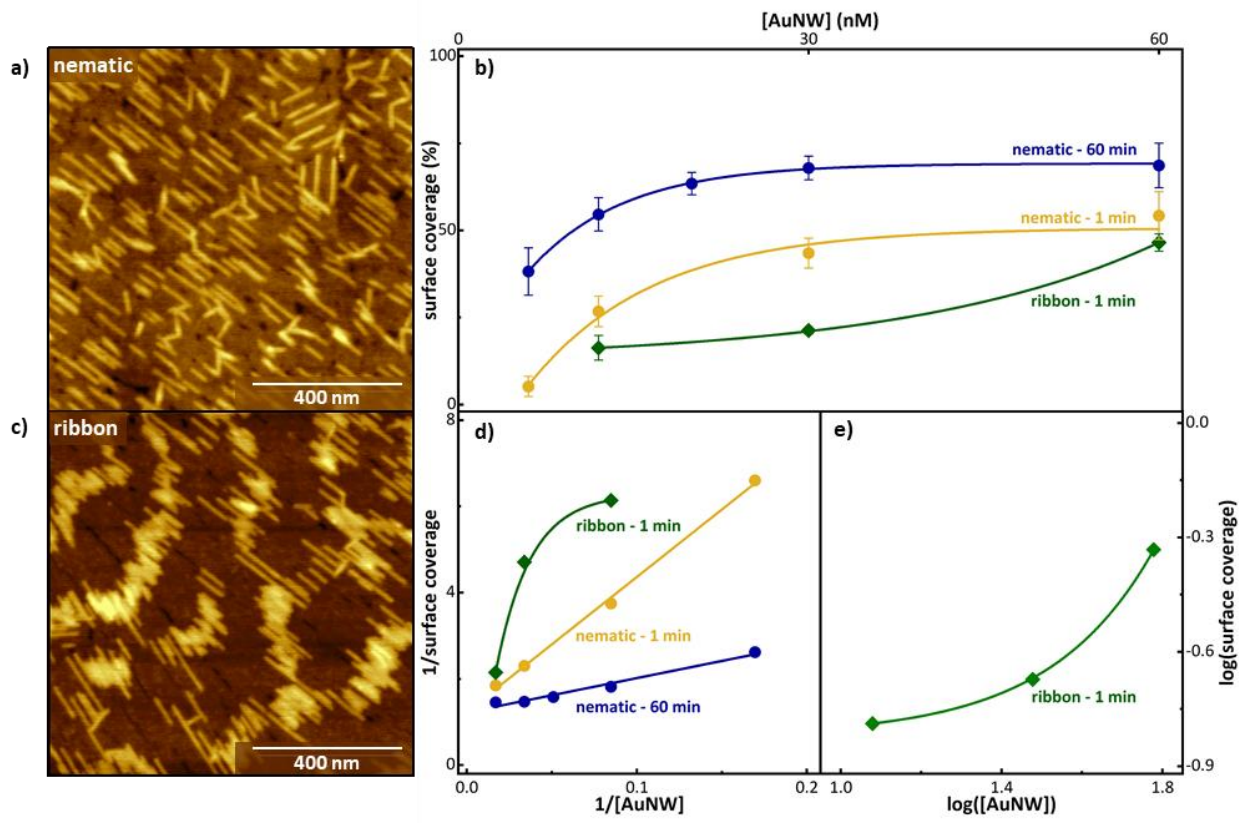

Figure A.5. Comparison of AuNW adsorption to Langmuir and Freundlich adsorption models. (a,c) AFM images depicting (a) nematic and (c) ribbon assemblies of AuNWs on dPE/HOPG surfaces. (b) Langmuir isotherm for nematic assemblies after 1 min and 60 min of exposure to AuNW solution (circles) and ribbon assemblies after 1 min (diamonds). (d) Linear Langmuir adsorption isotherm for nematic assemblies after 1 min and 60 min of exposure to AuNW solution (circles) and ribbon assemblies after 1 min (diamonds). (e) Linear Freundlich isotherm for ribbon phase assemblies after 1 min of exposure to AuNW solution.

SEM images showing long-range ordering of AuNWs assembled on dPE/HOPG substrates with long-range order.

In Chapter 3, Figure 3.4 includes AFM and SEM images of AuNW ribbon phases. In Figures A.6–A.8, we include the full-size images to demonstrate the length scale over which uniform ribbon phase assembly is observed. dPE striped phases exhibiting long-range order were prepared using TCR-LS conversion (see Experimental Methods) to yield molecular domains large enough to observe ribbon phase assembly of AuNWs ~450 nm in length. In regions of the substrate with high spatial densities of step edges, we in some cases observe high contrast defects which may be attributed to standing phases of OLAm that were not removed by the cyclohexane rinse.

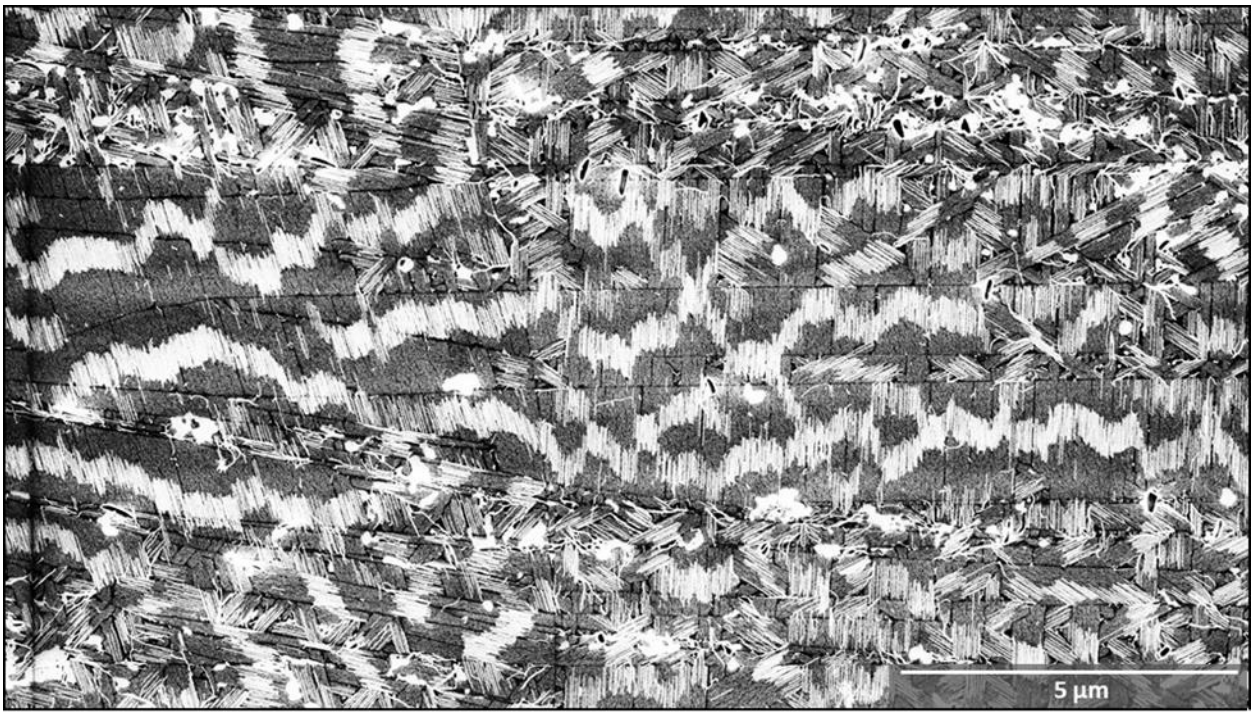

Figure A.6. Long-range ordering in ribbon-phase assembly on dPE template, scale bar 5 µm.

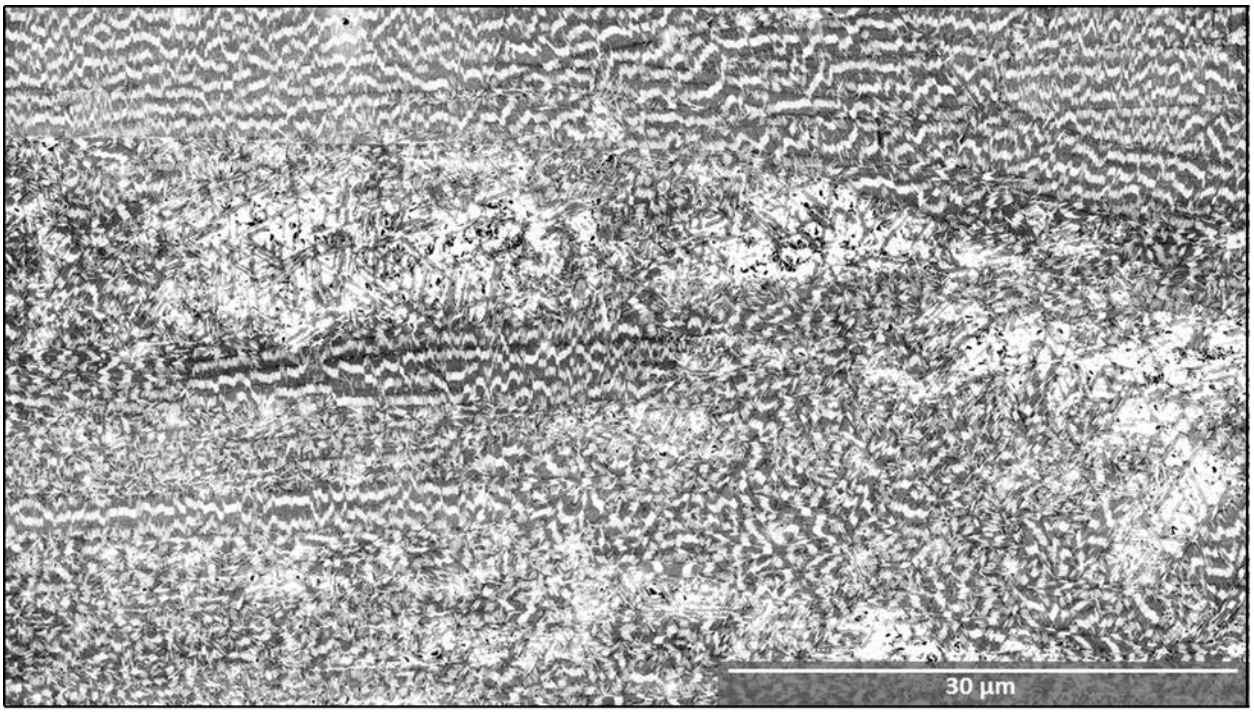

Figure A.7. Long-range ordering in ribbon-phase assembly on dPE template, scale bar 30 µm.

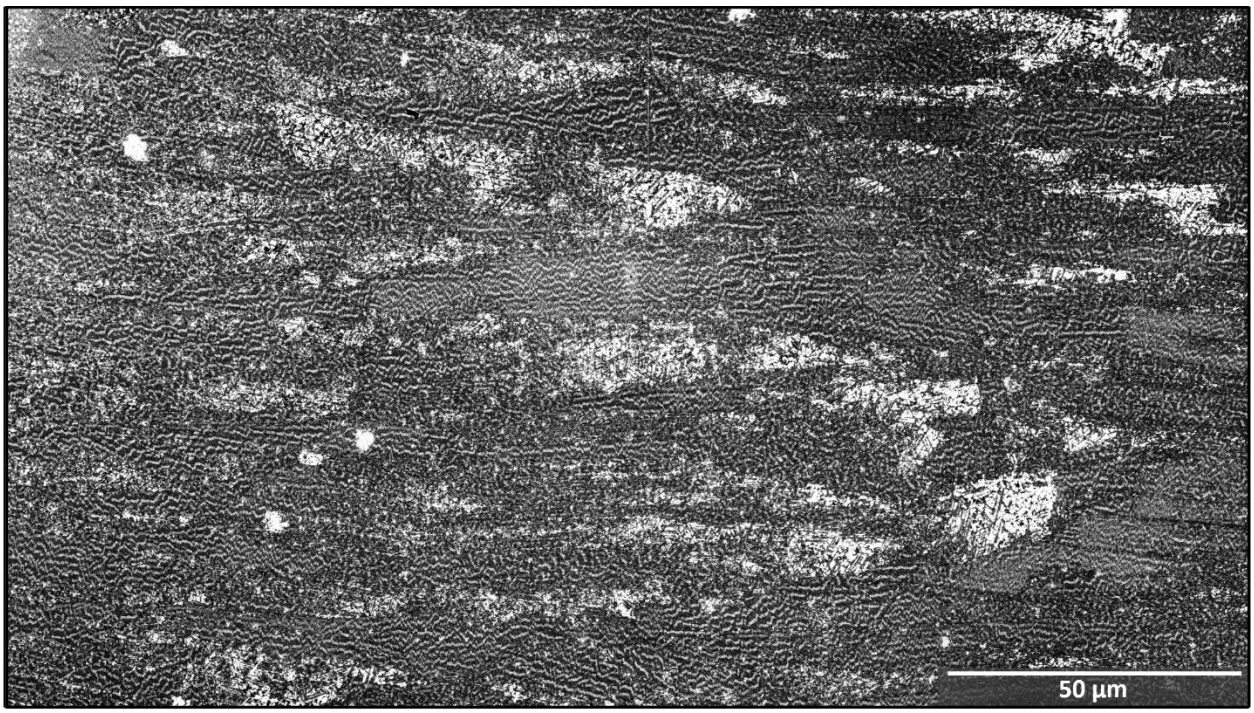

Figure A.8. Long-range ordering in ribbon-phase assembly on dPE template, scale bar 50 µm.

AFM images showing differences in T_R between OLAm reagents.

In Chapter 3, Figure 3.5 includes AFM images showing the difference in T_R for AuNWs synthesized using different OLAm reagents. The AFM topography images in Figure A.9 illustrate observed assembly morphologies for a wider range of temperatures.

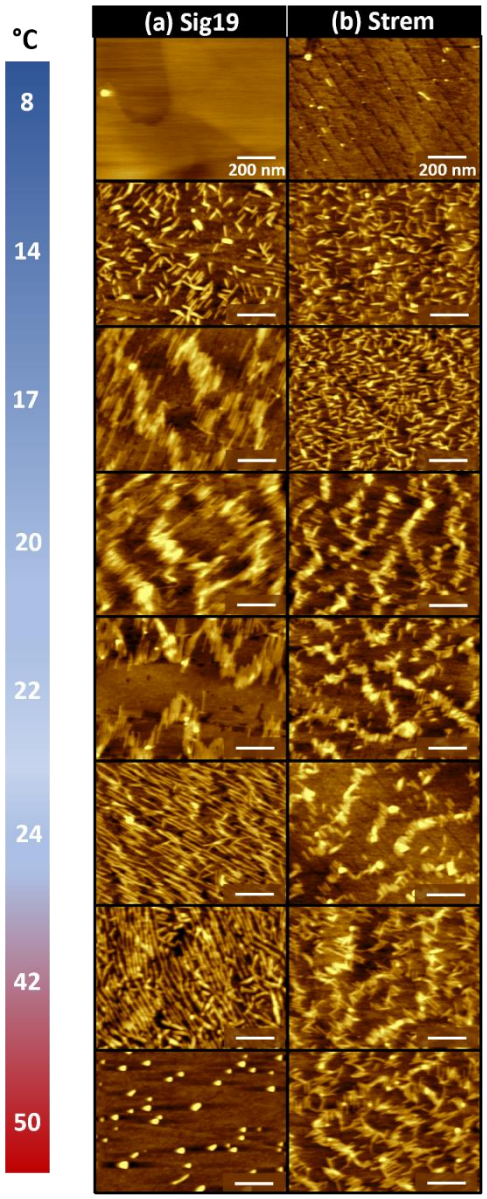

Figure A.9. AFM images of AuNWs adsorbed to dPE/HOPG substrates from AuNW solutions equilibrated to different temperatures. AuNWs were synthesized using (a) Sig19 OLAm and (b) Strem OLAm

AuNWs synthesized using Sig19 OLAm (Figure A.9a) undergo a transition from ribbon phase to nematic assembly between 22–24°C. At 50 °C, restructuring of Sig19 AuNWs is observed, likely due to Rayleigh instability. In contrast, AuNWs synthesized using Strem OLAm (Figure A.9b) assemble into ribbon phases through a much greater range, with ribbons still evident at temperatures as high as 50 °C.

Mass spectrometry analysis of OLAm reagents.

The full mass spectra for the as-received OLAm reagents are included in Figures A.10–12. A table of observed m/z values, molecular formulas matched to within 0.002 m/z difference, and relative abundances normalized to the parent ion (m/z = 268.300) for each OLAm reagent are also included. A high resolution mass spectrum of the as-synthesized *cis*-OLAm is included in Figure A.13; all peaks with relative abundance >3% have been labeled. High-resolution mass spectra were collected at the Purdue University Analytical Mass Spectrometry Facility.

a)

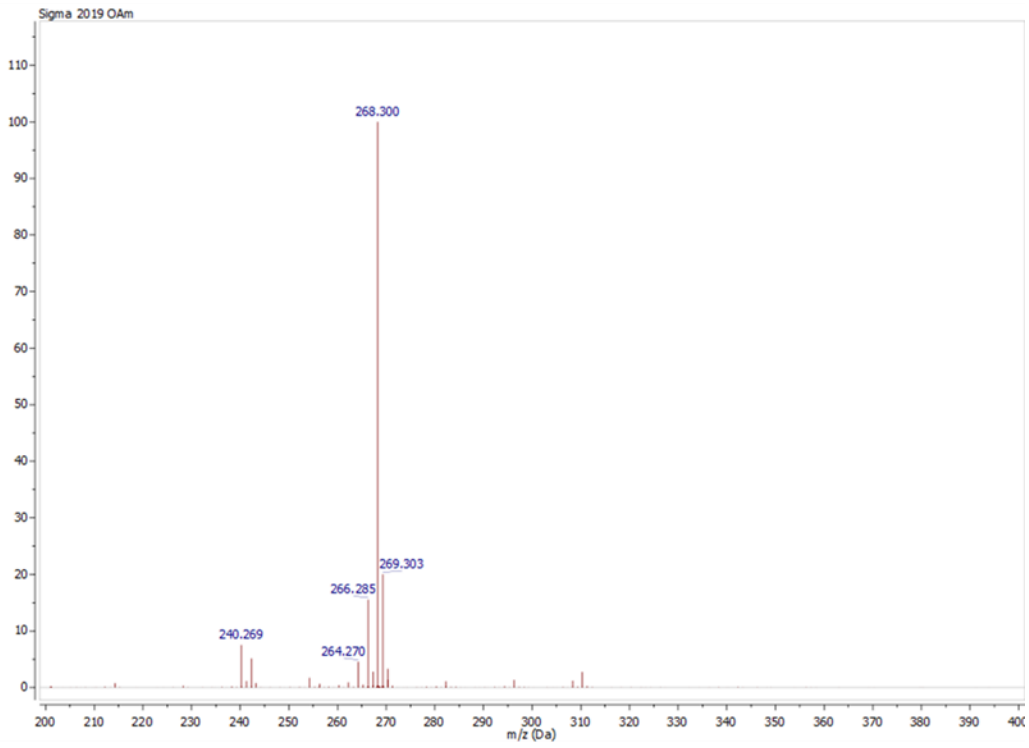

b)

m/z	formula	descriptor	exact mass (amu)	difference (ppm)	abundance	change from parent
268.300	$C_{18}H_{38}N$	18:1 e,z	268.3004	-1.58	100	parent
269.303	isotope	18:1 e,z (i)			20.03	isotope
266.285	$C_{18}H_{36}N$	18:2 e,z	266.2848	0.84	15.54	-2H
240.269	$C_{16}H_{34}N$	16:1 e,z	240.2691	-0.52	7.52	-2CH2
242.285	$C_{16}H_{36}N$	16:0 e,z	242.2848	0.93	5.14	-2CH2, +2H
264.270	$C_{18}H_{34}N$	18:3 e,z	264.2691	3.31	4.56	-4H
270.315	$C_{18}H_{40}N$	18:0 e,z	270.3161	-3.98	3.31	
267.289	isotope	18:2 e,z (i)			2.81	
310.311	$C_{20}H_{40}NO$	20:0 N=O	310.311	0.03	2.75	+2CH2,-2H,+O

Figure A.10. Mass spectral analysis for Sig19 OLAm including (a) full mass spectrum and (b) table of mass spectrum peaks.

a)

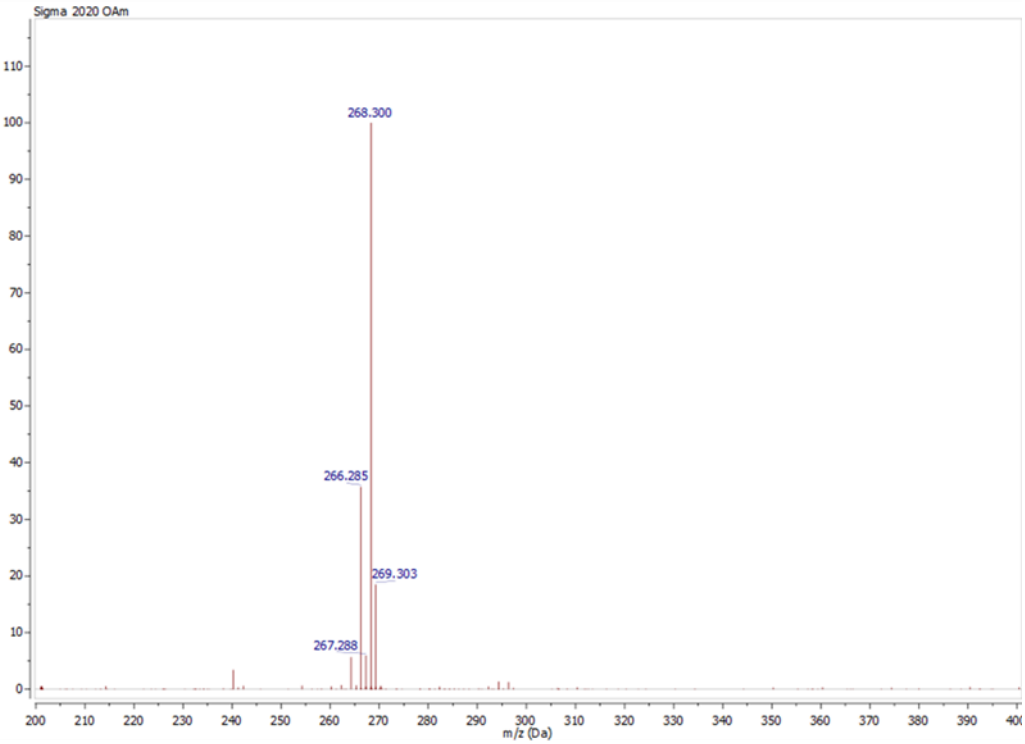

b)

m/z	formula	descriptor	exact mass (amu)	difference (ppm)	abundance	change from parent
268.300	$C_{18}H_{38}N$	18:1 e,z	268.3004	-1.58	100	parent
266.285	$C_{18}H_{36}N$	18:2 e,z	266.2848	0.84	35.74	-2H
269.303	isotope	18:1 e,z (i)			18.51	
418.404	$C_{28}H_{52}NO$		418.4049	-2.13	8.81	
267.288	isotope	18:2 e,z (i)			5.97	-2H
264.269	$C_{18}H_{34}N$	18:3 e,z	264.2691	-0.47	5.69	-4H
240.269	$C_{16}H_{34}N$	16:1 e,z	240.2691	-0.52	3.43	-2CH2
419.408	isotope	(i)			2.36	

Figure A.11. Mass spectral analysis for Sig20 OLAm including (a) full mass spectrum and (b) table of mass spectrum peaks.

a)

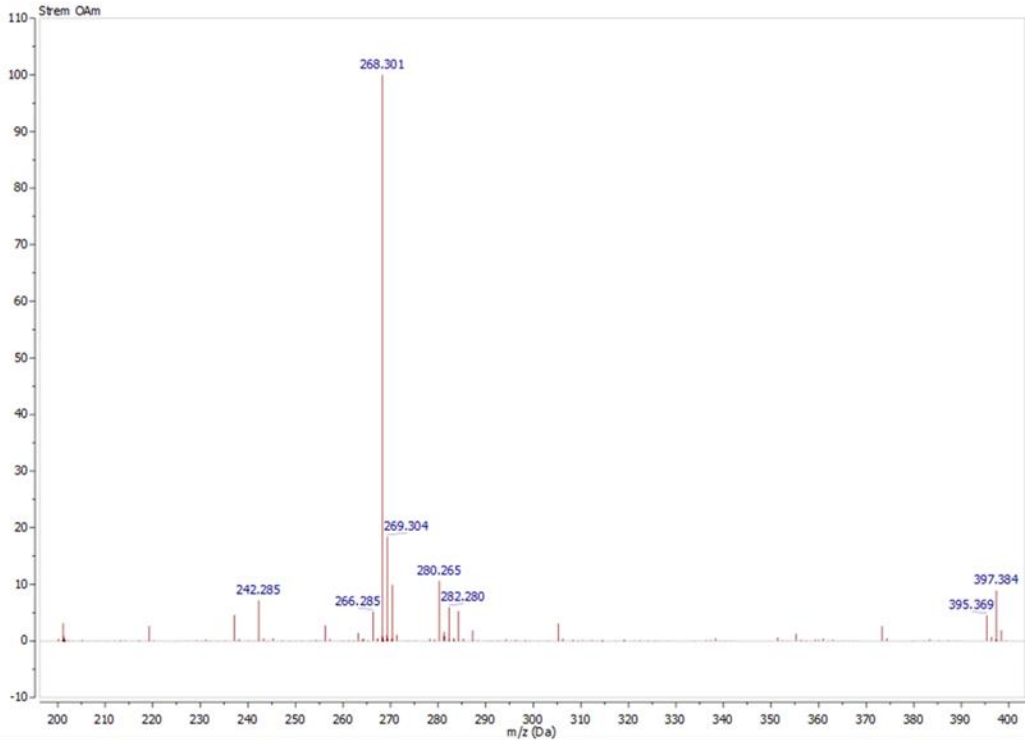

b)

m/z	formula	descriptor	exact mass (amu)	difference (ppm)	abundance	change from parent
268.301	$C_{18}H_{38}N$	18:1 e,z	268.3004	2.14	100	parent
269.304		18:1 e,z (i)			18.42	
280.265	$C_{18}H_{34}NO$		280.264	3.43	10.62	-4H, +O
270.316	$C_{18}H_{40}N$	18:0	270.3161	-0.28	9.93	+2H
397.384	$C_{29}H_{49}$ 6d.u.		397.3834	1.44	8.9	
242.285	$C_{16}H_{36}N$	16:0	242.2848	0.93	7.18	-2CH2,+2H
282.280	$C_{18}H_{36}NO$		282.2797	1.1	5.95	-2H, +O
284.296	$C_{18}H_{38}NO$		284.2953	2.32	5.28	+O
266.285	$C_{18}H_{36}N$	18:2 e,z	266.2848	0.84	5.19	
237.186	$C_{15}H_{25}O_2$ 4 d.u.		237.1855	2.3	4.59	
395.369	$C_{29}H_{47}$ 7 d.u.		395.3678	3.09	4.53	
201.164	$C_{15}H_{21}$ 6 d.u.		201.1643	-1.62	3.13	
305.249	$C_{20}H_{33}O_2$		305.2481	3.09	3.09	
256.264	$C_{16}H_{34}NO$		256.264	-0.15	2.73	
219.175	$C_{15}H_{23}O$ 5 d.u.		219.1749	0.5	2.63	
373.312	$C_{25}H_{41}O_2$ 6 d.u.		373.3107	3.6	2.63	

Figure A.12. Mass spectral analysis for Strem OLAm including (a) full mass spectrum and (b) table of mass spectrum peaks.

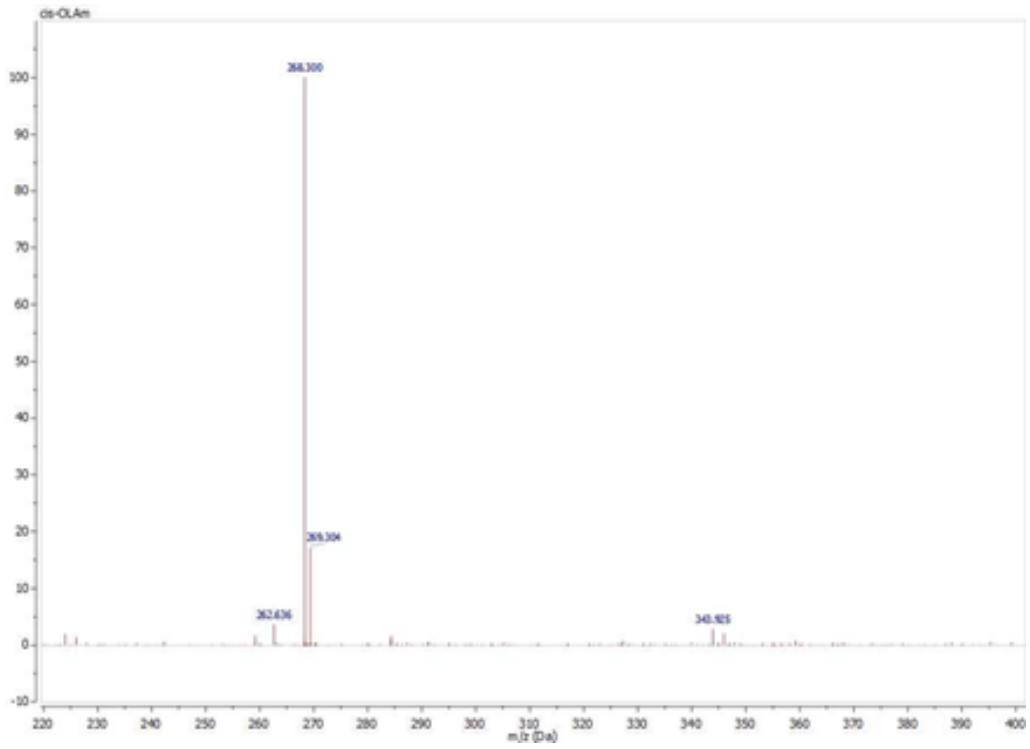

Figure A.13. Full mass spectrum of *cis*-OLAm synthesized from oleic acid. Species present in ≥ 3% relative abundance are labeled. The impurities at m/z = 262.636 and m/z = 343.925 could not be matched to a molecular formula within 0.002 m/z.

^{1}H NMR analysis of OLAm reagents.

The full ^{1}H NMR spectra for the as-received OLAm reagents dissolved in $CDCl_3$ are included in Figures A.14–A.16. Peak analysis was used to determine the *cis:trans* ratios for each reagent. The full NMR spectrum for the as-synthesized *cis*-OLAm is included in Figure A.17, with insets showing splitting patterns of vinyl and allyl protons indicating the *cis* configuration of the double bond.

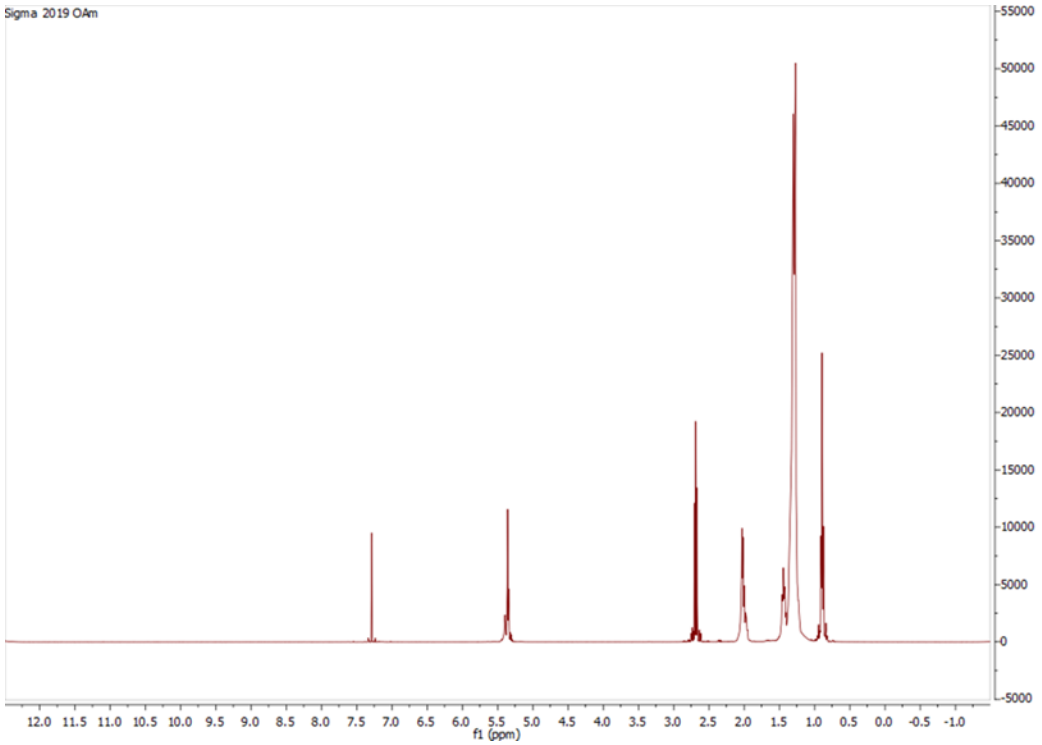

Figure A.14. Full NMR spectrum for Sig19 OLAm reagent.

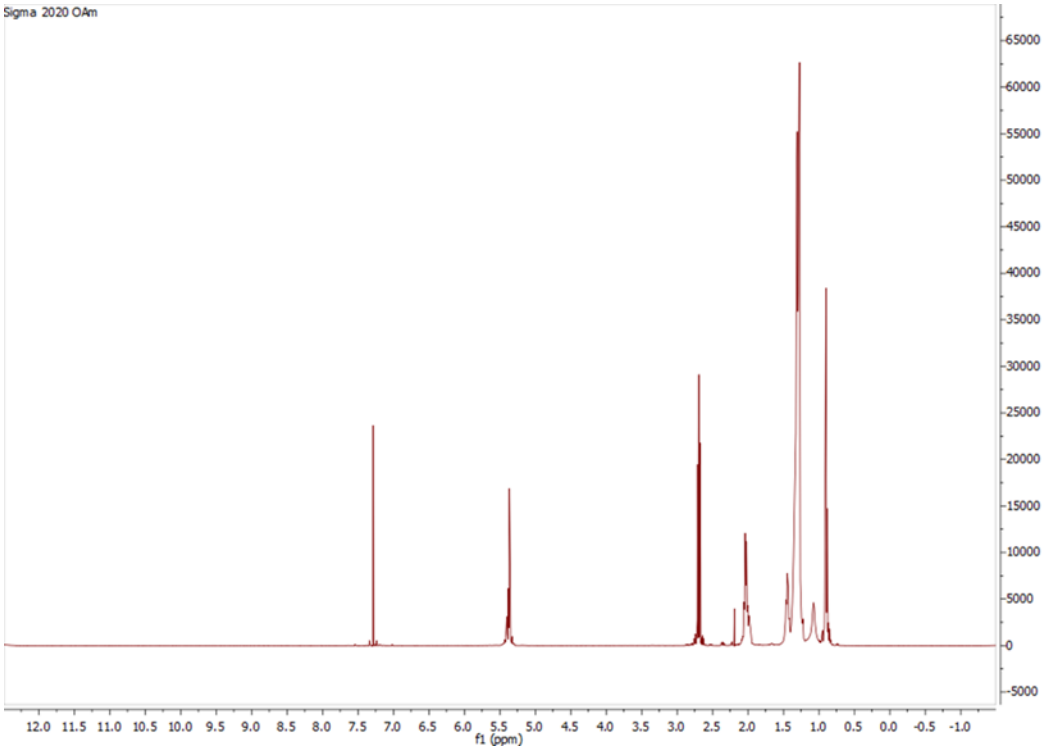

Figure A.15. Full NMR spectrum for Sig20 OLAm reagent. The singlet at 2.17 ppm is attributed to residual acetone in the NMR tube.

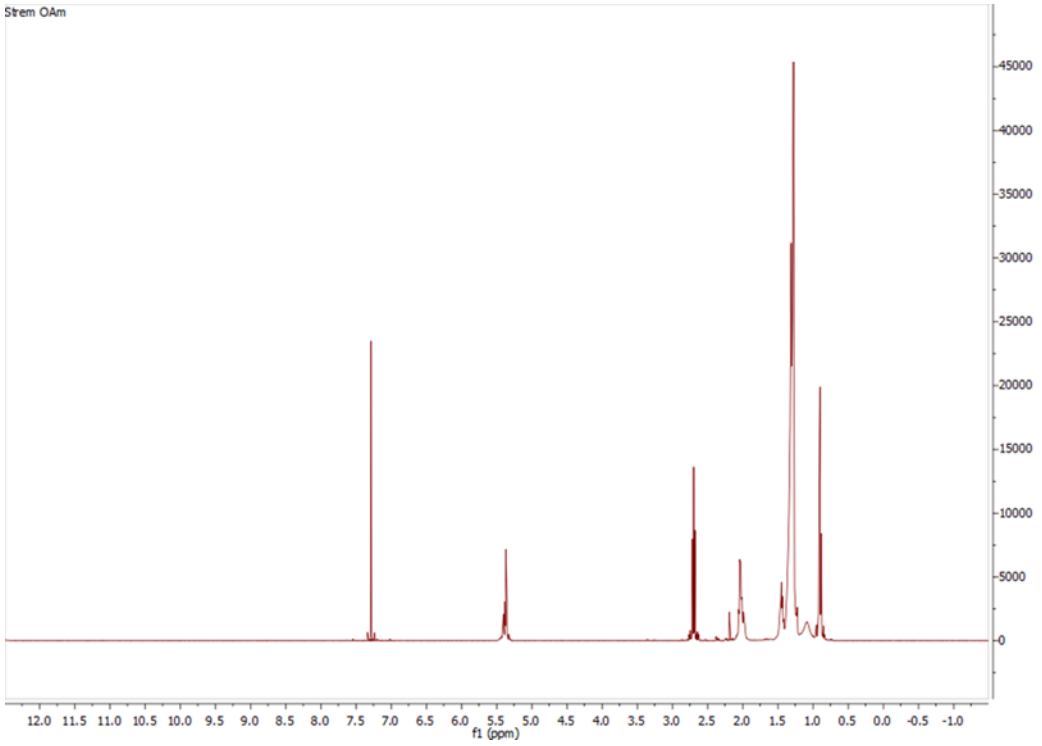

Figure A.16. Full NMR spectrum for Strem OLAm reagent. The singlet at 2.17 ppm is attributed to residual acetone in the NMR tube.

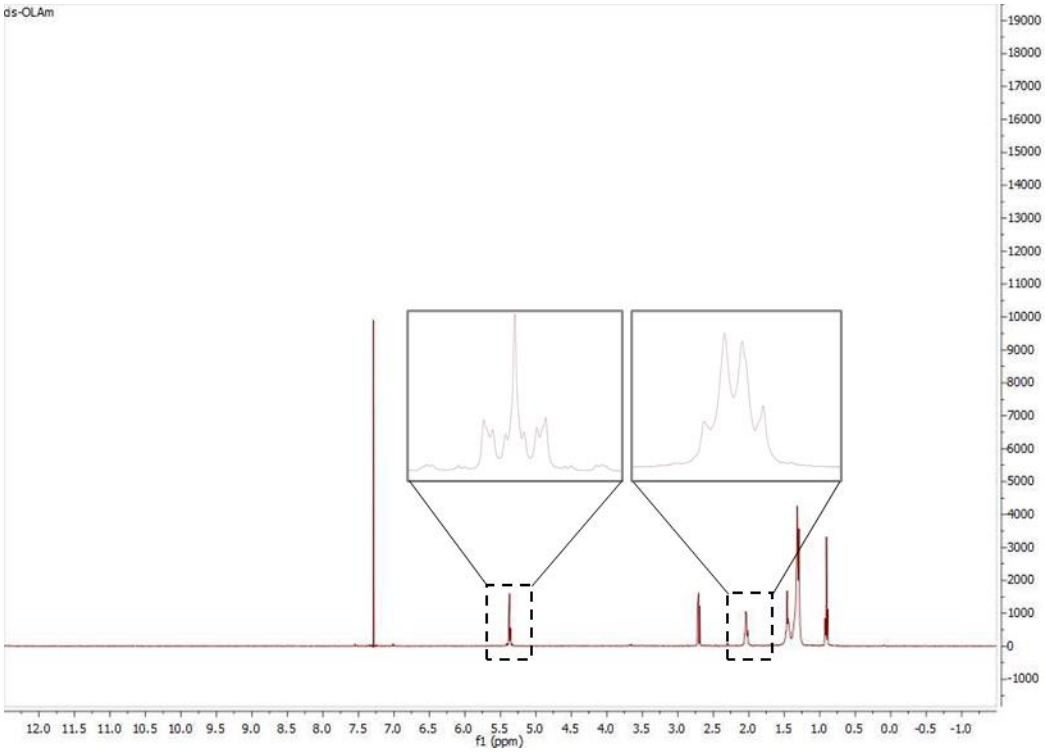

Figure A.17. Full NMR spectrum for *cis*-OLAm synthesized from oleic acid. Insets show splitting patterns of vinyl and allyl protons indicative of *cis* isomer.

Literature and estimated melting temperatures (T_m) for alkanoic acids and alkylamines.

In Chapter 3, we tabulate impurities in technical-grade OLAm blends along with literature or estimated T_m values, to illustrate possible impacts of the impurity on phase transitions. Figure A.18 lists literature T_m values for OLAm, ODAm, and HDAm, as well as their carboxylic acid analogues (OLAc, ODAc, and HDAc), and carboxylic acids structurally analogous to other amine impurities. For saturated amines, melting temperatures were typically 16-17 °C lower than the saturated carboxylic acid of the same length, whereas the CRC melting temperature for OLAm is several degrees higher than for OLAc (by 8.7 or 11.6 °C, depending on the OLAc transition).

We note that estimating a T_m for OLAm as: T_m(OLAm, *est.*) = T_m(OLAc, α) – 16 °C yields a value of -2.6 °C, similar the value determined by DSC for pure *cis*-OLAm in this work.

Chain	Head	Systematic name	Common name	Abbrev	T_m	Source
18:0	COOH	Octadecanoic acid	Stearic acid	*ODAc*	69.6	CRC-LB
18:0	**NH_2**	**Octadecylamine**	**Stearylamine**	***ODAm***	**53**	CRC-CP
16:0	COOH	Hexadecanoic acid	Palmitic acid	*HDAc*	63.1	CRC-LB
16:0	**NH_2**	**Hexadecylamine**	**Cetylamine**	***HDAm***	**46**	CRC-CP
18:1(9*Z*)	COOH	9Z-octadecenoic acid	Oleic acid	*OLAc*	13.4 (α), 16.3 (β)	CRC-LB
18:1(9Z)	**NH_2**	**9Z-octadecenamine**	**Oleylamine**	***OLAm***	**25**	CRC-CP
18:1(9E)	COOH	9E-octadecenoic acid	Elaidic acid	*ELAc*	44.5-46.6	CRC-LB
18:1(9E)	**NH_2**	**9E-octadecenamine**	**Elaidylamine**	***ELAm***	**30.5**	**[16]**
16:1 (9Z)	COOH	9Z-hexadecenoic acid	Palmitoleic acid		*-0.5 to +0.5*	CRC-LB
16:1 (9E)	COOH	9E-hexadecenoic acid	Palmitelaidic acid		*32-33*	CRC-LB
18:2 (9Z,12Z)	COOH	9Z,12Z-octadecadienoic acid	α-Linoleic		*-5.2 to -5.0*	CRC-LB
18:2 (9E,12E)	COOH	9E,12E-octadecadienoic acid	Linolelaidic		*28-29*	CRC-LB
18:3 (9Z,12Z,15Z)	COOH	9Z,12Z,15Z-octadecatrienoic acid	α-Linolenic		*-11 to -11.3*	CRC-LB
18:3 (9E,12E,15E)	COOH	9E,12E,15E-octadecatrienoic acid	Linolenelaidic		*29-30*	CRC-LB

Figure A.18. Table of literature T_m values for alkylamines common in OLAm blends, as well as for structurally analogous carboxylic acids. Literature values are from either the CRC Handbook of Lipid Bilayers[95] (CRC-LB) or CRC Handbook of Chemistry and Physics[55] (CRC-CP).

For cases in which the CRC manuals did not list a melting temperature for an amine present in reasonably large quantities in an OLAm blend, we estimate a value based on the Z/E (*cis*/*trans*) ratio for oleylamine/elaidylamine (~80%/20%) and the melting temperatures of the all-Z and all-E carboxylic acids. For instance, an estimated value for octadecadienamine (18:2 NH_3) was calculated as follows:

$$T_m(18{:}2\ NH_3, \textit{est.}) = (0.8)*T_m(18{:}2\ COOH\ (9Z,12Z)) + (0.2)*(18{:}2\ COOH\ (9E,12E)) - 16\ °C$$
$$= (0.8)(-5\ °C) + (0.2)(29\ °C) - 16\ °C = -14.2\ °C$$

The intent of these calculations is to provide the reader with an initial benchmark of whether each impurity would be expected to increase or decrease T_m for the blend in comparison with pure OLAm.

DSC thermogram of cis-OLAm and oleylammonium chloride.

To assess whether the formation of oleylammonium chloride during AuNW growth could be responsible for the appearance of a high-temperature transition in the DSC thermogram of AuNW growth solution solids for *cis*-OLAm AuNWs, we collected a DSC thermogram for a mixture of *cis*-OLAm and oleylammonium chloride. Figure A.19 shows the DSC thermogram for *cis*-OLAm with 6 mol % hydrochloric acid (HCl) added to form oleylammonium chloride. The mixture has a high-temperature melting transition at 15.9 °C, which is similar to the high-temperature melting transition for *cis*-OLAm AuNW growth solution solids that occurs at 16.2 °C.

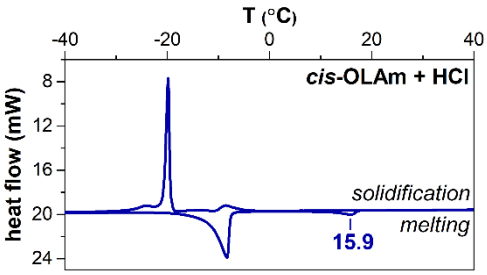

Figure A.19. DSC thermogram for *cis*-OLAm with 6 mol % HCl added to form oleylammonium chloride.

Etching of AuNW cores to assess ligand shell composition.

In the main manuscript, we characterize the impurities in each OLAm regent. Here, we carried out experiments to assess whether *trans* and saturated impurities are preferentially incorporated into the ligand shells of AuNWs. To prepare the ligand shells for characterization *via* mass spectrometry, the capping ligands were liberated through cyanide etching of the AuNW cores (Figure A.20a). [111] Briefly, AuNWs were grown under standard conditions using the OLAm reagents indicated in Figure A.20b. The AuNWs were washed by three cycles of ethanol precipitation (aided by centrifugation) to remove unbound ligands. The AuNW pellet was collected and resuspended in DCM. A 1 M aqueous solution of sodium cyanide (NaCN) was added, and the mixture was stirred at room temperature for 5 h. The organic layer was collected, rinsed with water, dried over sodium sulfate, and solvent was removed to yield the free ligands.

Mass spectra of the ligand shells (Figure A.20b) show that saturated impurities are slightly overrepresented. The abundances of octadecylamine (ODAm, *m/z*=270.316) and hexadecylamine (HDAm, *m/z*=242.285) in the ligands released from each bach of AuNWs are modestly increased relative to the OLAm reagents used to grow the AuNWs. Ligand shells of AuNWs synthesized using Sigma 2019 OLAm contained 9.77 % r.a. of ODAm and 10.37 % r.a. of HDAm, compared to 3.31 % r.a. of ODAm and 5.14 % r.a. of HDAm measured in the reagent. Similarly, ligand shells of AuNWs synthesized using Strem OLAm contained 11.74 % r.a. of ODAm and 7.18 % r.a. of HDAm (up from 9.93 % r.a. and 7.18 % r.a. respectively in the reagent). AuNWs synthesized using Sigma 2019 OLAm + 5 mol % ODAm (for 8.3 % total ODAm) contained 14.17 % r.a. ODAm in the ligand shells.

We note that this method does not enable us to assess abundance of ELAm, the most abundant impurity. It also appears that there is a small amount of variability in either ligand

incorporation, or in the quantification. For instance, the HDAm peak in the gold and green spectra would nominally be expected to be similar, since both batches use the Sigma 2019 reagent as a base (with 5 % ODAm added to the reagent used to generate AuNWs for the green spectrum). However, the measured HDAm value is slightly higher for the Sig19 AuNWs (10.37 % r.a. for Sig19 AuNWs, vs 7.05 % r.a. for Sig19 + 5 % ODAm AuNWs).

Overall, these data are likely consistent with an interpretation in which the ligand shells of all batches of nanowires are moderately enriched in *trans* and saturated chains, and that the total abundance in the ligand shell is greater for AuNWs synthesized from reagents containing larger percentages of these chains. This interpretation would also be consistent with our suggestion in Chapter 3 that $T_{O->N}$ and $T_{N->R}$ result from ligand shell order–disorder transitions. These transition temperatures are much lower for pure *cis*-OLAm AuNWs, and more similar for Sig19 and Strem AuNWs, with slightly higher values for Strem AuNWs.

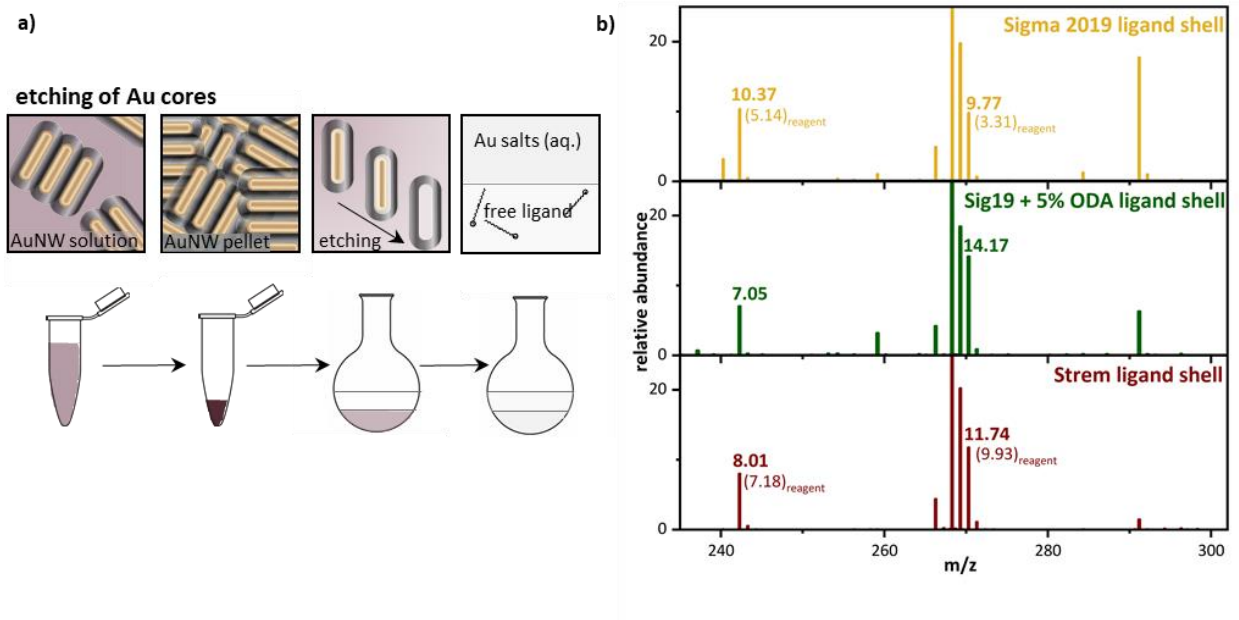

Figure A.20. (a) Schematic of AuNW core etching process, and (b) mass spectra of remaining organic components following etching. Relative abundances of HDAm and ODAm impurities are labeled. Labels in parentheses indicate the relative abundance of each impurity in the reagent.

APPENDIX B. SUPPORTING INFORMATION FOR CHAPTER 4

Limited Miscibility of Trans and Saturated Alkyl Chain Impurities in Technical-Grade Oleylamine: Impacts on Anisotropic Nanocrystal Growth

Materials and Methods.

Materials.

Ammonium hydroxide solution (28.0-30.0% NH_3 basis), oleylamine (OLAm, technical grade, 70%, lot #STBJ0354), triisopropylsilane (TIPS, 98%), oleic acid (OLAc, ≥99%), lithium aluminum hydride (95%), octadecylamine (ODAm, ≥99%), oxalyl chloride (98%), manganese (II) chloride tetrahydrate (≥99%), chloroform, anhydrous diethyl ether, and molecular sieves (4 Å) were purchased from Sigma Aldrich (Saint Louis, MO) and used as received. Diethyl ether, dichloromethane (DCM), dimethylformamide (DMF), methanol (MeOH), sodium sulfate, and sodium chloride were purchased from Fisher Scientific (Fair Lawn, NJ) and used as received. Dry cyclohexane (99.5% extra dry, Acroseal), elaidic acid (98%), and tetrachloroauric acid trihydrate (ACS reagent grade) were purchased from Acros Organics (Fair Lawn, NJ) and used as received. Oleylamine (min 95%, lot #23662300) was purchased from Strem Chemicals (Newburyport, MA) and used as received. Sodium cyanide (98%) was purchased from Alfa Aesar (Haverhill, MA) and used as received. 1,2-bis(10,12-tricosadiynoyl)-sn-glycero-3-phosphoethanolamine (dPE, >99% purity) was purchased from Avanti Polar Lipids (Alabaster, AL).

Image analysis.

Gwyddion scanning probe microscopy data visualization and analysis software[112] was used to perform plane flattening, median line corrections, and contrast adjustments for AFM images. AuNW lengths were measured using ImageJ (NIH) image processing software.[113] TEM data files were also processed using ImageJ.

Liquidous line calculation for binary phase diagrams.

The liquidous lines for binary mixtures of C18 amines were calculated based on a thermodynamic model.[114] The temperature of the liquidus line for a system in which the two components undergo ideal mixing in a liquid phase, but are completely immiscible in a solid phase,

is given by $T = \frac{T_A \Delta H_A}{\Delta H_A - RT_A \ln x_A}$. The liquidus phase boundary predicted for each binary mixture closely matches the experimentally determined boundary.

NMR analysis to determine cis:trans ratio of AuNW ligand shells.

A procedure based on the ratio method for separating spectral features of mixtures was adapted from the literature.[16] Here, the ratio method is based on the assumption that for OLAm reagents, the ^{1}H NMR spectral features for vinyl and allyl protons are linear sums of weighted spectra of *cis* and *trans* isomers:

$$reagent(\delta) = A * cis(\delta) + B * trans(\delta)$$

where δ is a chemical shift, and A and B are the amplitude weights of each isomer. The amplitude weights of each component (*cis* and *trans*) were determined using ^{1}H NMR spectra of synthesized OLAm and ELAm, and the Composite Spectrum Regression tool in OriginPro 2021 (OriginLab Corporation, Northampton, MA). The relative areas under the peaks were also calculated using OriginPro 2021. The reported *cis:trans* ratios for each reagent are averaged across vinylic and allylic protons.

Au core etching.

To collect AuNWs and remove unbound ligands, the AuNWs were extracted and washed by repeating the precipitation and centrifugation procedure listed above three times. AuNWs were then resuspended in 5 mL of DCM under stirring. To the solution of resuspended AuNWs, 5 mL of 1 M aqueous NaCN was added. The reaction mixture was stirred for 5 h under ambient conditions. The organic layer was collected, washed 3 times with milli-Q water, then dried over sodium sulfate. Solvent was removed to yield the liberated ligand molecules. The ^{1}H NMR spectrum of the crude ligand shell product dissolved in $CDCl_3$ showed significant contamination in the form of a singlet at 0.09 ppm, which was attributed to an unidentified silane impurity formed through side reactions with TIPS. The impurity was not soluble in MeOH, so the vial containing the dried ligand shell product was rinsed three times with MeOH, which separated the ligands from the impurity. Solvent was removed by rotary evaporation, then the ligands were dissolved in methanol-d4 and the ^{1}H NMR spectrum of the ligand shell was free of the silane signal.

Procedure for Langmuir-Schaefer (LS) transfer of amphiphile monolayers.

LS conversion of standing phase Langmuir films to striped phase assemblies on HOPG was performed using a Kibron (Helsinki, Finland) MicroTrough XL, as previously reported.[7, 10] Typically, 45 µL of a 0.6 mg/mL solution of dPE in $CHCl_3$ was deposited onto a subphase of 5 mM $MnCl_2$ in water at 30 °C. To allow for evaporation of the spreading solvent, the trough was allowed to equilibrate for 30 min before compressing the trough barriers at a rate of 6 mm/min. Upon compression to the desired monolayer packing density, a custom-built thermally controlled dipping apparatus reported previously[10] was used to heat a freshly cleaved HOPG substrate to 70 °C and subsequently lower the substrate into contact with the subphase for 2 min to facilitate LS conversion of the phospholipid monolayer. Transfer was carried out at a surface pressure of 30 mN/m. Upon withdrawal from the subphase, the substrate was dried under N_2. The resulting dPE monolayers were then photopolymerized by UV irradiation (254 nm) for 1 h.

AuNW assembly.

For AuNW assembly, monolayers of dPE on HOPG substrates were lowered into contact with the AuNW growth solution. The temperature of the growth solution was maintained by equilibrating in a water bath held at the desired temperature for 5 min prior to introducing the substrate; the growth solution was maintained at constant temperature throughout the AuNW adsorption process using a water bath. After 60 s of exposure to the growth solution, the substrate was removed, rinsed with 1 mL of cyclohexane, and dried under a stream of N_2. Substrates exposed to growth solutions containing significant fractions of ELAm and/or ODAm were rinsed with additional cyclohexane to remove excess adsorbed ligands, which can decrease image quality.

Procedure for synthesis of oleylamine (OLAm) from oleic acid.

The unsaturated alkyl amines were synthesized using a procedure modified from the literature.[108] Oleic acid (2.25 mL, 7 mmol) was dissolved in 25 mL of dichloromethane (DCM) at room temperature under N_2. Three drops of N,N-dimethylformamide (DMF) were added to the mixture, followed by oxalyl chloride (0.78 mL, 9.2 mmol). The reaction was stirred overnight at room temperature under an atmosphere of N_2. Solvent and excess oxalyl chloride were removed *via* rotary evaporation to yield oleoyl chloride as a yellow/orange oil.

Ammonium hydroxide solution (100 mL) was charged to a round bottom flask and cooled to 0 °C. A solution of oleoyl chloride (1.25 g) in 5 mL tetrahydrofuran (THF) was added dropwise under vigorous stirring, forming a white precipitate. The mixture was brought to room temperature and stirred for 18 h. The product was extracted with DCM (3×100 mL). The DCM layers were then combined and washed with water. If the addition of water resulted in a cloudy single-phase mixture, the addition of a small aliquot of brine solution typically allowed the mixture to form immiscible layers. The organic layer was collected and dried over sodium sulfate. Solvent was removed to yield oleylamide as a white solid.

A slurry of oleylamide (1.09 g, 3.9 mmol) and 40 mL of anhydrous diethyl ether (Et_2O) under N_2 was brought to 0 °C. Under vigorous stirring, lithium aluminum hydride (1.47 g, 39 mmol, LAH) was added. The mixture was brought to room temperature and stirred for 20 h. The reaction was quenched at 0 °C by sequential addition of 1.5 mL water, 1.5 mL of 15% NaOH in water, and 4.5 mL water. The mixture was filtered, and the organic layer was collected and dried over sodium sulfate. Solvent was removed to yield OLAm as a transparent, pale yellow oil (~80% yield).

Procedure for synthesis of elaidylamine (ELAm) from elaidic acid.

Elaidic acid (3.65 g, 12.9 mmol) was dissolved in 40 mL of DCM at room temperature under N_2. Under stirring, three drops of DMF were added to the mixture, followed by oxalyl chloride (1.42 mL, 16.8 mmol). The reaction was stirred overnight under an atmosphere of N_2 at room temperature. DCM and excess oxalyl chloride were removed via rotary evaporation to yield elaidoyl chloride as an orange oil.

A round bottom flask charged with 100 mL of ammonium hydroxide solution was brought to 0 °C. A solution of elaidoyl chloride dissolved in minimal THF was added dropwise under vigorous stirring, producing a white precipitate. The mixture was brought to room temperature and stirred for 16 h. Then, 100 mL of DCM was added to the reaction mixture and stirred for 30 min, forming an emulsion that was very slow to separate. Adding 30 mL of $CHCl_3$ to the reaction mixture typically induced phase separation. The product was extracted an additional two times using a mixture of DCM/$CHCl_3$. The organic layers were combined and rinsed 3× with brine. The organic layer was collected and dried over sodium sulfate. Solvent was removed via rotary evaporation to yield elaidylamide as a white solid.

A slurry of elaidylamide (2.88 g, 10.2 mmol) in 60 mL of anhydrous Et_2O was brought to 0 °C under N_2. Under vigorous stirring, LAH (3.90 g, 103 mmol) was added. The mixture was stirred for 20 h at room temperature. The reaction mixture was brought to 0 °C and quenched by sequential addition of 3.9 mL water, 3.9 mL of 15% NaOH in water, and 11.7 mL of water. The mixture was filtered and rinsed with Et_2O. The filtered solution was collected and dried over sodium sulfate. Solvent was removed to yield ELAm as a white solid.

Purification of OLAm and ELAm by flash chromatography.

To remove trace impurities, OLAm and ELAm were purified using a silica column. The silica was pre-treated with a 1% triethylamine solution to prevent the amines from sticking to the column. The mobile phase was 9:1 DCM/MeOH, with enough triethylamine added to account for 1% of the total volume.

Equilibration of binary mixtures of OLAm and ELAm for DSC thermograms.

Heating thermograms for binary mixtures of OLAm and ELAm collected after cooling the sample at a rate of >10 °C/min and holding the sample at -40 °C for three minutes exhibit an exothermic heating effect at -9.5 °C (Figure B1a, blue trace). The observation of an exothermic signal induced by heating suggests that solidifying the mixture by cooling the sample at a rate of >10 °C/min resulted in a metastable phase; heat is evolved during the transition from metastable phase to stable phase, which occurs upon increasing the temperature of the binary mixture.[68] To ensure that the exothermic heat effect did not alter the positions of endothermic transitions, we first heated the solid mixture to the temperature at which the exothermic peak was observed and held the sample at that temperature for five minutes, then cooled the sample again before collecting the heating thermogram (Figure B.1b). Addition of the isothermal pause to the experimental procedure allowed for equilibration of the solid to the stable state, which did not exhibit an exothermic heat effect upon melting (Figure B1a, yellow trace). Notably, the positions of the endothermic transitions of the binary mixture were unchanged by allowing the sample to equilibrate to the stable form before melting.

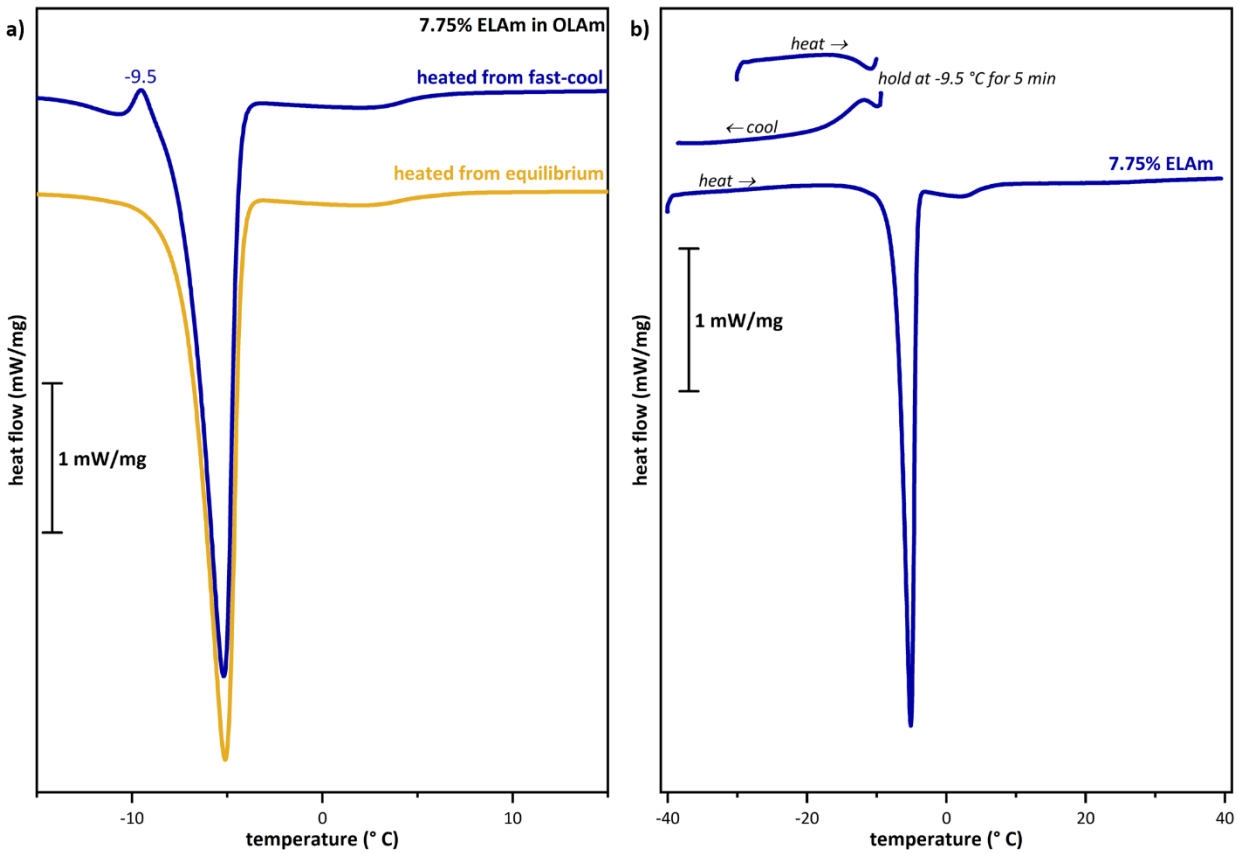

Figure B.1. DSC heating thermograms collected at a rate of 2 °C/min for a binary mixture of OLAm + 7.75% ELAm with (a, yellow trace) and without (a, blue trace) an isothermal pause. An overview of the procedure for equilibrating the binary mixture (b).

Importance of sample cooling rate for peak position in DSC heating thermograms of ternary ligand mixtures.

The heating thermograms in Figure 4.3 in Chapter 4, as well as the top trace in Figure B.2 (below) were collected after cooling ternary mixtures of ligands as quickly as the instrument allowed (>10 °C/min). The resulting thermograms exhibit a broad feature at *ca.* -10 °C consisting of two overlapping endothermic transitions. To determine whether each endothermic peak could be attributed to its own phase, or whether the smaller of the two peaks may represent the melting of a metastable phase formed by rapid cooling of the sample, we performed experiments in which the ternary mixture was cooled from the melt at controlled rates. The relative area of the smaller peak centered near -7 °C was reduced from ~15% when the mixture was rapidly cooled from the melt to ~3% when cooled at a rate of 2 °C/min (center trace). The sample exhibited only one endothermic transition after cooling at a rate of 0.5 °C/min. The dependence of the shoulder peak

near -7 °C on the rate at which the ternary mixture was cooled from the melt suggests that the shoulder represents the melting of a kinetically trapped metastable phase formed by cooling at a rate that does not allow the sample to reach thermal equilibrium. The position of the main endothermic transition is not altered by the shoulder peak.

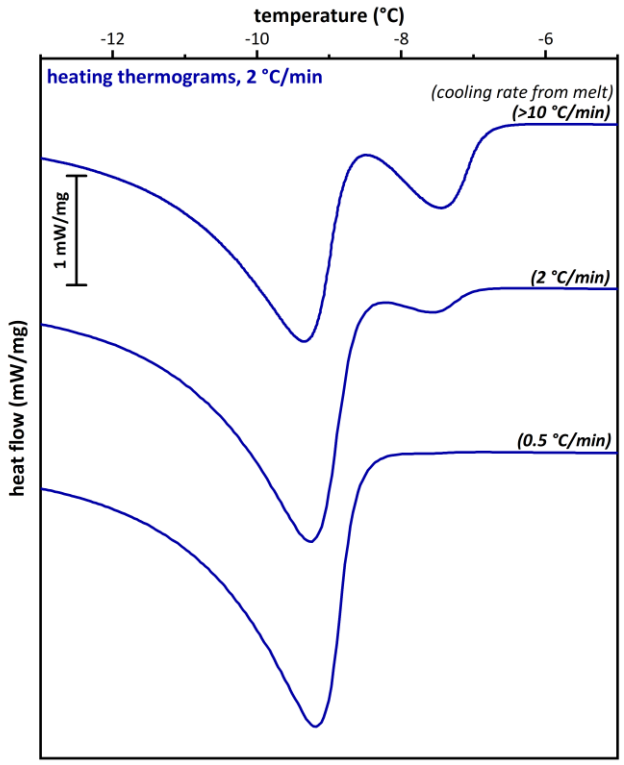

Figure B.2. Heating thermograms for a 3:1 mixture of OLAm/ELAm containing 6.10% ODAm after cooling the melt at >10 °C/min (top trace), 2 °C/min (center trace), and 0.5 °C/min (lower trace). All heating thermograms in the main manuscript were collected at a rate of 2 °C/min.

Savitzky-Golay smoothing of UV-Vis-NIR spectra for 8:2 OLAm/ELAm sample.

The UV-Vis-NIR spectra collected to monitor the early stages of AuNW growth for the sample prepared with an 8:2 OLAm/ELAm ligand blend were particularly noisy, likely due to low transmittance of the sample (Figure B.3a). The spectra were smoothed by applying a Savitzky-Golay filter using OriginPro 2021 (Figure B.3b).

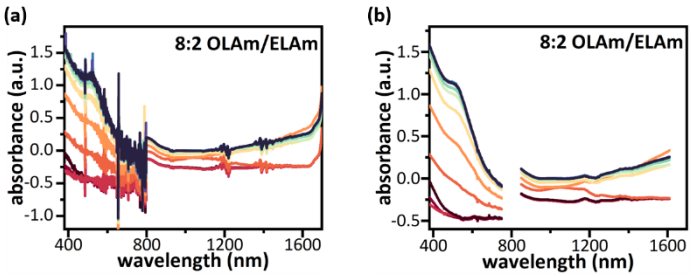

Figure B.3. UV-Vis-NIR spectra collected to monitor the initial growth of AuNWs synthesized using 8:2 OLAm/ELAm (a) before and (b) after applying the Savitzky-Golay smoothing filter.

Effect of ODAm on AuNW length.

In Chapter 4, Figure 4.8 shows a plot summarizing wire length data for AuNWs synthesized using blends of OLAm and ODAm. Here we show representative TEM images for all conditions, as well as histograms showing the distribution of wire lengths for each sample (Figure B.4).

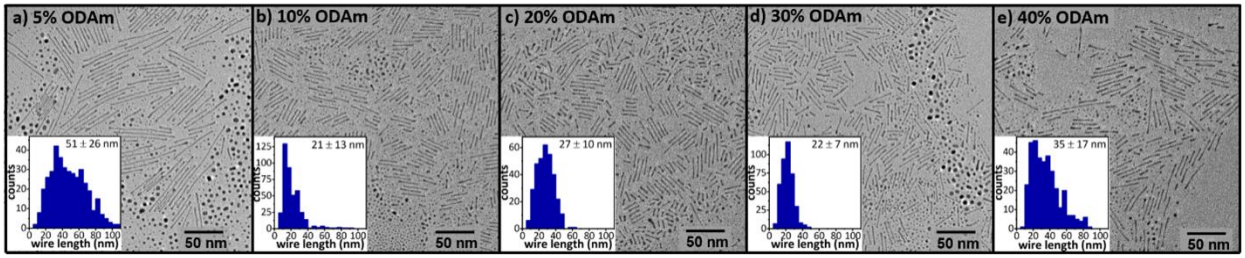

Figure B.4. TEM images of AuNWs synthesized using ligand mixtures of OLAm and ODAm with histograms (insets) showing the resulting wire length distribution. AuNWs were synthesized using a) 5% ODAm, b) 10% ODAm, c) 20% ODAm, d) 30% ODAm, and e) 40% ODAm.

Effect of ELAm on AuNW length

In Chapter 4, Figure 4.8 shows a plot summarizing wire length data for AuNWs synthesized using blends of OLAm and ELAm. Here we show representative TEM images for all conditions as well as histograms showing the distribution of wire lengths for each sample (Figure B.5).

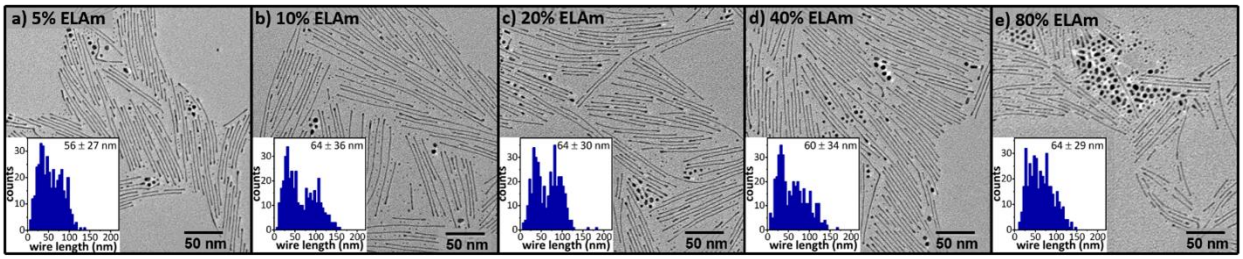

Figure B.5. TEM images of AuNWs synthesized using ligand mixtures of OLAm and ELAm with histograms (insets) showing the resulting wire length distribution. AuNWs were synthesized using a) 5% ELAm, b) 10% ELAm, c) 20% ODAm, d) 40% ELAm, and e) 80% ELAm.

Stability of surface adsorbed AuNWs is dependent on ligand composition.

In the Chapter 4, Figure 4.9 shows AFM topography images of AuNWs synthesized using specified ligand blends at controlled time points after adsorption onto dPE/HOPG substrates. Here we show larger versions of the images from the main manuscript, as well as images from additional time points, and data for AuNWs synthesized using 8:2 OLAm/ELAm. As the AuNWs age on the surface, they undergo Rayleigh instability, resulting in the formation of spherical AuNPs. However, the rate at which AuNWs are converted to AuNPs depends on the composition of the capping ligands. For AuNWs synthesized using OLAm (Figure B.6 a-d), we observed both AuNWs and AuNPs 20 min after adsorption of AuNWs. After 40 min, the relative surface coverage of AuNWs decreased, while the relative surface coverage of AuNPs increased. After 1 h, only AuNPs were observed on the surface. The surface stability of AuNWs was enhanced by the incorporation of *trans* and saturated ligands (ELAm and ODAm), with AuNWs synthesized using 9:1 OLAm/ODAm (Figure B.6 e-h) still observed on the surface after 7 h, and AuNWs synthesized using 8:2 OLAm/ELAm (Figure B.6 i-j) present after 2 h 20 min of aging on the surface.

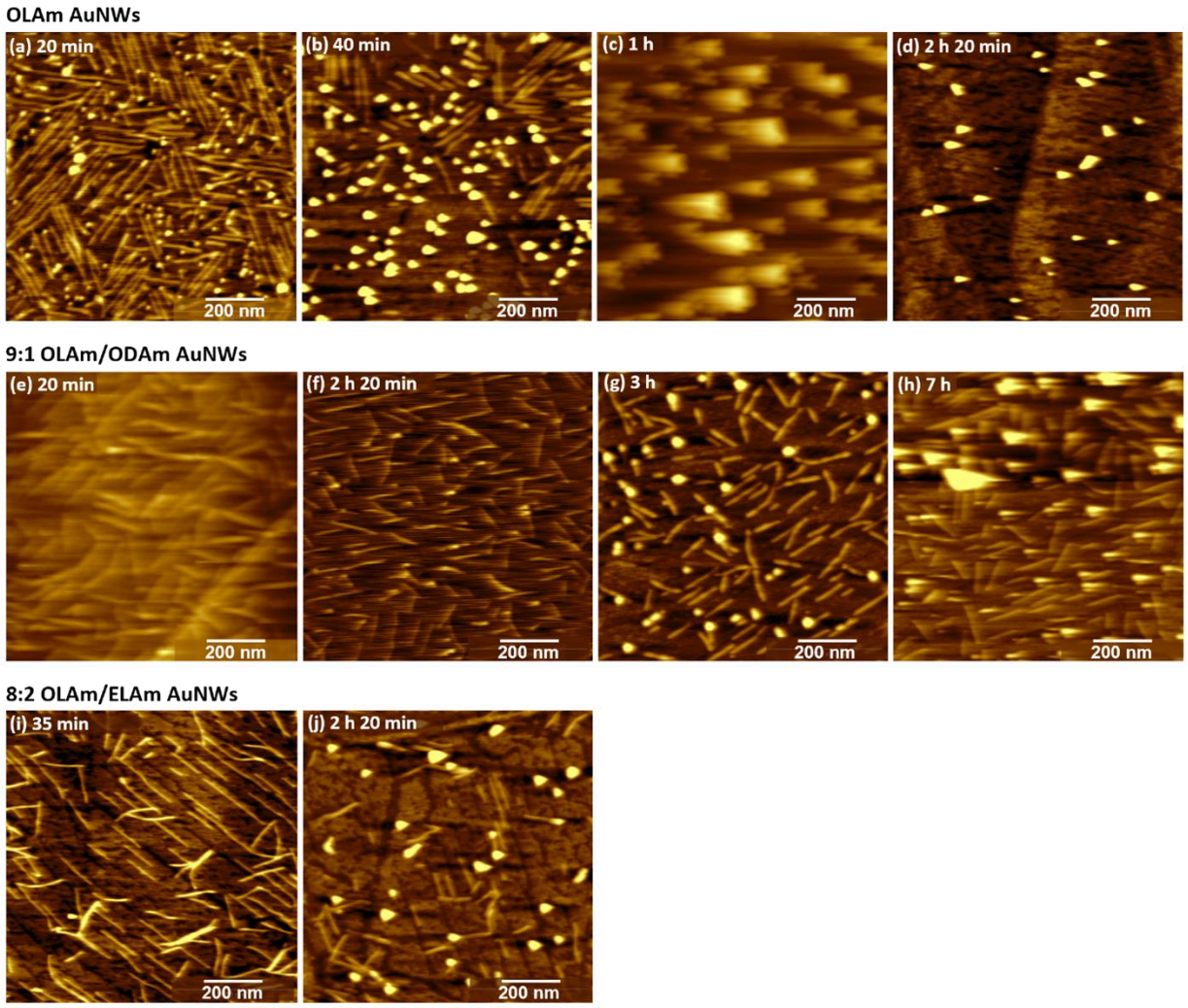

Figure B.6. AFM topography images for AuNWs synthesized using OLAm (a-d), 9:1 OLAm/ODAm (e-h), and 8:2 OLAm/ELAm (i-j) collected at various time points after adsorption on dPE/HOPG substrates.

^{1}H NMR analysis of OLAm and ELAm.

The full ^{1}H NMR spectra for the as-synthesized OLAm and ELAm dissolved in $CDCl_3$ are included in Figures B.7 and B.8 respectively. The vinyl and allyl proton signals (Figures B.7 & B.8, insests) from OLAm and ELAm were used to determine the *cis:trans* ratios of ligand shells abstracted from AuNWs, as tabulated in Figure 4.7.

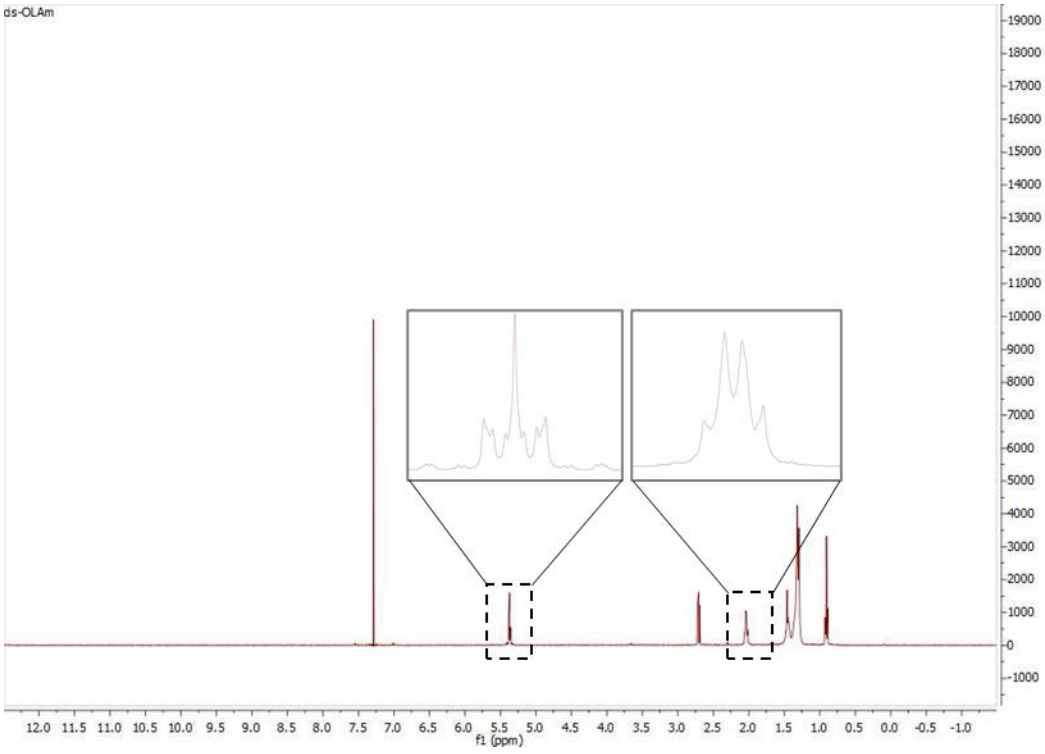

Figure B.7. Full NMR spectrum for *cis*-OLAm synthesized from oleic acid in $CDCl_3$. Insets show splitting patterns of vinyl and allyl protons indicative of *cis* isomer.

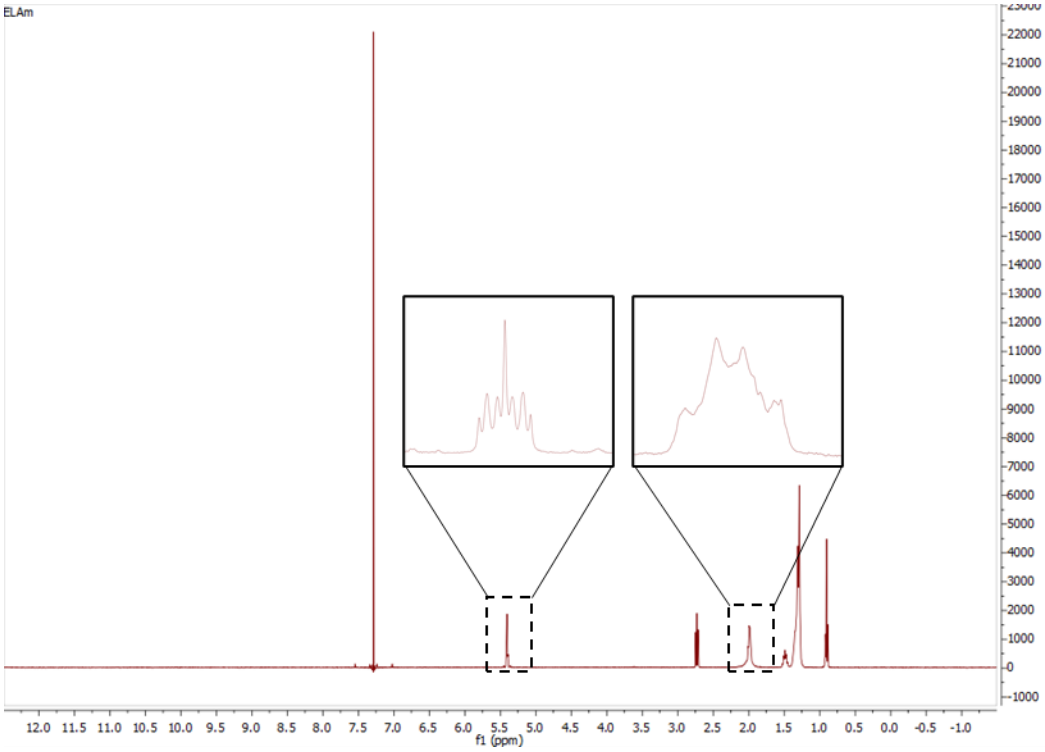

Figure B.8. Full NMR spectrum for ELAm synthesized from elaidic acid in $CDCl_3$. Insets show splitting patterns of vinyl and allyl protons indicative of *trans* isomer.

REFERENCES

(1) Paivanranta, B.; Langner, A.; Kirk, E.; David, C.; Ekinci, Y. Sub-10 nm Patterning Using EUV Interference Lithography. *Nanotechnology* **2011**, *22*.

(2) Li, L.; Liu, X.; Pal, S.; Wang, S. L.; Ober, C. K.; Giannelis, E. P. Extreme Ultraviolet Resist Materials for Sub-7 nm Patterning. *Chem. Soc. Rev.* **2017**, *46*, 4855-4866.

(3) Luckey, M. *Membrane Structural Biology: With Biochemical and Biophysical Foundations*; Cambridge University Press: Cambridge, 2014.

(4) Rabe, J. P.; Buchholz, S. Commensurability and Mobility in 2-Dimensional Molecular Patterns on Graphite *Science* **1991**, *253*, 424-427.

(5) Groszek, A. J. Preferential Adsorption of Normal Hydrocarbons on Cast Iron. *Nature* **1962**, *196*, 531-531.

(6) Groszek, A. J. Selective Adsorption at Graphite/Hydrocarbon Interfaces. *Proc. R. Soc. Lond. A* **1970**, *314*, 473-498.

(7) Bang, J. J.; Rupp, K. K.; Russell, S. R.; Choong, S. W.; Claridge, S. A. Sitting Phases of Polymerizable Amphiphiles for Controlled Functionalization of Layered Materials. *J. Am. Chem. Soc.* **2016**, *138*, 4448-4457, Article.

(8) Grim, P. C. M.; De Feyter, S.; Gesquiere, A.; Vanoppen, P.; Rucker, M.; Valiyaveettil, S.; Moessner, G.; Mullen, K.; De Schryver, F. C. Submolecularly Resolved Polymerization of Diacetylene Molecules on the Graphite Surface Observed with Scanning Tunneling Microscopy. *Angew. Chem. Int. Ed.* **1997**, *36*, 2601-2603.

(9) Okawa, Y.; Aono, M. Linear Chain Polymerization Initiated by a Scanning Tunneling Microscope Tip at Designated Positions. *J. Chem. Phys.* **2001**, *115*, 2317-2322.

(10) Hayes, T. R.; Bang, J. J.; Davis, T. C.; Peterson, C. F.; McMillan, D. G.; Claridge, S. A. Multimicrometer Noncovalent Monolayer Domains on Layered Materials Through Thermally Controlled Langmuir-Schaefer Conversion for Noncovalent 2D Functionalization. *ACS Appl. Mater. Interfaces* **2017**, *9*, 36409–36416.

(11) Porter, A. G.; Ouyang, T.; Hayes, T. R.; Biechele-Speziale, J.; Russell, S. R.; Claridge, S. A. 1-nm-Wide Hydrated Dipole Arrays Regulate AuNW Assembly on Striped Monolayers in Nonpolar Solvent. *Chem* **2019**, *5*, 2264-2275.

(12) Hayes, T. R.; Lang, E. N.; Shi, A. N.; Claridge, S. A. Large-Scale Noncovalent Functionalization of 2D Materials through Thermally Controlled Rotary Langmuir-Schaefer Conversion. *Langmuir* **2020**, *36*, 10577-10586.

(13) Gustafsson, J. O.; Lannefors, C. J. Polyquaternary Polymer as a Depressant in a Method for Froth Flotation of Potash Ores. US Patent US 9486815 B2, November 8, 2016.

(14) Kawamura, Y.; Keiji, T. Grease Composition. . U.S. Patent No. 20110195880 A1, 11 August, 2011.

(15) Abutbul, R. E.; Golan, Y. 'Beneficial Impurities' in Colloidal Synthesis of Surfactant Coated Inorganic Nanoparticles. *Nanotechnology* **2021**, *32*, 102001.

(16) Baranov, D.; Lynch, M. J.; Curtis, A. C.; Carollo, A. R.; Douglass, C. R.; Mateo-Tejada, A. M.; Jonas, D. M. Purification of Oleylamine for Materials Synthesis and Spectroscopic Diagnostics for trans Isomers. *Chem. Mater.* **2019**, *31*, 1223-1230.

(17) Lang, E. N.; Porter, A. G.; Ouyang, T.; Shi, A.; Hayes, T. R.; Davis, T. C.; Claridge, S. A. Oleylamine Impurities Regulate Temperature-Dependent Hierarchical Assembly of Ultranarrow Gold Nanowires on Biotemplated Interfaces. *ACS Nano* **2021**, *15*, 10275-10285.

(18) Liz-Marzan, L. M.; Kagan, C. R.; Millstone, J. E. Reproducibility in Nanocrystal Synthesis? Watch Out for Impurities! *ACS Nano* **2020**, *14*, 6359-6361.

(19) Millstone, J. E.; Wei, W.; Jones, M. R.; Yoo, H. J.; Mirkin, C. A. Iodide Ions Control Seed-Mediated Growth of Anisotropic Gold Nanoparticles. *Nano Lett.* **2008**, *8*, 2526-2529.

(20) Wang, F.; Tang, R.; Buhro, W. E. The Trouble with TOPO; Identification of Adventitious Impurities Beneficial to the Growth of Cadmium Selenide Quantum Dots, Rod, and Wires. *Nano Lett.* **2008**, *8*, 3521-3524.

(21) *Evonik Industries. ADOGEN 172 Product Information.* https://corporate.evonik.com/en/products/search-products/pages/product-details.aspx?productId=43640&letter=A (accessed August 20).

(22) US Environmental Protection Agency. *Assessment of Testing Needs (9-Octadecenylamine), Support Document Proposed Health Effects Test Rule Toxic Substance Control Act, Section 4*. **1986**. (accessed March 18).

(23) Wood, J. D.; Enser, M.; Fisher, A. V.; Nute, G. R.; Sheard, P. R.; Richardson, R. I.; Hughes, S. I.; Whittington, F. M. Fat Deposition, Fatty Acid Composition and Meat Quality: A Review. *Meat Sci.* **2008**, *78*, 343-358.

(24) Bockisch, M. *Fats and Oils Handbook*; AOCS Press: Urbana, IL, 1998.

(25) Millipore Sigma. *Oleylamine product information*. https://www.sigmaaldrich.com/catalog/product/aldrich/o7805 (accessed 2021 March 2).

(26) Strem Chemicals Inc. *Oleylamine product information*. https://www.strem.com/catalog/v/07-1668/nanomaterials_112-90-3 (accessed 2021 March 2).

(27) Gibson, S. Process for the Preparation of Saturated or Unsaturated Primary Fatty Amines U.S. Patent No. US 7705186 B2, April 27, 2010.

(28) Peng, X. G.; Manna, L.; Yang, W. D.; Wickham, J.; Scher, E.; Kadavanich, A.; Alivisatos, A. P. Shape Control of CdSe Nanocrystals. *Nature* **2000**, *404*, 59-61.

(29) Wang, F.; Tang, R.; Kao, J. L.-F.; Dingman, S. D.; Buhro, W. E. Spectroscopic Identification of Tri-n-octylphosphine Oxide (TOPO) Impurities and Elucidation of Their Roles in Cadmium Selenide Quantum-Wire Growth. *J. Am. Chem. Soc.* **2009**, *131*, 4983-4994.

(30) Wang, F.; Buhro, W. E. Morphology Control of Cadmium Selenide Nanocrystals: Insights into the Roles of Di-n-octylphosphine Oxide (DOPO) and Acid (DOPA). *J. Am. Chem. Soc.* **2012**, *134*, 5369-5380.

(31) Wolcott, A.; Fitzmorris, R. C.; Muzaffery, O.; Zhang, J. Z. CdSe Quantum Rod Formation Aided by In Situ TOPO Oxidation. *Chem. Mater.* **2010**, *22*, 2814-2821.

(32) Morris-Cohen, A. J.; Donakowski, M. D.; Knowles, K. E.; Weiss, E. A. The Effect of a Common Purification Procedure on the Chemical Composition of the Surfaces of CdSe Quantum Dots Synthesized with Trioctylphosphine Oxide. *J. Phys. Chem. C* **2010**, *114*, 897-906.

(33) Steckel, J. S.; Yen, B. K. H.; Oertel, D. C.; Bawendi, M. G. On the Mechanism of Lead Chalcogenide Nanocrystal Formation. *J. Am. Chem. Soc.* **2006**, *128*, 13032-13033.

(34) Boles, M. A.; Ling, D.; Hyeon, T.; Talapin, D. V. The Surface Science of Nanocrystals. *Nat. Mater.* **2016**, *15*, 141-153.

(35) Owen, J. S. The Coordination Chemistry of Nanocrystal Surfaces. *Science* **2015**, *347*, 615-616.

(36) Belman, N.; Israelachvili, J. N.; Safinya, C. R.; Bernstein, J.; Golan, Y. The Temperature-Dependent Structure of Alkyl Amines and Their Corresponding Alkylammonium-Alkylcarbamates. *J. Am. Chem. Soc.* **2009**, *31*, 9107-9113.

(37) Luo, B.; Rossini, J. E.; Gladfelter, W. L. Zinc Oxide Nanocrystals Stabilized by Alkylammonium Alkylcarbamates. *Langmuir* **2009**, *25*, 13133-13141.

(38) Abutbul, R. E.; Segev, E.; Smamuha, S.; Zeiri, L.; Ezersky, V.; Makov, G.; Golan, Y. A New Nanocrystalline Binary Phase: Synthesis and Properties of Cubic Tin Monoselenide. *CrystEngComm* **2016**, *18*, 1918-1923.

(39) Abutbul, R. E.; Toutian, E.; Galili, A.; Golan, Y. Beneficial Impurities and Phase Control in Colloidal Synthesis of Tin Monoselenide. *Langmuir* **2019**, *35*, 15855-15863.

(40) Magnussen, O. M. Ordered Anion Adlayers on Metal Electrode Surfaces. *Chem. Rev.* **2002**, *102*, 679-725.

(41) Rayavarapu, R. G.; Ungureanu, C.; Krystek, P.; van Leeuwen, T. G.; Manohar, S. Iodide Impurities in Hexadecyltrimethylammonium Bromide (CTAB) Products: Lot-Lot Variations and Influence on Gold Nanorod Synthesis. *Langmuir* **2010**, *26*, 5050-5055.

(42) Smith, D. K.; Miller, N. R.; Korgel, B. A. Iodide in CTAB Prevents Gold Nanorod Formation. *Langmuir* **2009**, *25*, 9518-9524.

(43) Ha, T. H.; Koo, H. J.; Chung, B. H. Shape-Controlled Syntheses of Gold Nanoprisms and Nanorods Influenced by Specific Adsorption of Halide Ions. *J. Phys. Chem. C* **2007**, *111*, 1123-1130.

(44) Pradhan, N.; Reifsnyder, D.; Xie, R. G.; Aldana, J.; Peng, X. G. Surface Ligand Dynamics in Growth of Nanocrystals. *J. Am. Chem. Soc.* **2007**, *129*, 9500-9509.

(45) Kim, D.; Lee, Y. K.; Lee, D.; Kim, W. D.; Bae, W. K.; Lee, D. C. Colloidal Dual-Diameter and Core-Position Controlled Core/Shell Cadmium Chalcogenide Nanorods. *ACS Nano* **2017**, *11*, 12461-12472.

(46) Liu, S.; Chen, G. Y.; Prasad, P. N.; Swihart, M. T. Synthesis of Monodisperse Au, Ag, and Au-Ag Alloy Nanoparticles with Tunable Size and Surface Plasmon Resonance Frequency. *Chem. Mater.* **2011**, *23*, 4098-4101.

(47) Cademartiri, L.; Bertolotti, J.; Sapienza, R.; Wiersma, D. S.; von Freymann, G.; Ozin, G. A. Multigram Scale, Solventless, and Diffusion-Controlled Route to Highly Monodisperse PbS Nanocrystals. *J. Phys. Chem. B* **2006**, *110*, 671-673.

(48) Farrell, D.; Majetich, S. A.; Wilcoxon, J. P. Preparation and Characterization of Monodisperse Fe Nanoparticles. *J. Phys. Chem. B* **2003**, *107*, 11022-11030.

(49) Halder, A.; Ravishankar, N. Ultrafine Single-Crystalline Gold Nanowire Arrays by Oriented Attachment. *Adv. Mater.* **2007**, *19*, 1854-1858.

(50) Lu, X. M.; Yavuz, M. S.; Tuan, H. Y.; Korgel, B. A.; Xia, Y. N. Ultrathin Gold Nanowires Can Be Obtained by Reducing Polymeric Strands of Oleylamine-AuCl Complexes Formed via Aurophilic Interaction. *J. Am. Chem. Soc.* **2008**, *130*, 8900-8901.

(51) Mourdikoudis, S.; Liz-Marzan, L. M. Oleylamine in Nanoparticle Synthesis. *Chem. Mater.* **2013**, *25*, 1465-1476.

(52) Nam, K. M.; Shim, J. H.; Ki, H.; Choi, S.-I.; Lee, G.; Jang, J. K.; Jo, Y.; Jung, M.-H.; Song, H.; Park, J. T. Single-Crystalline Hollow Face-Centered-Cubic Cobalt Nanoparticles from Solid Face-Centered-Cubic Cobalt Oxide Nanoparticles. *Angew. Chem. Int. Ed.* **2008**, *47*, 9504-9508.

(53) Park, J.; Kang, E.; Son, S. U.; Park, H. M.; Lee, M. K.; Kim, J.; Kim, K. W.; Noh, H.-J.; Park, J.-H.; Bae, C. J.; et al. Monodisperse Nanoparticles of Ni and NiO: Synthesis, Characterization, Self-Assembled Superlattices, and Catalytic Applications in the Suzuki Coupling Reaction. *Adv. Mater.* **2005**, *17*, 429-434.

(54) Esposito, S.; Beach, K. E.; Dale, T. J.; Esmacher, M. J.; Hefner, R. E.; Rossi, A. Compositions and Methods for Inhibiting Corrosion in Gas Turbine Air Compressors. World Patent No. WO 2014134491., September 4, 2014.

(55) *CRC Handbook of Chemistry and Physics*, 101st ed.; Rumble, J. R., Ed.; CRC Press: Boca Raton, 2020.

(56) Peng, X. G. Green Chemical Approaches Toward High-Quality Semiconductor Nanocrystals. *Chem. Eur. J.* **2002**, *8*, 335-339.

(57) Grzelczak, M.; Perez-Juste, J.; Mulvaney, P.; Liz-Marzan, L. M. Shape Control in Gold Nanoparticle Synthesis. *Chem. Soc. Rev.* **2008**, *37*, 1783-1791.

(58) Simons, K.; Ikonen, E. Functional Rafts in Cell Membranes. *Nature* **1997**, *387*, 569-572.

(59) Israelachvili, J. N.; Marcelja, S.; Horn, R. G. Physical Principles of Membrane Organization. *Q. Rev. Biophys.* **1980**, *13*, 121-200.

(60) Hunter, T. Signaling - 2000 and Beyond. *Cell* **2000**, *100*, 113-127.

(61) Sheets, E. D.; Holowka, D.; Baird, B. Membrane Organization in Immunoglobulin E Receptor Signaling. *Curr. Opin. Chem. Biol.* **1999**, *3*, 95-99.

(62) Janes, P. W.; Ley, S. C.; Magee, A. I.; Kabouridis, P. S. The Role of Lipid Rafts in T Cell Antigen Receptor (TCR) Signalling. *Semin. Immunol.* **2000**, *12*, 23-34.

(63) Simons, K.; Toomre, D. Lipid Rafts and Signal Transduction. *Nat. Rev. Mol. Cell Biol.* **2000**, *1*, 31-39.

(64) Burrows, N. D.; Vartanian, A. M.; Abadeer, N. S.; Grzincic, E. M.; Jacob, L. M.; Lin, W. N.; Li, J.; Dennison, J. M.; Hinman, J. G.; Murphy, C. J. Anisotropic Nanoparticles and Anisotropic Surface Chemistry. *J. Phys. Chem. Lett.* **2016**, *7*, 632-641.

(65) Pawlowska, D.; Janich, C.; Langner, A.; Dobner, B.; Wolk, C.; Brezesinski, G. The Impact of Alkyl-Chain Purity on Lipid-Based Nucleic Acid Delivery Systems - Is the Utilization of Lipid Components with Technical Grade Justified? *Chemphyschem* **2019**, *20*, 2110-2121.

(66) Ueno, S.; Suetake, T.; Yano, J.; Suzuki, M.; Sato, K. Structure and Polymorphic Transformations in Elaidic Acid (trans-ω9-Octadecenoic Acid). *Chem. Phys. Lipids* **1994**, *72*, 27-34.

(67) Inoue, T.; Hisatsugu, Y.; Yamamoto, R.; Suzuki, M. Solid-Liquid Phase Behavior of Binary Fatty Acid Mixtures 1. Oleic Acid/Stearic Acid and Oleic Acid/Behenic Acid Mixtures. *Chem. Phys. Lipids* **2004**, *127*, 143-152.

(68) Inoue, T.; Hisatsugu, Y.; Ishikawa, R.; Suzuki, M. Solid-Liquid Phase Behavior of Binary Fatty Acid Mixtures 2. Mixtures of Oleic Acid with Lauric Acid, Myristic acid, and Palmitic acid. *Chem. Phys. Lipids* **2004**, *127*, 161-173.

(69) Inoue, T.; Hisatsugu, Y.; Suzuki, M.; Wang, Z. N.; Zheng, L. Q. Solid-Liquid Phase Behavior of Binary Fatty Acid Mixtures 3. Mixtures of Oleic Acid With Capric Acid (Decanoic Acid) and Caprylic Acid (Octanoic Acid). *Chem. Phys. Lipids* **2004**, *132*, 225-234.

(70) Badia, A.; Cuccia, L.; Demers, L.; Morin, F.; Lennox, R. B. Structure and Dynamics in Alkanethiolate Monolayers Self-assembled on Gold Nanoparticles: A DSC, FT-IR and Deuterium NMR Study. *J. Am. Chem. Soc.* **1997**, *119*.

(71) Ghorai, P. K.; Glotzer, S. C. Molecular Dynamics Simulation Study of Self-Assembled Monolayers of Alkanethiol Surfactants on Spherical Gold Nanoparticles. *J. Phys. Chem. C* **2007**, *111*, 15857-15862.

(72) Luedtke, W. D.; Landman, U. Structure, Dynamics, and Thermodynamics of Passivated Gold Nanocrystallites and Their Assemblies. *J. Phys. Chem.* **1996**, *100*, 13323-13329.

(73) Yang, Y. L.; Qin, H.; Peng, X. Intramolecular Entropy and Size-Dependent Solution Properties of Nanocrystal-Ligands Complexes. *Nano Lett.* **2016**, *16*, 2127-2132.

(74) Monego, D.; Kister, T.; Kirkwood, N.; Mulvaney, P.; Widmer-Cooper, A.; Kraus, T. Colloidal Stability of Apolar Nanoparticles: Role of Ligand Length. *Langmuir* **2018**, *34*, 12982-12989.

(75) Kister, T.; Monego, D.; Mulvaey, P.; Widmer-Cooper, A.; Kraus, T. Colloidal Stability of Apolar Nanoparticles: The Role of Particle Size and Ligand Shell Structure. *ACS Nano* **2018**, *12*, 5969-5977.

(76) Wuister, S. F.; van Houselt, A.; de Mello Donega, C.; Vnanmaekelbergh, D.; Meijerink, A. Temperature Antiquenching of the Luinescence from Capped CdSe Quantum Dots. *Angew. Chem. Int. Ed.* **2004**, *116*, 3091-3095.

(77) Balan, A. D.; Olshansky, J. H.; Horowitz, Y.; Han, H.-L.; O'Brien, E. A.; Tang, L.; Somorjai, G. A.; Alivisatos, A. P. Unsaturated Ligands Seed an Order to Disorder Transition in Mixed Ligand Shells of CdSe/CdS Quantum Dots. *ACS Nano* **2019**, *13*, 13784-13796.

(78) Hoeppener, S.; Chi, L. F.; Fuchs, H. Formation of Au-55 Strands on a Molecular Template at the Solid-Liquid Interface. *Nano Lett.* **2002**, *2*, 459-463.

(79) Mezour, M. A.; Perepichka, I. I.; Zhu, J.; Lennox, R. B.; Perepichka, D. F. Directing the Assembly of Gold Nanoparticles with Two-Dimensional Molecular Networks. *ACS Nano* **2014**, *8*, 2214-2222.

(80) Widmer-Cooper, A.; Geissler, P. Orientational Ordering of Passivating Ligands on CdS Nanorods in Solution Generates Strong Rod-Rod Interactions. *Nano Lett.* **2014**, *14*, 57-65.

(81) Huo, Z. Y.; Tsung, C. K.; Huang, W. Y.; Zhang, X. F.; Yang, P. D. Sub-Two Nanometer Single Crystal Au Nanowires. *Nano Lett.* **2008**, *8*, 2041-2044.

(82) Wang, C.; Hu, Y. J.; Lieber, C. M.; Sun, S. H. Ultrathin Au Nanowires and Their Transport Properties. *J. Am. Chem. Soc.* **2008**, *130*, 8902-8903.

(83) Reiser, B.; Gerstner, D.; Gonzalez-Garcia, L.; Maurer, J. H. M.; Kanelidis, I.; Kraus, T. Multivalent Bonds in Self-Assembled Bundles of Ultrathin Gold Nanowires. *Phys. Chem. Chem. Phys.* **2016**, *18*, 27165-27169.

(84) Davis, T. C.; Bang, J. J.; Brooks, J. T.; McMillan, D. G.; Claridge, S. A. Hierarchically Patterned Noncovalent Functionalization of 2D Materials by Controlled Langmuir–Schaefer Conversion. *Langmuir* **2018**, *34*, 1353-1362.

(85) Bang, J. J.; Porter, A. G.; Davis, T. C.; Hayes, T. R.; Claridge, S. A. Spatially Controlled Noncovalent Functionalization of 2D Materials Based on Molecular Architecture. *Langmuir* **2018**, *34*, 5454-5463.

(86) Villarreal, T. A.; Russell, S. R.; Bang, J. J.; Patterson, J. K.; Claridge, S. A. Modulating Wettability of Layered Materials by Controlling Ligand Polar Headgroup Dynamics. *J. Am. Chem. Soc.* **2017**, *139*, 11973-11979.

(87) Okawa, Y.; Akai-Kasaya, M.; Kuwahara, Y.; Mandal, S. K.; Aono, M. Controlled Chain Polymerisation and Chemical Soldering for Single-Molecule Electronics. *Nanoscale* **2012**, *4*, 3013-3028.

(88) Sun, C.; Bojdys, M. J.; Clarke, S. M.; Harper, L. D.; Jefferson, A.; Castro, M. A.; Medina-Carrasco, S. Bulk and Adsorbed Monolayer Phase Behavior of Binary Mixtures of Undecanoic Acid and Undecylamine: Catanionic Monolayers. *Langmuir* **2011**, *27*, 3626-3637.

(89) Loubat, A.; Imperor-Clerc, M.; Pansu, B.; Meneau, F.; Raquet, B.; Viau, G.; Lacroix, L. M. Growth and Self-Assembly of Ultrathin Au Nanowires into Expanded Hexagonal Superlattice Studied by in Situ SAXS. *Langmuir* **2014**, *30*, 4005-4012.

(90) Bettscheider, S.; Kuttich, B.; Engel, L. F.; Gonzalez-Garcia, L.; Kraus, T. Bundling of Nanowires Induced by Unbound Ligand. *J. Phys. Chem. C* **2021**, *125*, 3590-3598.

(91) Kim, F.; Kwan, S.; Akana, J.; Yang, P. D. Langmuir-Blodgett Nanorod Assembly. *J. Am. Chem. Soc.* **2001**, *123*, 4360-4361.

(92) Li, L. S.; Walda, J.; Manna, L.; Alivisatos, A. P. Semiconductor Nanorod Liquid Crystals. *Nano Lett.* **2002**, *2*, 557-560.

(93) Talapin, D. V.; Shevchenko, E. V.; Murray, C. B.; Kornowski, A.; Forster, S.; Weller, H. CdSe and CdSe/CdS Nanorod Solids. *J. Am. Chem. Soc.* **2004**, *126*, 12984-12988.

(94) Carbone, L.; Nobile, C.; De Giorgi, M.; Sala, F. D.; Morello, G.; Pompa, P.; Hytch, M.; Snoeck, E.; Fiore, A.; Franchini, I. R.; et al. Synthesis and Micrometer-Scale Assembly of Colloidal CdSe/CdS Nanorods Prepared by a Seeded Growth Approach. *Nano Lett.* **2007**, *7*, 2942-2950.

(95) *CRC Handbook of Lipid Bilayers*, 2nd ed.; Marsh, D., Ed.; CRC Press: Boca Raton, 2013.

(96) Suzuki, M.; Ogaki, T.; Sato, K. Crystallization and Transformation Mechanisms of α,ß- and Γ- Polymorphs of Ultra-Pure Oleic Acid *J. Am. Oil Chem. Soc.* **1985**, *62*, 1600-1604.

(97) Ramamoorthy, R. K.; Yildirim, E.; Barba, E.; Roblin, P.; Vargas, J. A.; Lacroix, L. M.; Rodriguez-Ruiz, I.; Decorse, P.; Petkov, V.; Teychene, S.; et al. The Role of Pre-Nucleation Clusters in the Crystallization of Gold Nanoparticles. *Nanoscale* **2020**, *12*, 16173-16188.

(98) Lang, E. N.; Claridge, S. A. Cow-to-Cow Variation in Nanocrystal Synthesis: Learning from Technical-Grade Oleylamine. *Nanotechnology* **2022**, *33*, 082501.

(99) Shi, A.; Claridge, S. A. Lipids: An Atomic Toolkit for the Endless frontier. *ACS Nano* **2021**, *15*, 15429-15445.

(100) McLaughlin, S.; Wang, J.; Gambhir, A.; Murray, D. PIP2 and Proteins: Interactions, Organization, and Information Flow. *Annu. Rev. Biophys. Biomol. Struct.* **2002**, *31*, 151-175.

(101) Wang, Y.-H.; Collins, A.; Guo, L.; Smith-Dupont, K. B.; Gai, F.; Svitkina, T.; Janmey, P. A. Divalent Cation-Induced Cluster Formation by Polyphosphoinositides in Model Membranes. *J. Am. Chem. Soc.* **2012**, *134*, 3387-3395.

(102) Hannun, Y. A.; Obeid, L. M. Principles of Bioactive Lipid Signalling: Lessons From Sphingolipids. *Nat. Rev. Mol. Cell Biol.* **2008**, *9*, 139-150.

(103) Israelachvili, J. N.; Mitchell, D. J.; Ninham, B. W. Theory of Self-Assembly of Hydrocarbon Amphiphiles into Micelles and Bilayers. *J. Chem. Soc. Faraday Trans.* **1976**, *72*, 1525-1568.

(104) McMahon, H. T.; Gallop, J. L. Membrane Curvature and Mechanisms of Dynamic Cell Membrane Remodelling. *Nature* **2005**, *438*, 590-596.

(105) Calvin, J. J.; O'Brien, E. A.; Sedlak, A. B.; Balan, A. D.; Alivisatos, A. P. Thermodynamics of Composition Dependent Ligand Exchange on the Surfaces of Colloidal Indium Phosphide Quantum Dots. *ACS Nano* **2021**, *15*, 1407-1420.

(106) Yu, Y.; Cui, F.; Sun, J. W.; Yang, P. D. Atomic Structure of Ultrathin Gold Nanowires. *Nano Lett.* **2016**, *16*, 3078-3084.

(107) Takahata, R.; Yamazoe, S.; Koyasu, K.; Imura, K.; Tsukuda, T. Gold Ultrathin Nanorods with Controlled Aspect Ratios and Surface Modifications: Formation Mechanism and Localized Surface Plasmon Resonance. *J. Am. Chem. Soc.* **2018**, *140*, 6640-6647.

(108) Pumtang, S.; Siripornnoppakhun, W.; Sukwattanasinitt, M.; Ajavakom, A. Solvent Colorimetric Paper-Based Polydiacetylene Sensors from Diacetylene Lipids. *J. Colloid Interface Sci.* **2011**, *364*, 366-372.

(109) Maestro. version 10.1. Schrödinger, LLC: New York, NY, 2015.

(110) MacroModel. version 10.7. Schrödinger, LLC: New York, NY, 2015.

(111) Liu, X.; Yu, M.; Kim, H.; Mameli, M.; Stellacci, F. Determination of Monolayer-Protected Gold Nanoparticle Ligand-Shell Morphology Using NMR. *Nat. Commun.* **2012**, *3*.

(112) Necas, D.; Klapetek, P. Gwyddion: An Open-Source Software for SPM Data Analysis. *Central European Journal of Physics* **2012**, *10*, 181-188.

(113) Schneider, C. A.; Rasband, W. S.; Eliceiri, K. W. NIH Image to ImageJ: 25 Years of Image Analysis. *Nature Methods* **2012**, *9*, 671-675.

(114) Lee, A. G. Lipid Phase Transitions and Phase Diagrams II. Mixtures Involving Lipids *Biochim. Biophys. Acta* **1977**, *472*, 285-344.